Finanziato dall'Unione europea NextGenerationEU
Ministero dell'Università e della Ricerca
Italiadomani PIANO NAZIONALE DI RIPRESA E RESILIENZA
UNIVERSITÀ DEGLI STUDI DI NAPOLI FEDERICO II

multi-Risk sciEnce for resilienT commUnities undeR a changiNg climate
MUR: **PE00000005** – CUP LEAD PARTNER H93C22000610002

Deliverable title

Large plains: thematic maps of hazard severity indicators and zoning for coupled/combined trigger

Deliverable ID

DV 2.4.6

Due date: May 31, 2025
Submission date: May 15th, 2025

AUTHORS
Giovanni Forte (UNINA)
Giuseppe Bausilio (UNINA), Domenico Calcaterra (UNINA), Filippo Catani (UNIPD), Xue Chen (UNIPD), Rosa Colacicco (UNIBA), Melania De Falco (UNINA), Diego Di Martire (UNINA) Lucia Mele (UNINA), Ascanio Rosi (UNIPD), Francesco Silvestri (UNINA)

Table of contents

List of Figures

Technical references

Project Acronym	RETURN
Project Title	multi-Risk sciEnce for resilienT commUnities undeR a changiNg climate
Project Coordinator	Domenico Calcaterra UNIVERSITA DEGLI STUDI DI NAPOLI FEDERICO II domcalca@unina.it
Project Duration	December 2022 – November 2025 (36 months)
Deliverable No.	DV2.4.6
Dissemination level*	PU
Work Package	WP4 – Trigger-based multiple geohazard scenarios
Task	T2.4.3 – Multiple geohazards for ground instabilities in large plains, sinkhole zone
Lead beneficiary	UNINA

Contributing beneficiary/ies	UNIBA, UNIPD

* PU = Public
PP = Restricted to other programme participants (including the Commission Services)
RE = Restricted to a group specified by the consortium (including the Commission Services)
CO = Confidential, only for members of the consortium (including the Commission Services)

Document history

Version	Date	Lead contributor	Description
0.1		Giovanni Forte (UNINA) Giuseppe Bausilio (UNINA) Xue Chen (UNIPD) Rosa Colacicco (UNIBA) Melania De Falco (UNINA) Lucia Mele (UNINA) Francesco Silvestri (UNINA)	First draft
0.2		Salvatore Martino (UniRoma1) Francesca Bozzano (UniRoma1) Domenico Calcaterra (UNINA) Diego Di Martire (UNINA)	Spoke leader review
0.3		Giovanni Forte (UNINA)	Critical review and proofreading
0.4		Giovanni Forte (UNINA)	Final version

1 Abstract

This deliverable (DV 2.4.6), part of the RETURN project under WP4 and Task 2.4.3, addresses the development and application of methodologies for assessing and mapping ground instability hazards in large plains, with a specific focus on soil liquefaction, regional subsidence, and anthropogenic sinkholes. The overarching objective is to produce thematic hazard severity maps and zoning based on combined or coupled geohazard triggers, contributing to more resilient communities under a changing climate.

A central aspect of the deliverable is the implementation of a multi-level "tool chain" approach that integrates predisposing, preparatory, and triggering factors to assess hazard susceptibility. These tool chains allow for both qualitative and quantitative modeling across different spatial and temporal scales. Three main processes are analyzed: soil liquefaction, subsidence, and anthropogenic sinkholes, each studied within its geomorphological context and supported by case studies and scenario-based analysis.

For soil liquefaction, a tiered assessment methodology is applied. At Level 1, geological and geomorphological data, along with groundwater depth and Peak Ground Acceleration (PGA), are used to generate screening maps of susceptibility. At Level 2, a semi-empirical, stress-based evaluation using Cone Penetration Test (CPT) data is applied to calculate the Factor of Safety (FS) and Liquefaction Potential Index (LPI). The Emilia-Romagna region, affected by the 2012 earthquake, is used as a test area, revealing significant liquefaction susceptibility in Holocene fluvial deposits. Hazard scenarios are modeled by varying groundwater levels and PGA to generate spatially explicit LPI and settlement maps, which are further analyzed using statistical and spatial aggregation techniques.

Subsidence assessment leverages satellite-based Persistent Scatterer Interferometry (PSI) and temporal modeling to identify and classify deformation trends in the Po delta. This includes detection of abrupt changes, long-term trends, and seasonal variability, providing insight into both natural and anthropogenic drivers. The results are integrated into zoning maps to support urban planning and infrastructure management.

In the case of anthropogenic sinkholes, a dual-track methodology is introduced. One approach focuses on static susceptibility analysis using ensemble machine learning models (e.g., Random Forest, GBM, MaxEnt), while the second incorporates temporal forecasting through Poisson distribution modeling. The models are calibrated and validated using detailed inventories from cities such as Naples and Palermo, producing multi-scenario hazard forecasts that consider both sinkhole diameter and return period (from 1 month to several years). The final outputs are twelve combined magnitude-temporal risk scenarios that support targeted risk mitigation strategies.

Across all analyses, the RETURN project emphasizes integrated modeling, data fusion, and AI-

driven decision support tools aimed at informing local and national policies for disaster risk reduction. This deliverable provides a comprehensive framework for multi-hazard risk assessment in large plains, promoting robust and transferable methodologies adaptable to various geological and climatic contexts.

2 Introduction

This Deliverable (DV) presents the research activities carried out within SPOKE VS2 (Ground Instabilities) of the RETURN project. RETURN "Multi-risk science for resilient communities under a changing climate" was established with the aim of supporting communities in addressing the challenges posed by multiple, interacting hazards that are becoming increasingly frequent and intense due to climate change. The project is designed to develop practical tools and methodologies for managing complex climate-related risks such as wildfires, floods, droughts, and other extreme events, as earthquakes or volcanic eruptions. Through an interdisciplinary and multi-scale approach, RETURN leverages cutting-edge technologies, including satellite data, numerical modeling, and artificial intelligence (AI), to analyze how different hazards interact and influence each other. These technologies enable the creation of accurate forecasts and simulations, supporting informed decision-making and strategic planning. Moreover, RETURN aims to enhance the resilience of both infrastructures and citizens, not only by addressing individual hazards but also by understanding and mitigating the compound and cascading effects of multiple concurrent or sequential events. The ultimate goal is to inform and support national and EU policy development on risk management.

Within this broader framework, SPOKE VS2 focuses specifically on Ground Failures caused by geohazards such as landslides, sinkholes and subsidence, which may result from consolidation processes or liquefaction phenomena. One of the core objectives of SPOKE 2 is the mapping and risk assessment of these ground instabilities, aimed at producing integrated hazard maps. Each process was analyzed in terms of three categories of factors:

Predisposing factors (e.g., geological and geomorphological conditions),

Preparatory factors (e.g., long-term environmental changes or human activity),

Triggering factors (e.g., earthquakes, volcanic activity, or heavy rainfall).

By quantifying the influence of these categories, the project develops probabilistic and deterministic methods to reconstruct instability scenarios both on land and in marine environments. This allows for comprehensive assessments of the impact that such phenomena may have on the built environment, at both local and national scales. Particular attention is given to the combined and cascading effects of ground instabilities, exploring how one event may exacerbate or trigger others.

This document summarizes some of the activities of WP4, which is organized in 4 TASKs related

to the geomorphological setting/context in which ground instabilities develop. In particular, it focuses on:

Task 2.4.3: Multiple geohazards for ground instabilities in large plains, sinkhole zones (TK3).

It is focused on ground instabilities in large plains, including soil subsidence and sinkhole zones. Main topics of this task will concern multi-hazard effects and indicators in case of soil displacements in alluvial plains by combining process understanding (DV 2.4.5) and hazard mapping (DV 2.4.6) for multiple triggers. Following the approach proposed by RETURN, each process was divided into tasks on the basis of the geomorphological setting and successively classified through a kinematic approach.

In plain areas, the analyzed phenomena are:

Soil Liquefaction, process characterized by rapid occurrence;

Sinkholes, characterized by both slow and rapid kinematics;

Subsidence, which is a slow-moving process.

The occurrence of these phenomena in alluvial plains is analyzed with a multi-level approach labelled as "tool chain". This methodology accounts for the use of “tools” in terms of methods and data more suitable to model the effect of a hazard at a certain scale of representation. Tool chains are collected in the DV 2.4.5, while here are applied to test areas, for generating hazard maps, conduct uncertainty analysis on input and output data, and validate the overall approach. These results contribute to the broader goal of developing robust, transferable models for the informatic POC.

3 Soil Liquefaction assessment

Earthquake induced liquefaction can be defined as the temporary transition of a granular soil from the solid to a fluid state as a consequence of the increased pore-water pressures. The effects of liquefaction can be particularly damaging to the built environment, leading to consequences such as the sinking or tilting of buildings and infrastructure, as well as damage to roads and pipelines. In recent years, growing awareness of this risk has led to the development of hazard maps aimed at assessing and mitigating the impact of liquefaction in vulnerable areas.

Liquefaction typically occurs on loose saturated sandy deposits, being their contractive tendency upon cyclic shearing inhibited by water with the onset of positive excess pore pressures (Δu). If the excess pore pressures build up is positive, the normal effective stresses will reduce during the seismic action, eventually increasing back during the post-seismic consolidation phase. Since the soil shear strength $\tau(\sigma')$ and stiffness $G(\sigma')$ directly depend on the effective stresses, they will progressively reduce during the

seismic action on liquefiable soils, becoming nihil when the effective stresses tend to zero (full liquefaction, theoretically at ru=1, where ru is the pore pressure ratio defined as $\Delta u/\sigma'_c$). At the end of cyclic action, consolidation will take place due to the excess pore pressure drainage. Figure 1 summarized the phases before earthquake and after when liquefaction occurs (Flora et al., 2023).

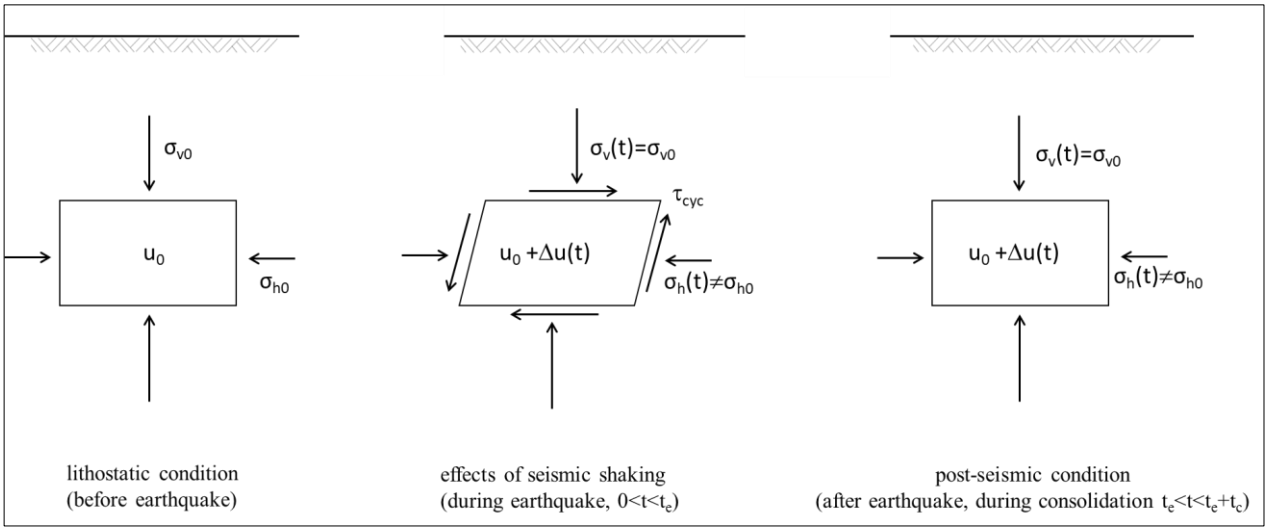

Figure 1 Stress state in a liquefiable layer before (t=0) and during an earthquake of duration te and after the earthquake, during the post-seismic consolidation of duration tc (Flora et al., 2023).

Liquefaction study methodologies include empirical approaches based on field investigations, such as Standard Penetration Tests (SPT) and Cone Penetration Tests (CPT), which measure soil resistance and help estimate its seismic response. Additionally, analytical methods based on advanced numerical models are employed. These models simulate the dynamic behavior of soils during an earthquake, incorporating variables such as stress history and permeability, to provide more accurate predictions of how liquefiable soils will behave under different seismic scenarios. By combining these techniques, it becomes possible to produce reliable assessments that inform urban planning and engineering interventions aimed at reducing the vulnerability of the built environment to liquefaction, thereby enhancing the safety of communities in seismically active areas. Over the past four decades, research on liquefaction phenomena has led to multiple perspectives in describing the mechanisms involved. Some authors define liquefaction as the condition in which the effective stress temporarily drops to zero, while others consider it to occur when the soil deforms under a constant shear stress. The former is referred to as cyclic mobility, and the latter as flow liquefaction.

To date, most studies have focused primarily on the liquefaction potential, i.e., whether liquefaction will occur or not. While the estimation of liquefaction effects has improved with the development of empirical procedures, the uncertainty in predicting these effects remains very high. Achieving a more reliable forecast of structural performance requires more accurate prediction of liquefaction effects (Kramer and Elgamal, 2001).

Liquefaction potential depends on a combination of intrinsic soil properties, environmental factors, and earthquake characteristics. Key soil properties include dynamic shear modulus, damping characteristics, grain size distribution, relative density, and soil fabric. Among environmental factors, soil formation processes, seismic and geological history, lateral earth pressure coefficient, depth to the water table, and effective confining pressure significantly influence liquefaction behavior. Additionally, the intensity and duration of ground shaking are critical in determining liquefaction occurrence.

To evaluate liquefaction potential, both macroscopic and microscopic assessment methods are used, involving field and laboratory tests. Critical conditions are typically found at depths less than 15 meters and for seismic intensities above VI on the Modified Mercalli scale (Kramer and Stewart, 2024) while soil parameters that indicate a higher probability of liquefaction include:

- Mean grain size between 0.02 and 1.0 mm,
- Coefficient of uniformity below 10,
- Relative density below 75%,
- Plasticity index below 10.

The susceptibility of a soil to liquefaction can be evaluated using three main criteria:

1) Historical criterion: Soils that have liquefied in past seismic events are likely to do so again, and this can be assessed through historical seismic data.
2) Geological/geomorphological criterion: Soils formed through fluvial, lacustrine, eolian, or artificial fill processes (especially hydraulic fills) are particularly susceptible. Youd and Perkins (1978) analyzed the liquefaction susceptibility of various deposit types by assigning qualitative susceptibility scores based on depositional environment and geologic age. The relative susceptibility chart by Anderson et al. (2006) (shown in Figure 2) indicates that recent unconsolidated deposits, such as Holocene river channels, alluvial plains, and deltaic deposits, show high to very high liquefaction susceptibility. In contrast, alluvial fan and plain deposits, beaches, glacial deposits, residual soils, tuffs, and compacted fills are generally less susceptible. For all deposit types, susceptibility decreases with increasing age, from recent (< 500 years) to pre-Pleistocene, with the exception of loess, which remains susceptible to liquefaction during strong earthquakes regardless of age. Holocene sediments are more susceptible than Pleistocene, while Pre-Pleistocene sediments are rarely affected.

Type of deposit (1)	General distribution of cohesionless sediments in deposits (2)	Likelihood that Cohesionless Sediments, When Saturated, Would Be Susceptible to Liquefaction (by Age of Deposit)			
		<500 yr (3)	Holocene (4)	Pleistocene (5)	Pre-pleistocene (6)
(a) Continental Deposits					
River channel	Locally variable	Very high	High	Low	Very low
Flood plain	Locally variable	High	Moderate	Low	Very low
Alluvial fan and plain	Widespread	Moderate	Low	Low	Very low
Marine terraces and plains	Widespread	—	Low	Very low	Very low
Delta and fan-delta	Widespread	High	Moderate	Low	Very low
Lacustrine and playa	Variable	High	Moderate	Low	Very low
Colluvium	Variable	High	Moderate	Low	Very low
Talus	Widespread	Low	Low	Very low	Very low
Dunes	Widespread	High	Moderate	Low	Very low
Loess	Variable	High	High	High	Unknown
Glacial till	Variable	Low	Low	Very low	Very low
Tuff	Rare	Low	Low	Very low	Very low
Tephra	Widespread	High	High	?	?
Residual soils	Rare	Low	Low	Very low	Very low
Sebka	Locally variable	High	Moderate	Low	Very low
(b) Coastal Zone					
Delta	Widespread	Very high	High	Low	Very low
Esturine	Locally variable	High	Moderate	Low	Very low
Beach					
High wave energy	Widespread	Moderate	Low	Very low	Very low
Low wave energy	Widespread	High	Moderate	Low	Very low
Lagoonal	Locally variable	High	Moderate	Low	Very low
Fore shore	Locally variable	High	Moderate	Low	Very low
(c) Artificial					
Uncompacted fill	Variable	Very high	—	—	—
Compacted fill	Variable	Low	—	—	—

Figure 2. Liquefaction susceptibility of sedimentary deposits by Youd and Perkins (1978), (from Anderson et al., 2006).

3) Compositional criterion: This pertains to soil grain structure. Uniformly graded soils are more prone to liquefaction than well-graded soils, and rounded particles are more susceptible than angular ones. Even cohesive soils with fines content (particles < 0.002 mm) below 30%, liquid limits under 35%, and water content exceeding 90% of the liquid limit may experience significant strength loss and be considered liquefiable if deformation exceeds certain thresholds (Seed et al., 1983).

In addition to sandy and silty soils, gravelly soils can also exhibit liquefaction vulnerability, particularly when voids between coarse particles are filled with fines, or when surrounded by low-permeability soils that restrict drainage and promote cyclic pore pressure buildup. However, because gravelly deposits are typically dense and stable, a preliminary conservative analysis is often sufficient to assess their liquefaction risk. Generally, pre-Holocene gravel deposits are generally considered less susceptible.

A synthesis of the various approaches and methodologies was provided by Silvestri and D'Onofrio (2014), who stated that the assessment of liquefaction triggering, and more generally the response of a soil deposit in terms of pore pressure build-up, can be carried out using methods of increasing complexity,

as briefly summarized in Table 1. The methods more suitable to the mapping are represented by level 1 and level 2. The others 3 and 4 rely on numerical modelling and can be applied at the scale of the site (1D) or of the cross-section (2D) and for this reason are out of the scope of the tool chain.

Table 1. Analyses for liquefaction triggering assessment modified after (Silvestri and D'Onofrio, 2014).

Level of analysis	Type of analysis	Constitutive model	Calculation approach	Output
Level 1	Screening criteria (qualitative)	-	Evaluation of some parameters (grain size distribution, ground water table and expected maximum acceleration)	Liquefaction yes, no
Level 2	Semi-empirical methods	Elementary	Simplified stress-based	Actions (demand) vs. Resistance (capacity)
Level 2	Simplified dynamic analyses	Simplified (mostly visco-elastic, uncoupled)	Dynamic (with simplified geometry)	Total stresses, shear strains, pore pressure increments*
Level 4	Advanced dynamic analyses	Advanced (elasto-plastic with hardening, coupled)	Dynamic (with complex 3D geometry)	Total and effective stresses, shear strains, pore pressure increments, residual displacements

*Calculated through analytical correlations.

According to NTC, 2018, the likelihood of liquefaction occurring in saturated sandy soils is low or zero if at least one of the following conditions occurs:

1. maximum expected accelerations at ground level in free field conditions less than 0.1g;
2. average seasonal depth of the groundwater table higher than 15 m from ground level;
3. deposits consisting of clean sands with normalised penetrometer resistance $(N_1)_{60} > 30$ or $q_{c1N} > 180$;
4. particle size distribution outside the zones shown in Figure 3a in the case of soils with uniformity coefficient $U_c < 3.5$ and in Figure 3b in the case of soils with uniformity coefficient $U_c > 3.5$.

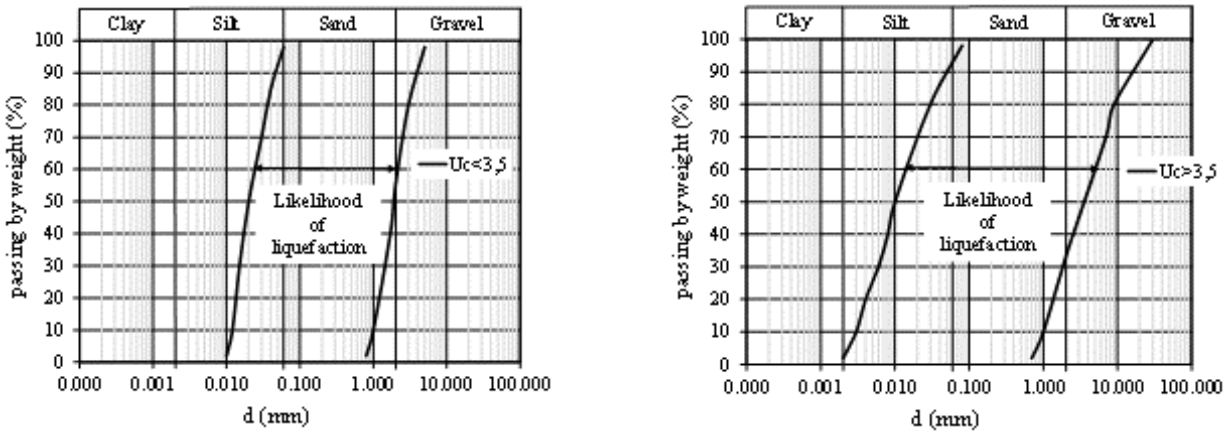

(a) U_c<3.5 (b) U_c>3.5

Figure 3. Particle size ranges of soils susceptible to liquefaction (adapted from NTC (2018) with uniform coefficient Uc< 3.5 (a) and Uc> 3.5 (b).

If the first condition is not verified and, therefore, the maximum acceleration expected at ground level is higher than 0.1 g, the geotechnical investigations must be aimed at determining the parameters necessary to verify the other three conditions.

When none of the four abovementioned conditions is satisfied, NTC (2018) states that the site is potentially susceptible to liquefaction (i.e. prone, due to the presence of predisposing elements) and the area is potentially at risk (due to the non-negligible seismic hazard). It is therefore necessary to assess the liquefaction safety factor at the depths where potentially liquefiable soils are present.

3.1 Tool chain for soil liquefaction

As described in the DV 2.4.5., to create a unified framework across the work packages (WPs), "tool chains" have been developed to capture the full sequence of factors involved in a specific process, from predisposing to preparatory and finally to triggering factors. According to the definitions provided in VS2, this classification is based on a temporal scale: predisposing factors are considered stable over the observation period, while preparatory factors can vary or follow cyclic trends within the same timeframe. Triggering events, on the other hand, occur within a very short and clearly defined timespan.

In the context of soil liquefaction, predisposing factors include geological characteristics, earthquakes with magnitudes greater than 5, fluctuations in the groundwater table, peak ground acceleration (PGA), and geotechnical properties (see Figure 4).

The liquefaction tool chain assigns different levels of significance to each factor, indicated by a star rating: very high importance (4 stars for water table depth less than 15 m) and high importance (3 stars for geology, geotechnical properties, and expected PGA > 0.1g).

This process enables both qualitative and quantitative assessments of liquefaction susceptibility and the expected degree of ground settlement.

Based on this framework, a preliminary case study was conducted in an area with sufficient input data (e.g., geological and geotechnical information, groundwater level) and historical liquefaction events, enabling verification of the tool chain's application.

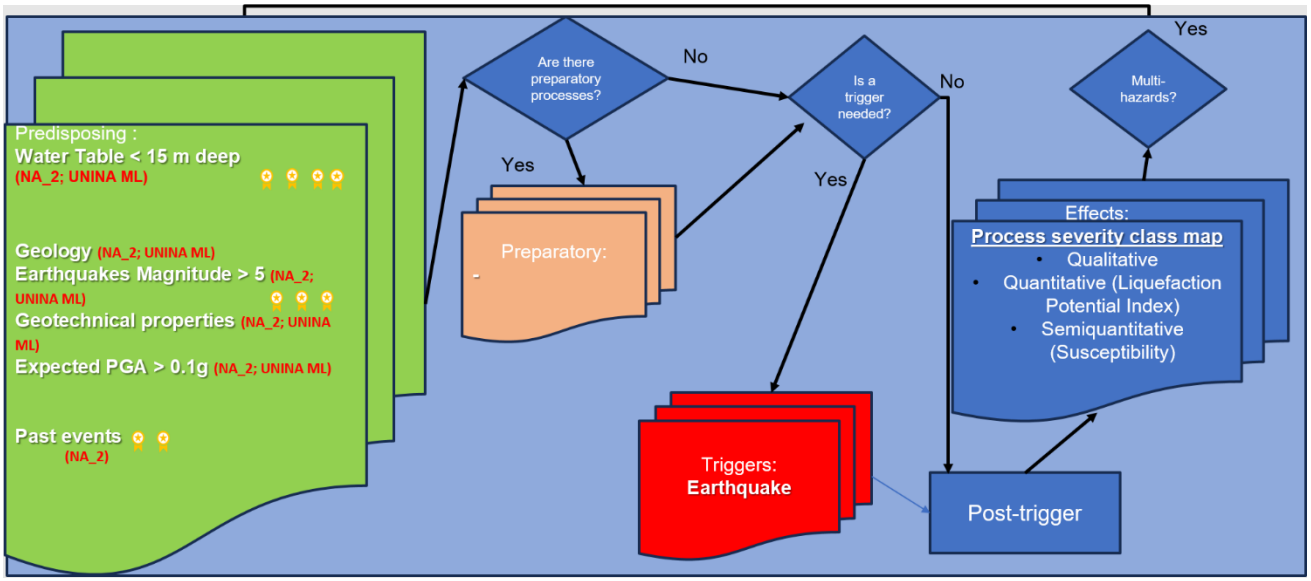

Figure 4. Tool chain developed under the RETURN project for liquefaction analysis.

3.2 Level I for soil liquefaction susceptibility

Liquefaction susceptibility can be evaluated in four levels as reported in Table 1, but to define susceptibility in large areas, levels 1 and 2 are the most suitable. In particular, knowing the geological and geomorphological characteristics of the area and the groundwater table depth, it is possible to develop a basic susceptibility map (level 0) also called "screening map" to assess which macro sectors are more susceptible than others. Youd and Perkins (1978) analysed the liquefaction susceptibility of various types of soil deposits by assigning a qualitative susceptibility score based on general depositional environment and geologic age of the deposit. The relative susceptibility degree of Anderson et al. (2006) shown in Figure 3 indicates that unconsolidated soils recently deposited such as Holocene age river channel, floodplain, and delta deposits have high to very high liquefaction susceptibility. Such deposits as an alluvial fan and plain, beach, glacial till, talus, residual soils, tuff and compacted fill are, in general, not susceptible to liquefaction. For each deposit type, the liquefaction susceptibility is decreasing by the ages, from young (< 500 years) to old (Pre-Pleistocene), except for the loess, which is always susceptible to liquefaction during strong earthquakes no matter the age is of Holocene or Pleistocene. The Holocene sediments are more susceptible to liquefaction than the Pleistocene ones, and the Pre-Pleistocene sediments are rarely susceptible.

According to Youd and Perkins (1978), and considering the water table depth, the susceptibility of level 0 was performed using the "if/then" logic scheme (Figure 5).

Following the scheme the low susceptibility is obtained if the deposits belong to river channel, flood/alluvial plain, beach plain and lacustrine of pre-Pleistocene age and the water table is < 15 meters deep. Susceptibility is medium if deposits belong to Holocene floodplain, beach or delta/fan-delta or Pleistocene lacustrine with water table < 15 meters, while a high degree of susceptibility occurs if the deposits belong to Holocene river channel and pyroclastic soils or Pleistocene/Holocene loess.

Liquefaction events in mountain, foothill and hill environments do not occur, as well as in plain areas where the PGA is very low (< 0.01g) or the water table depth is > 15 meters, then the susceptibility results null.

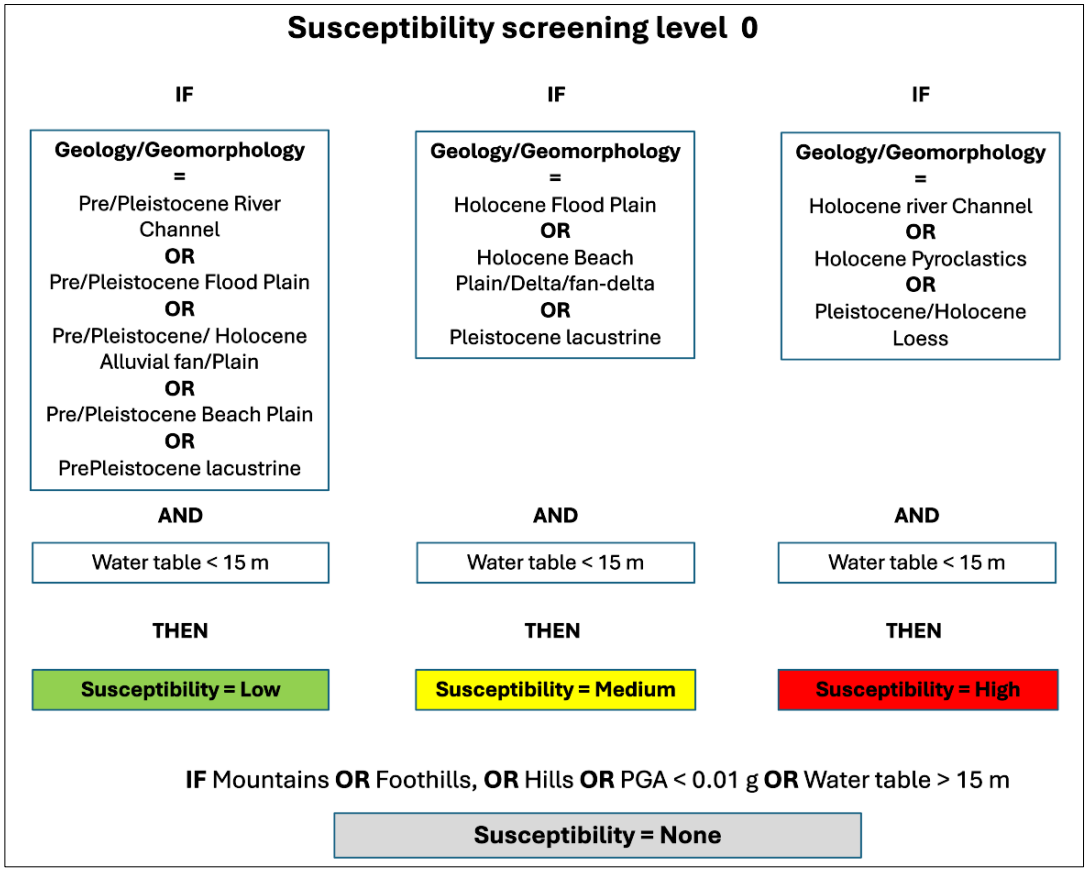

Figure 5. Scheme to evaluate the susceptibility liquefaction of level 0.

Taking into account also the PGA, which can be considered both a predisposing and a triggering factor, the scheme for assessing liquefaction susceptibility of level 1 was developed. According to NTC (2018), the value of PGA must be greater than 0.1g to have liquefaction. Thus, by intersecting the geological and geomorphological features of the deposits, the depth of the water table and the PGA, susceptibility classes from low to very high are obtained. In particular, as shown in Figure 6, susceptibility is low if pre-Pleistocene/Pleistocene deposits with water table depth less than 15 meters and low PGA values are observed. The level of susceptibility is very high when Holocene river channel or pyroclastic

soils or loess deposits are present together with a water table depth < 15 meters and PGA values > 0.1g.

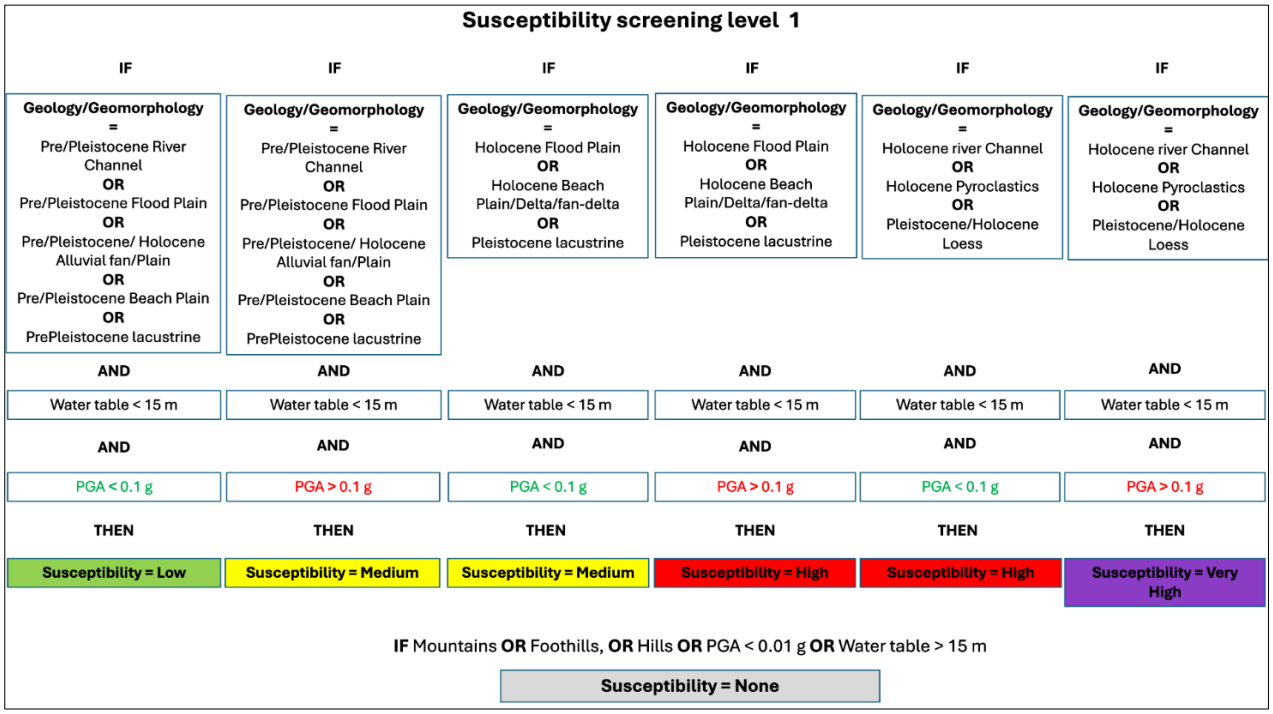

Figure 6. Scheme to evaluate the susceptibility liquefaction of level 1.

3.3 Level 2 for soil liquefaction susceptibility

Usually in engineering practice, liquefaction triggering assessment is carried out using the semi-empirical stress-based analysis (level 2). With this approach, a factor of safety FS(z) is defined for free-field conditions (i.e. without buildings and structures) as the ratio between the normalized shear stress required to induce liquefaction (CRR=soil capacity) and the normalized equivalent stress induced by the design earthquake (CSR=demand) (Boulanger and Idriss, 2014; Seed and Idriss, 1971):

$$FS(z) = \frac{CRR(z)}{CSR(z)} = \frac{CRR_{M=7,5,\sigma'v=1}}{CSR} \cdot MSF \cdot K_\sigma \cdot K_\alpha \qquad Eq.\ 1$$

where soil capacity $CRR_{M=7.5}$, $\sigma'v_{=1}$ is calculated with reference to a seismic event of magnitude M=7.5 and a vertical effective stress state of one atmosphere (101 kPa). The parameter MSF (Magnitude Scaling Factor) is a factor accounting for the effect of earthquake magnitude, and the two corrective coefficients K_σ and K_α respectively take into account the effects of vertical stress and of a possible pre-existing static shear stress on horizontal planes (e.g. sloping ground or state of stress under existing structures) (see Figure 3 for their expressions). Literature data (e.g. Tomasello and Porcino (2022); Vaid et al. (2001) indicate that, in loose or medium dense sands (D_r < 50%), pre-existing shear stresses reduce soil capacity. In this density range, from a practical point of view, this detrimental effect can be considered

assuming $K_\alpha = 0.8$.

Liquefaction resistance can be evaluated interpreting the results of in-situ or laboratory tests. Usually, in situ tests are more commonly adopted for the following shortcomings of laboratory tests:

i) it is extremely difficult to retrieve granular undisturbed samples on site: therefore, tested specimens may not represent the true in situ conditions;

ii) laboratory tests are carried out using constant amplitude cycles; as a consequence, for their interpretation a correlation has to be introduced between the irregular seismic action and the equivalent number of constant amplitude cycles, N;

iii) even if using very sophisticated laboratory apparatuses, the stresses applied in laboratory cannot represent the true stress path experienced by the soil in situ during the earthquake.

Therefore, the values of CRR are generally derived from historic-empirical correlations based on CPT and SPT results (Boulanger and Idriss, 2014) as:

- $$CRR_{M=7.5,\sigma'v=1} = exp\left(\frac{q_{c1Ncs}}{113} + \left(\frac{q_{c1Ncs}}{1000}\right)^2 - \left(\frac{q_{c1Ncs}}{140}\right)^3 + \left(\frac{q_{c1Ncs}}{137}\right)^4 - 2.8\right) \quad \textit{Eq. 2}$$

- $$CRR_{M=7.5,\sigma'v=1} = exp\left(\frac{N_{1,60cs}}{14.1} + \left(\frac{N_{1,60cs}}{126}\right)^2 - \left(\frac{N_{1,60cs}}{23.6}\right)^3 + \left(\frac{N_{1,60cs}}{25.4}\right)^4 - 2.8\right) \quad \textit{Eq. 3}$$

where q_{c1Ncs} and $(N_1)_{60cs}$ are respectively the normalized values of the tip resistance (CPT) and the number of blows (N_{SPT}) corrected for the finest content (FC, defined as the percentage by weight passing at the 0.075 mm sieve).

It has to be emphasized that Eq. 2 and Eq. 3 have no mechanical origin and are just analytical correlations empirically set up to separate historical data of liquefied from non-liquefied cases in a capacity vs. demand plane. Generally, they correspond to a conservative lower bound of the observed values of CRR, and thus lead to a conservative estimate of FS(z).

With the semi-empirical approach, the stress state induced by the seismic action is estimated through the knowledge of the maximum horizontal acceleration expected at ground level (PGA, a_{max}) according to a well-established empirical procedure, or as a(z) at the generic depth of interest, if the results of local seismic response analyses are used. Typically, with this approach the cyclic stress ratio CSR is calculated as (Seed and Idriss, 1971):

- $$CSR(z) = 0.65\frac{a_{max}}{g}\frac{\sigma_v}{\sigma'_v}r_d \quad \textit{Eq. 4}$$

where σ_v and σ'_v are the total and effective lithostatic stress at the generic depth (z), a_{max} is the peak value of the expected horizontal acceleration at the surface, g is the earth's gravitational acceleration and

r_d is a reductive factor of the acceleration to take into account the deformability of the soil column and can be estimated empirically or calculated numerically through a local seismic response analysis. In this calculation, if remediation actions have to be implemented, the effects of ground improvement should be taken into account considering their effect in terms of stiffness increase.

3.3.1 *Methods based on CPT*

The use of in-situ testing is the dominant approach in engineering practice for the quantitative evaluation of liquefaction potential. To assess the liquefaction resistance of soils, it is necessary to calculate two variables: the seismic demand on a soil layer, expressed in terms of CSR (Cyclic Stress Ratio), and the soil's capacity to resist liquefaction, expressed as CRR (Cyclic Resistance Ratio). The models proposed by Seed and Idriss (1971), Seed and Peacock (1971), Iwasaki et al. (1984) and Robertson and Wride (1998) are widely used to predict potential liquefaction using field data. In addition, Youd and Idriss (2001) provided a detailed review of various field methods for assessing soil liquefaction potential.

The CPT (Cone Penetration Test) has become one of the most common and economical exploration method. The cone penetrometer is pushed into the ground at a standard rate of 2 cm/sec, and data is recorded at regular intervals (typically every 2 or 5 cm) during penetration. The results provide excellent stratigraphic detail and repeatability, provided proper attention is paid to equipment calibration (transducers and electronics). It is a versatile investigation method that can be used to determine soil materials and their properties within a soil profile.

To evaluate soil liquefaction potential, it is essential to determine soil stratification and the in-situ soil condition.

The simplified method by Robertson and Wride (1998) to estimate the cyclic shear stress (CSR) was developed by Seed and Idriss (1971), based on the site's peak ground acceleration, as follows:

$$CSR = \frac{\tau_{av}}{\sigma_0'} = 0.65(MWF)\left(\frac{\sigma_0}{\sigma_0'}\right)\left(\frac{a_{max}}{g}\right)r_d \qquad Eq.\ 5$$

$$MWF = M^{2.56}/173 \qquad Eq.\ 6$$

where MWF is the magnitude weighting factor, and M is the earthquake magnitude, commonly taken as M = 7.5. Seed et al. (1985) also developed a method for estimating the Cyclic Resistance Ratio (CRR) for clean sands and silty sands based on CPT, using normalized penetration resistance. The CPT-based liquefaction correlation was re-evaluated by Idriss and Boulanger (2006) using compiled data from Shibata and Teparaksa (1988), Kayen et al. (1992), Boulanger (2003) and Moss et al. (2003).The Magnitude Scaling Factor (MSF) is a parameter used in evaluating liquefaction potential to account for the effect of earthquake duration, represented by its magnitude. Specifically, this factor is used to adjust

the calculated CSR to make the liquefaction potential estimate applicable to earthquakes of different magnitudes than those considered in the original tests.

Seed and Idris (1982) introduced a correction factor called the Magnitude Scaling Factor (MSF), which can be used to shift CRR-based curves up or down, depending on the earthquake magnitude. Figure 7 shows curves proposed by various authors for different magnitudes.

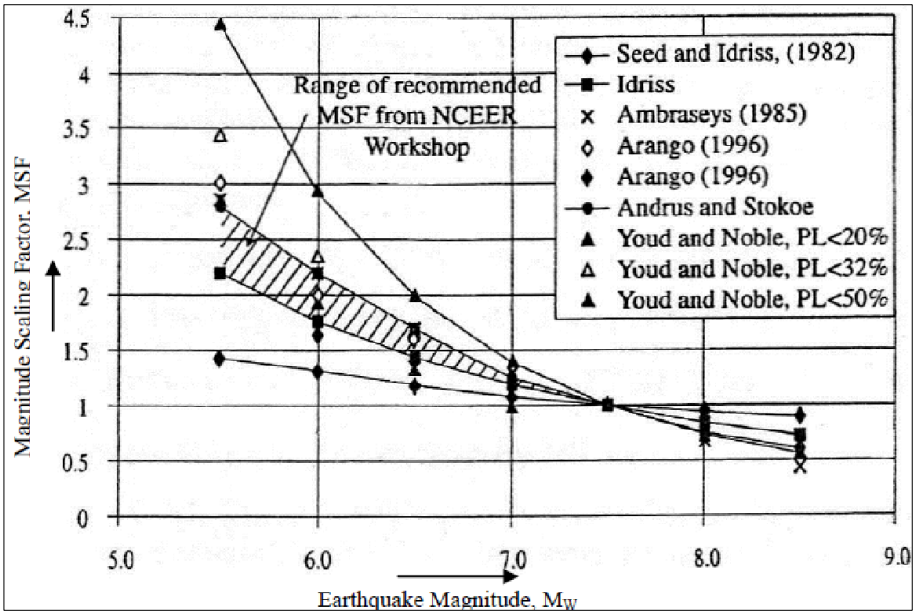

Figure 7. MSF obtained from different sources Youd and Idriss (2001).

They also developed a set of MSFs based on the average number of loading cycles for various earthquake magnitudes and lab test results. The MSF was defined as:

$$MSF = \left(\frac{10^{2.24}}{{M_w}^{2.56}}\right) \qquad Eq.\ 7$$

The revised scaling factors were higher than the original for magnitudes < 7.5 and slightly lower for magnitudes > 7.5. Compared to the original factors, the revised MSFs result in lower calculated liquefaction hazard for M < 7.5, but higher hazard for M > 7.5. These revised factors were suggested as lower bounds by participants at the NCEER (National Center for Earthquake Engineering Research) workshop.

Ambraseys (1988) analyzed liquefaction data and calculated cyclic stresses at sites that did or did not experience liquefaction, based on N60 values. From this, he developed an empirical equation defining CRR as a function of N60 and moment magnitude. For M < 7.5, the MSFs proposed by Ambraseys are significantly higher than those by Seed and Idris (1982), and for M > 7.5, significantly lower, making them more conservative.

Andrus and Stokoe (2000) developed MSFs by drawing boundary curves for sites where surface

effects of liquefaction were observed or not for earthquakes of magnitudes 6, 6.5, and 7.0. MSFs for M < 6 and > 7.5 were extrapolated using the following equation:

$$MSF = \left(\frac{M_w}{7.5}\right)^{-2.56} \qquad Eq.\ 8$$

For M < 7.5, the MSFs proposed by Andrus and Stokoe (2000) are close to those proposed by Ambraseys (1988). For M > 7.5, the MSFs by Andrus and Stokoe are slightly lower than the revised MSFs by Seed and Idris (1982).

Youd and Noble (1997) used a probabilistic and logistic regression analysis of historical data from sites that did or did not report liquefaction in past earthquakes. They defined three MSF sets for different magnitude intervals and various probabilities of liquefaction (PL):

$$P_L < 20\% \qquad MSF = \left[\frac{10^{3.81}}{M^{4.53}}\right] \qquad for\ M_w < 7 \qquad Eq.\ 9$$

$$P_L < 32\% \qquad MSF = \left[\frac{10^{3.74}}{M^{4.43}}\right] \qquad for\ M_w < 7 \qquad Eq.\ 10$$

$$P_L < 50\% \qquad MSF = \left[\frac{10^{4.21}}{M^{4.81}}\right] \qquad for\ M_w < 7.75 \qquad Eq.\ 11$$

Figure 8 provides MSF values by several Authors.

Magnitude, *M* (1)	Seed and Idriss (1982) (2)	Idriss[a] (3)	Ambraseys (1988) (4)	Arango (1996) Distance based (5)	Arango (1996) Energy based (6)	Andrus and Stokoe (1997) (7)	Youd and Noble (1997b) P_L < 20% (8)	Youd and Noble (1997b) P_L < 32% (9)	Youd and Noble (1997b) P_L < 50% (10)
5.5	1.43	2.20	2.86	3.00	2.20	2.8	2.86	3.42	4.44
6.0	1.32	1.76	2.20	2.00	1.65	2.1	1.93	2.35	2.92
6.5	1.19	1.44	1.69	1.60	1.40	1.6	1.34	1.66	1.99
7.0	1.08	1.19	1.30	1.25	1.10	1.25	1.00	1.20	1.39
7.5	1.00	1.00	1.00	1.00	1.00	1.00	—	—	1.00
8.0	0.94	0.84	0.67	0.75	0.85	0.8?	—	—	0.73?
8.5	0.89	0.72	0.44	—	—	0.65?	—	—	0.56?

Note: ? = Very uncertain values.
[a]1995 Seed Memorial Lecture, University of California at Berkeley (I. M. Idriss, personal communication to T. L. Youd, 1997).

Figure 8. MSF values by several Authors (Youd and Idriss, 2001).

Figure 9 summarizes the steps necessary to calculate FS(z) with the semi-empirical stress based approach (Boulanger and Idriss, 2014; Idriss and Boulanger, 2008).

It has to be highlighted that, even though the normalized values q_{c1Ncs} and $(N_1)_{60cs}$ take into account the fines content, sometimes they may lead to a misprediction of soil capacity: this is for instance the case of pyroclastic soils, which may have a relevant fines content FC with no plasticity (which means that the normalized resistance overestimates the beneficial effect of FC on CRR), and their fragile grains may be easily crushed by the testing tool (especially during SPT) (which means that soil shear strength may be underestimated). The combined effect of these two peculiarities cannot be theoretically assessed, but some experimental evidence (i.e. Anderson et al. (2019)) indicate that the use of the semi-empirical stress based

approach for pyroclastic soils is largely conservative, because of an overall underestimate of soil capacity.

Moreover, it should be stressed that the simplified approach just described does not consider peculiar site mechanisms that may affect the overall behaviour, like for instance the so called "system response" in layered deposits, smartly identified by Cubrinovski et al. (2019) in well documented case histories in Christchurch.

$$q_{c1} = C_N \cdot q_c$$

$$q_{c1N} = \frac{q_{c1}}{P_a} \quad (P_a = 101kPa)$$

$$C_N = \left(\frac{P_a}{\sigma'_v}\right)^m \leq 1.7 \quad m = 1.338 - 0.249 \cdot (q_{c1N})^{0.264}$$

$$(N_1)_{60} = C_N \cdot N_{60}$$

$$C_N = \left(\frac{P_a}{\sigma'_v}\right)^m \leq 1.7 \quad m = 0.784 - 0.0768 \cdot \sqrt{(N_1)_{60cs}}$$

$$FC = 80 \cdot (I_c + C_{FC}) - 137 \quad -0.29 \leq C_{FC} \leq 0.29$$

$$I_c = [(3.47 - logQ)^2 + (1.22 + logF)^2]^{0.5}$$

$$Q = \left(\frac{q_c - \sigma_{vc}}{P_a}\right) \cdot \left(\frac{P_a}{\sigma'_{vc}}\right)^n \qquad F = \left(\frac{f_s}{q_c - \sigma_{vc}}\right) \cdot 100$$

$$FC = 80 \cdot (I_c + C_{FC}) - 137 \quad -0.29 \leq C_{FC} \leq 0.29$$

$$I_c = -0.717 \cdot ln\left(\frac{V_s^2}{9.81 \cdot z}\right) + 6.3211$$

$$V_s = 100.59 \cdot N_{SPT}^{0.302}$$

$$\Delta q_{c1N} = \left(11.9 + \frac{q_{c1N}}{14.6}\right) \cdot exp\left[1.63 - \frac{9.7}{FC + 2} - \left(\frac{15.7}{FC + 2}\right)^2\right]$$

$$q_{c1Ncs} = q_{c1N} + \Delta q_{c1N}$$

$$\Delta(N_1)_{60} = exp\left[1.63 + \frac{9.7}{FC + 0.01} - \left(\frac{15.7}{FC + 0.01}\right)^2\right]$$

$$(N_1)_{60cs} = (N_1)_{60} \quad \Delta(N_1)_{60}$$

$$CRR_{M=7.5,\sigma'v=1} = \exp\left[\frac{q_{c1Ncs}}{113} + \left(\frac{q_{c1Ncs}}{1000}\right)^2 - \left(\frac{q_{c1Ncs}}{140}\right)^3 + \left(\frac{q_{c1Ncs}}{137}\right)^4 - 2.8\right]$$

$$CRR_{M=7.5,\sigma'v=1} = \exp\left[\frac{(N_1)_{60cs}}{14.1} + \left(\frac{(N_1)_{60cs}}{126}\right)^2 - \left(\frac{(N_1)_{60cs}}{23.6}\right)^3 + \left(\frac{(N_1)_{60cs}}{25.4}\right)^4 - 2.8\right]$$

$$FS = \frac{CRR}{CSR}$$

$$CSR = 0.65 \cdot \frac{a_{max}}{g} \cdot \frac{\sigma_v}{\sigma'_v} \cdot r_d \cdot \frac{1}{MSF} \cdot \frac{1}{K_\sigma} \cdot \frac{1}{K_\alpha}$$

$$\ln(r_d) = \alpha + \beta \cdot M$$

$$\alpha = -1.012 - 1.26 \cdot sen\left(\frac{z}{11.73} + 5.133\right)$$

$$\beta = 0.106 - 0.118 \cdot sen\left(\frac{z}{11.28} + 5.142\right)$$

$$C_\sigma = \frac{1}{37.3 - 8.27 \cdot q_{c1Ncs}^{0.264}} \leq 0.3 \qquad K_\sigma = 1 - C_\sigma \cdot ln\frac{\sigma'_v}{P_a} \leq 1.1 \qquad C_\sigma = \frac{1}{18.9 - 2.55 \cdot (N_1)_{60cs}^{0.5}} \leq 0.3$$

$$MSF = 6.9 \cdot exp\left(-\frac{M}{4}\right) - 0.058$$

$$K_\alpha = a + b \cdot exp\left(-\frac{\xi_R}{c}\right)$$

$$a = 1267 + 636 \cdot \alpha^2 - 634 \cdot \exp(\alpha) - 632 \cdot \exp(-\alpha)$$

$$b = \exp(-1.11 + 12.3 \cdot \alpha^2 + 1.31 \cdot ln(\alpha + 0.0001)) \qquad \alpha = \frac{\tau_s}{\sigma'_{vc}}$$

$$c = 0.138 + 0.126 \cdot \alpha + 2.52 \cdot \alpha^3$$

$$\xi_R = \frac{1}{Q - ln\left[\frac{100 \cdot (1 + 2 \cdot K_0) \cdot \sigma'_{vc}}{3 \cdot P_a}\right]} - (0.478 \cdot q_{c1Ncs}^{0.264} - 1.063)$$

$$\xi_R = \frac{1}{Q - ln\left[\frac{100 \cdot (1 + 2 \cdot K_0) \cdot \sigma'_{vc}}{3 \cdot P_a}\right]} - \sqrt{\frac{(N_1)_{60}}{46}}$$

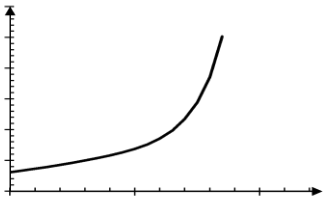

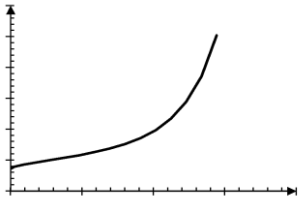

Figure 9. Procedure to calculate FS(z) based on the knowledge of (a) qc1Ncs or (b) (N1)60cs (Flora et al., 2023).

This mechanism, that can be quantitatively taken into account only using fully coupled advanced dynamic analyses, is related to the hydraulic interaction between contiguous granular layers, i.e. to the change in their pore pressure regime during the earthquake (or immediately after it) caused by transient inter-layer flows that may lead to the liquefaction of layers initially far from it.

FS values lower than 1 imply the liquefaction susceptibility of site. In this case, the potential consequences of liquefaction can be evaluated with the integral response of the deposit, through the simplified liquefaction index LSN (Tonkin and Taylor, 2012), defined as:

$$LSN = 1000 \int_0^{20} \frac{\varepsilon_v}{z} dz \qquad \textit{Eq. 12}$$

where z is the depth in meters and ε_v is the post-liquefaction volumetric reconsolidation strain (entered as a decimal) that can be calculated according to existing charts (see (Ishihara and Yoshimine, 1992). Degree of damage can be estimated as:

- 0<LSN<20: minor;
- 20<LSN<40: major;
- LSN>40: severe.

It is worth mentioning that LSN is not the only indicator proposed in literature, and many alternatives have been suggested in time. From a historical point of view, the first (and most popular) integral indicator is the *Liquefaction Potential Index*, LPI (Iwasaki et al., 1984), which represents a measure of the vulnerability of a site as a single value, ranging between 0 (very low risk) and values over 15 (very high risk), defined as:

$$LPI = \int_0^{20} F(z) \cdot W(z) dz \qquad \textit{Eq. 13}$$

where z is the depth in meters, while $F(z)$ and $W(z)$ are respectively:

$$F(z) = \{1 - FS \quad for \quad FS \quad < 1 \; 0 \qquad for \quad FS \quad \geq 1 \qquad \textit{Eq. 14}$$

$$W(z) = 10 - 0.5z \qquad \textit{Eq. 15}$$

in which FS is computed by Eq. 1.

3.3.2 Assessment of the liquefaction-induced settlements

In sandy soil deposits, effective stresses can approach zero, and as a result, the soil behavior shifts from that of a solid to that of a fluid, triggering liquefaction. When liquefaction occurs, significant settlements of shallow foundations and other engineering structures can take place. In many recent strong earthquakes (e.g., New Zealand, 2011; Japan, 2011; Emilia-Romagna, 2012; Turkey, 2023), liquefaction-induced phenomena caused considerable damage to the built environment.

In practice, earthquake-induced building settlements are quantified using empirical procedures developed by considering one-dimensional (1-D) volumetric consolidation settlements under "free-field" conditions, ignoring the presence of structures at the ground surface (e.g., (Ishihara and Yoshimine, 1992; Tokimatsu and Seed, 1987)). In other words, only volumetric deformations are considered, mainly due to the dissipation of excess pore water pressure accumulated during the seismic sequence.

Settlements (w) can be estimated using the following equation:

$$w = \sum_{i=1}^{j} \varepsilon_{z,i} \cdot \Delta z_i \qquad \textit{Eq. 16}$$

where ε_{zi} is the post-liquefaction volumetric strain for the *i-th* soil layer; Δzi is the thickness of the *i-th* layer; and *j* is the number of soil layers.

Methods for estimating liquefaction-induced settlements aim to predict how much the ground will subside due to soil liquefaction during seismic events. These methods mainly focus on the behavior of loose and saturated soils (often sands and silts) that lose strength when shaken. Approaches range from simple empirical ones—based on field test data and past experience—to more complex numerical models that simulate soil behavior under seismic conditions.

Empirical methods are easy to apply but may lack accuracy under varying geotechnical conditions, while analytical, stress-strain, and probabilistic methods offer greater precision but require more detailed input data and computational resources. The choice of method depends on the site's complexity, data availability, and the level of accuracy required for engineering analysis. Below are the most commonly used methods.

Probabilistic methods incorporate uncertainty and variability in soil properties, seismic loading, and site conditions. They provide estimates based on probability distributions rather than deterministic values. These methods are useful in risk assessments and help account for the variability in seismic and soil parameters. The Monte Carlo approach uses statistical methods to generate numerous possible liquefaction and settlement outcomes based on variable inputs (e.g., soil density, seismic intensity). The results are presented as probability distributions of settlements. Probabilistic Seismic Hazard Analysis (PSHA), often combined with Monte Carlo methods, helps account for the variability and uncertainties in earthquake characteristics and their impact on liquefaction-induced settlements.

In this project, empirical approaches, which rely on correlations derived from historical liquefaction events and field test data are adopted. These methods use simplified parameters to estimate settlement based on past experiences. They are relatively straightforward and easy to apply, though sometimes limited by their dependence on specific case studies and conditions. Common empirical methods include:

Tokimatsu and Seed (1987). This widely used method relates the results of Standard Penetration Tests (SPT) or Cone Penetration Tests (CPT) to the amount of post-liquefaction settlement. It involves determining the factor of safety against liquefaction and using empirical curves to estimate settlements based on soil density and the Cyclic Stress Ratio (CSR).

Ishihara and Yoshimine (1992). This method provides an empirical relationship between the vertical deformation induced by liquefaction and the factor of safety, with settlement calculated by multiplying the vertical strain by the thickness of the liquefied layers.

Simplified analytical methods use a combination of empirical correlations and analytical equations. They often involve calculating the Cyclic Stress Ratio (CSR) and comparing it with the Cyclic Resistance Ratio (CRR) of the soil to estimate the triggering of liquefaction. Once the triggering is assessed, settlements are estimated using volumetric or strain-based deformation models. Examples include:

Idriss and Boulanger (2008). This method refines previous empirical approaches by incorporating updated data on seismic hazard and soil characteristics, and provides more detailed guidelines for estimating liquefaction triggering and the resulting soil deformation.

Zhang et al. (2002). This CPT-based method estimates post-liquefaction settlements using cone tip resistance to evaluate liquefaction potential and the corresponding settlements in each soil layer. The authors correlated the volumetric deformations induced by the dissipation of excess pore water pressure with FS (Factor of Safety) and qc1Ncs (normalized cone penetration resistance) as shown in Figure 10.

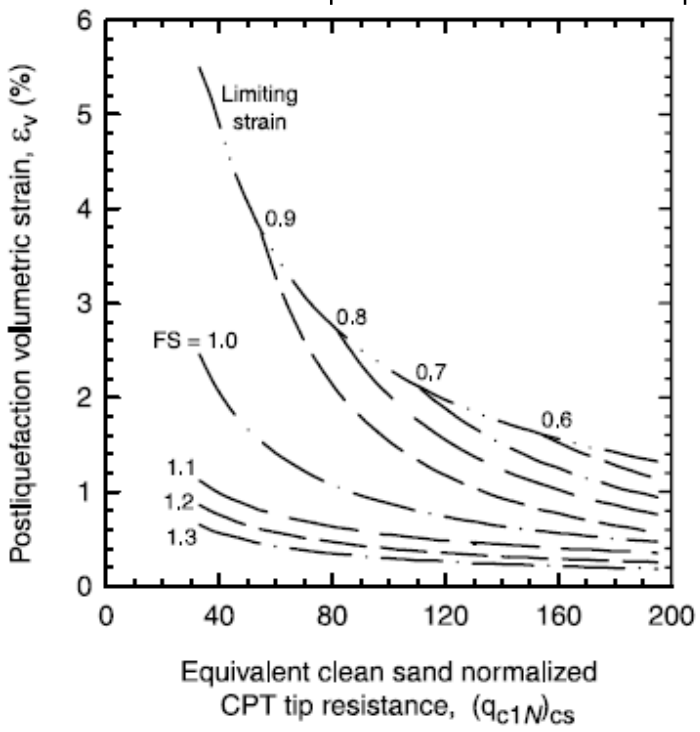

Figure 10. Relationship between post-liquefaction volumetric strain and the clean sand equivalent normalized CPT tip resistance for different factors of safety (FS).

The equations are the following:

$$
\begin{aligned}
if\ FS \le 0.5, \quad & \varepsilon_v = 102 \cdot (q_{c1ncs})^{-0.82} && for\ 33 \le q_{c1ncs} \le 200 \\
if\ FS = 0.6, \quad & \varepsilon_v = 102 \cdot (q_{c1ncs})^{-0.82} && for\ 33 \le q_{c1ncs} \le 147 \\
if\ FS = 0.6, \quad & \varepsilon_v = 2411 \cdot (q_{c1ncs})^{-1.45} && for\ 147 \le q_{c1ncs} \le 200 \\
if\ FS = 0.7, \quad & \varepsilon_v = 102 \cdot (q_{c1ncs})^{-0.82} && for\ 33 \le q_{c1ncs} \le 110 \\
if\ FS = 0.7, \quad & \varepsilon_v = 1701 \cdot (q_{c1ncs})^{-1.42} && for\ 110 \le q_{c1ncs} \le 200 \\
if\ FS = 0.8, \quad & \varepsilon_v = 102 \cdot (q_{c1ncs})^{-0.82} && for\ 33 \le q_{c1ncs} \le 80 \\
if\ FS = 0.8, \quad & \varepsilon_v = 1690 \cdot (q_{c1ncs})^{-1.46} && for\ 80 \le q_{c1ncs} \le 200 \\
if\ FS = 0.9, \quad & \varepsilon_v = 102 \cdot (q_{c1ncs})^{-0.82} && for\ 33 \le q_{c1ncs} \le 60 \\
if\ FS = 0.9, \quad & \varepsilon_v = 1430 \cdot (q_{c1ncs})^{-1.48} && for\ 60 \le q_{c1ncs} \le 200 \\
if\ FS = 1.0, \quad & \varepsilon_v = 64 \cdot (q_{c1ncs})^{-0.93} && for\ 33 \le q_{c1ncs} \le 200 \\
if\ FS = 1.1, \quad & \varepsilon_v = 11 \cdot (q_{c1ncs})^{-0.65} && for\ 33 \le q_{c1ncs} \le 200 \\
if\ FS = 1.2, \quad & \varepsilon_v = 9.7 \cdot (q_{c1ncs})^{-0.69} && for\ 33 \le q_{c1ncs} \le 200 \\
if\ FS = 1.3, \quad & \varepsilon_v = 7.6 \cdot (q_{c1ncs})^{-0.71} && for\ 33 \le q_{c1ncs} \le 200 \\
if\ FS = 2.0, \quad & \varepsilon_v = 0 && for\ 33 \le q_{c1ncs} \le 20
\end{aligned}
$$

3.4 Application of the tool chain in Emilia Romagna (North Italy)

In order to apply the tool chain for liquefaction phenomena, a study area in Emilia Romagna Region has been chosen. Indeed, in May 2012, Italy was struck by an important seismic sequence. The main shock occurred on 20 May 2012 (M_w=6.1) and caused extensive liquefaction phenomena. The part of the country which was affected by these violent shakes was the area of the river Po Valley, in the foreland basin of two mountain chains constituted by the Alps and the northern Apennine, in the Emilia-Romagna Region (Northern-Italy). Since 19 May 2012, Emilia Romagna and surrounding parts of Veneto and Lombardia are hit by a long seismic sequence characterized by about two thousand of shakes. Many

buildings collapsed and 27 victims were recorded. The epicentre of the 20 May event (44.89°N latitude and 11.23°E longitude) was located between the provinces of Modena and Ferrara, while the hypocentre was at a depth of 6.3 km, owing to that it is considered a shallow earthquake (Lai et al., 2015). This event was extremely interesting in Italian seismic literature. It is due to the rarity of so extended soil liquefaction phenomena in Italy. Although Italy is a seismic country, liquefaction occurred only in restricted areas and owing to that the induced damage was generally limited. The most evident effects of liquefaction phenomena following the 2012 earthquake were found in San Carlo (Municipality of Sant'Agostino) and Mirabello, whose subsoil was characterized by alluvial sediments of different depositional environment, which consists of alternated layers of silty-clayey deposits and sandy soils mainly constituting ancient rivers banks (Chiaradonna et al., 2018). The effects of liquefaction induced by the 2012 Northern Italy earthquake, have been recorded and reported in several research works (Lai et al., 2015; Lombardi and Bhattacharya, 2014; Sciarra et al., 2012; Vannucchi et al., 2012). As an example, some photos have been reported in Figure 11 (Vannucchi et al., 2012), where the typical effects of liquefaction may be noted, such as sand boils, vents, sinkholes, craters, surface ruptures, extensional fissures. Many open spaces, as courtyards, gardens and roads, were completely covered by the ejected sand, mud and water.

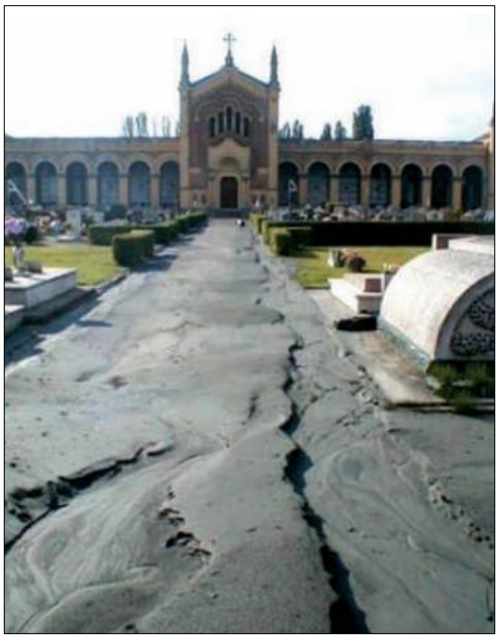

(a)

(b)

(c)

(d)

Figure 11. Liquefaction evidence at San Carlo: main roads covered by grey silty sand ejected from the ground in San Carlo (a); garage (b); sand boils (c) and a private house (d) (Vannucchi et al., 2012).

The study area for the application of liquefaction tool chain was selected considering a sector with the highest concentration of events occurred during the 2012 earthquake. In addition, data for develop the tool chain were collected, such as geological and geotechnical investigations, water table depth, and PGA values. In particular, the geological and geotechnical investigations were obtained from the database created by the Geology, Soil, and Seismic Area of the Emilia-Romagna Region. The water table depth values were obtained by interpolating the average groundwater levels from point data downloaded from the ARPAE database (Regional Agency for Prevention, Environment, and Energy of Emilia-Romagna). This data refers to the monitoring conducted from 2009 to 2022 at the underground water body stations belonging to the regional network for environmental quality. Finally, the PGA (Peak Ground Acceleration) values related to the 2012 Emilia earthquake with a magnitude of 5.8 were obtained from the INGV archive. By using these data the application and validation of the tool-chain was carried out.

3.4.1 Results of Level 1 susceptibility

The susceptibility map of level 0 was elaborated applying a GIS intersection of geological/geomorphological and the water table maps following the logical scheme of Figure 4. In particular, by means of some studies of literature (Civico et al., 2015; Minarelli et al., 2022; Priolo et al., 2012; Stefani et al., 2018) and boreholes available in the study area, a map was drowned complying with the Youd and Perkins's classification (Figure 12). The groundwater table level was obtained by interpolation of water table depth point values among the monitoring database of ARPAE (Regional Agency for Prevention, Environment and Energy of Emilia-Romagna) stations (Figure 12).

On the other hand, the susceptibility map of level 1, was elaborated applying a GIS intersection of geological/geomorphological, the water table and PGA maps. The latter is related to the 2012 Emilia earthquake with a magnitude of 5.8 and shows that the liquefaction evidence is within the range of 0.18 - 0.30 g. Few points are present for PGA values less than 0.18 g (Figure 13).

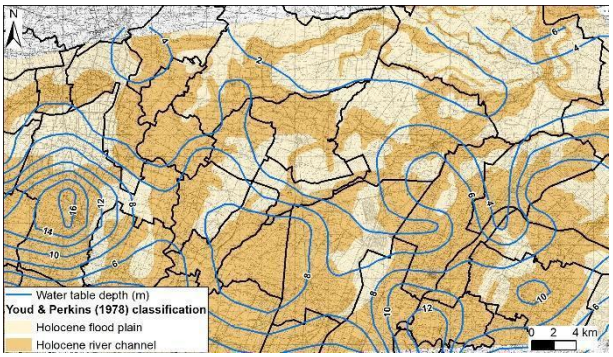

Figure 12. Geological/geomorphological setting following Youd & Perkins (1978) and mean water table depth.

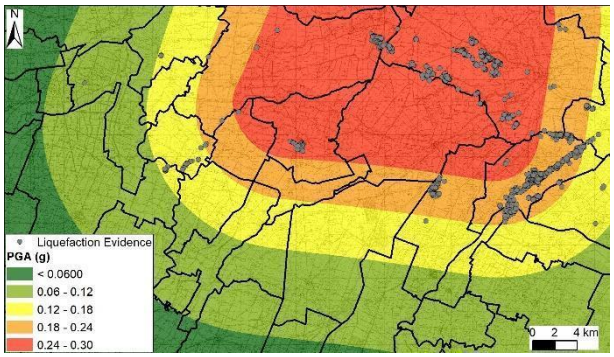

Figure 13. PGA map referred to 2012 Emilia earthquake with magnitude of 5.8

The susceptibility maps of levels 0 and 1 for liquefaction phenomena was shown respectively in

Figure 14 and Figure 15. The water table depth of the area is always less than 15 meters, therefore in the first scenario the result class zonation depends on the distribution of Holocene flood plain and river channel deposits, while in the second one it is evident also the contribution of the PGA. The majority of liquefaction events fall within the high and very high susceptibility class.

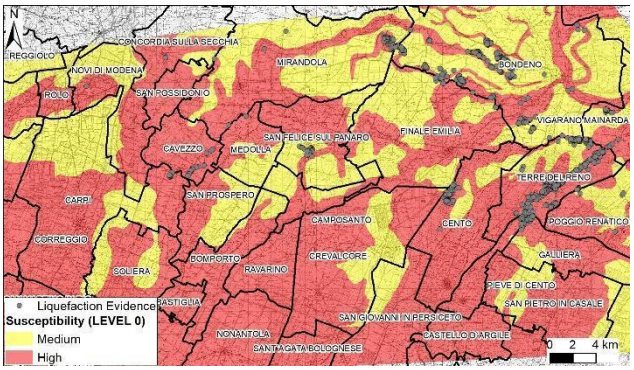

Figure 14. Susceptibility map of level 0 and liquefaction evidence.

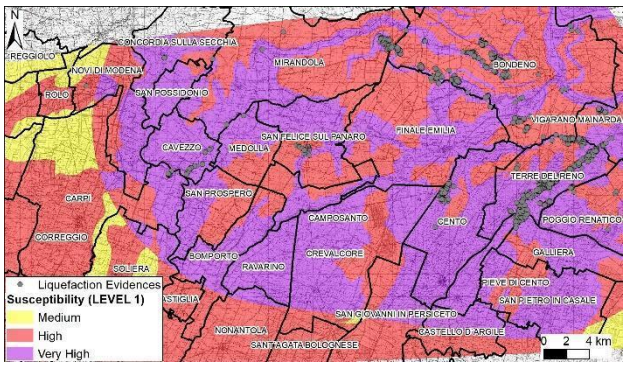

Figure 15. Susceptibility map of level 1 and liquefaction evidence.

In order to obtain a liquefaction map based on the semi-empirical stress based approach of Idriss and Boulanger (2008), (Boulanger and Idriss, 2014), the geotechnical investigations (CPT or SPT) are necessary. For the study area more than two thousand points representing CPT investigations are available that could be interpolated and used to elaborate a susceptibility map of level 2.

A first attempt was made estimating the LPI index for 12 CPT points localized neighboring the high concentration of liquefaction events and close to borehole with evidence of sand layers interbedded to silt and clay (Figure 16).

Following the procedure described in figure 3 and using the equation 5 the LPI (Liquefaction potential index) was estimated. For 11 examined points the LPI values ranged from 6.8 and 14 with high potential failure index; while one data shows LPI value of 21.9 with very high potential failure index (Figure 17).

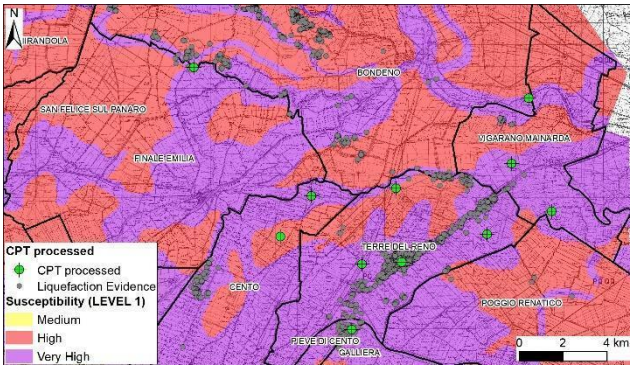

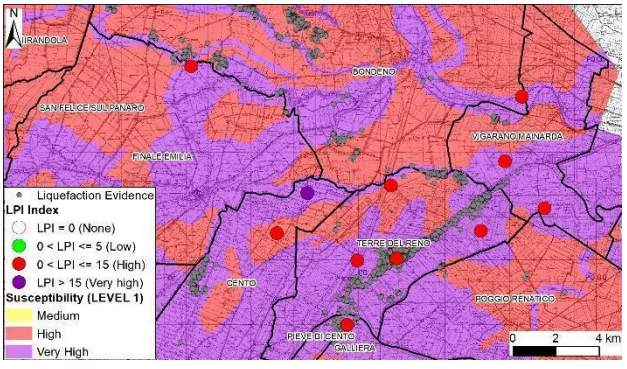

Figure 16. CPT investigations distribution for LPI index evaluation

Figure 17. LPI index classes distribution

3.4.2 *Results of Level 2 Susceptibility*

In the area selected for the application of the toolchain, 2035 CPTs are available, and for each of them, the depth of the groundwater table was calculated. Subsequently, using a script, it was possible to evaluate for some of them the Factor of Safety (FS) at each depth and the LPI (Liquefaction Potential Index) representative of the entire vertical, as developed by Iwasaki et al. (1984).

A total of 203 CPTs were processed, of which 131 were representative of liquefiable sandy layers, and 72 were located in areas without sandy layers and therefore not suitable for liquefaction assessment.

Figure 18 shows an example of a processed CPT, illustrating the presence of liquefiable and non-liquefiable layers and the variation of the Factor of Safety along the vertical axis z.

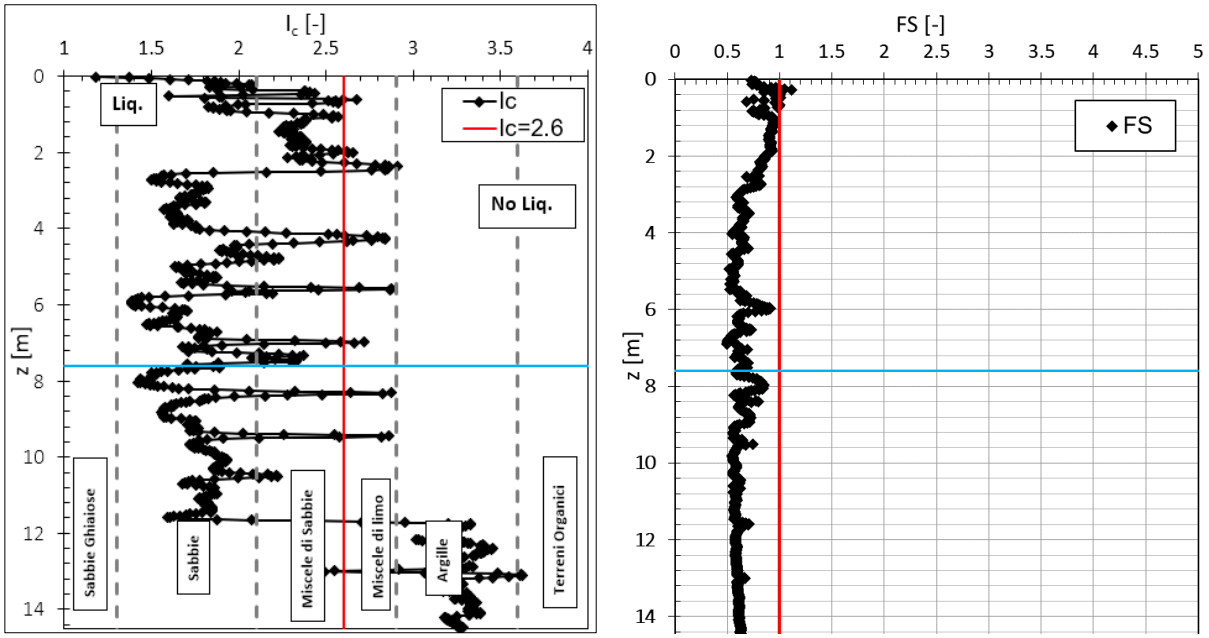

Figure 18. Representation of the liquefiable and not-liquefiable layers and their FS along the z profile.

Figure 19 shows the spatial distribution of the entire CPT dataset available in the test area, as well as those used for the calculation of the factor of safety and settlements. Specifically, the blue points indicate CPTs that are not suitable for liquefaction assessment because they are located in areas where the stratigraphy is predominantly characterized by clayey layers, with thin or absent sandy strata. The green dots indicate the CPTs that were processed, because they are located in areas with potentially liquefiable sandy layers. Finally, the grey points represent the CPTs that will be processed at a later stage.

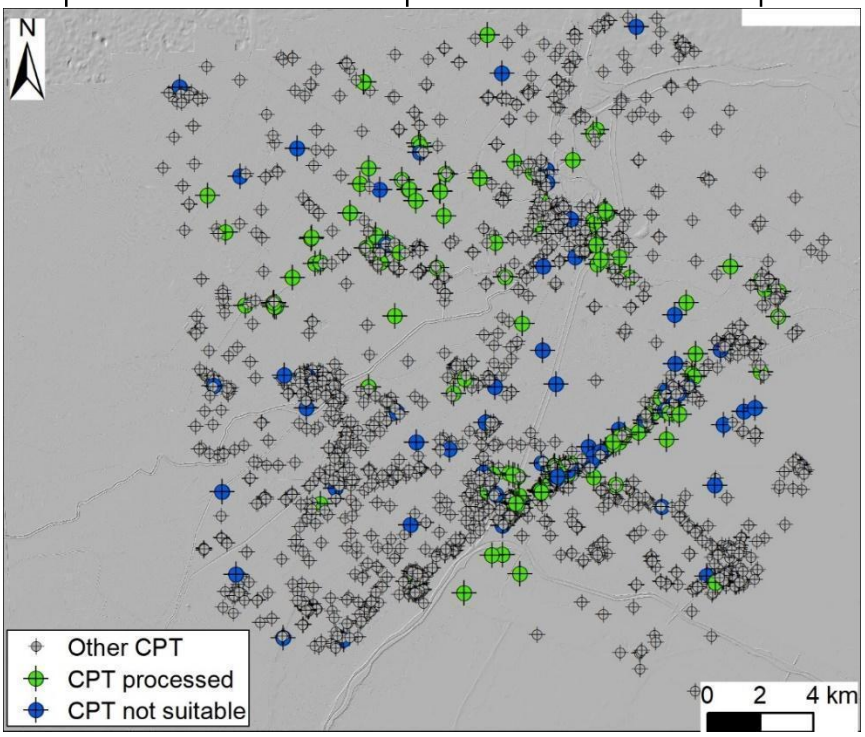

Figure 19. Spatial distribution of the available CPT data in the test area, highlighting processed and unprocessed data for liquefaction assessment.

For the processed data, the Liquefaction Potential Index (LPI) and settlements were calculated considering four reference scenarios, obtained by varying two of the three factors that influence the phenomenon—namely, the preparatory conditions and the trigger.

In the first case, the preparatory factor considered was the variation in the groundwater table depth, ranging from the ground surface (depth = 0) to values obtained from an average map of groundwater level contours, based on monitoring carried out between 2009 and 2022 by the Emilia-Romagna Region.

As for the triggering event—represented by an earthquake—the variation parameter considered was the PGA (Peak Ground Acceleration). Specifically, the adopted values follow the macro-seismic classification of Italy (NTC, 2018), which divides the country into different seismic zones based on risk, classified from Zone 1 (highest risk) to Zone 4 (very low risk). Each zone corresponds to a specific PGA value:

- Zone 1: PGA ≥ 0.25 g High seismic hazard. Earthquakes can be very strong and frequent;

- Zone 2: 0.15 g ≤ PGA < 0.25 g Medium-high hazard. Earthquakes can be intense but less frequent;

- Zone 3: 0.05 g ≤ PGA < 0.15 g Moderate hazard. Earthquakes may occur but are generally less intense;

- Zone 4: PGA < 0.05 g Low seismic hazard. Earthquakes are rare and of low intensity.

For simplicity, the studied values refer to Zone 1 and Zone 2, as the analyzed process requires a high-energy earthquake for triggering. Therefore, the proposed analysis of the Liquefaction Potential

Index (LPI) was carried out following four scenarios:

- Scenario 1 (IL_1):

  Groundwater depth: average depth values from 2009 to 2022

  PGA: 0.15 g

- Scenario 2 (IL_2):

  Groundwater depth: average depth values from 2009 to 2022

  PGA: 0.25 g

- Scenario 3 (IL_3):

  Groundwater depth: 0

  PGA: 0.15 g

- Scenario 4 (IL_4):

  Groundwater depth: 0

  PGA: 0.25 g

Considering the four scenarios, the Liquefaction Potential Index (LPI) was calculated for each investigation by modifying both the preparatory factor (groundwater depth) and the triggering factor (PGA). Figure 18 shows the spatial distribution of LPI values for each scenario (IL). It is evident that from Scenario 1 (IL_1) to Scenario 4 (IL_4), the conditions worsen, as the groundwater table is assumed to be at the surface (IL_3 and IL_4), or the PGA increases (IL_2 and IL_4), as shown in Figure 20.

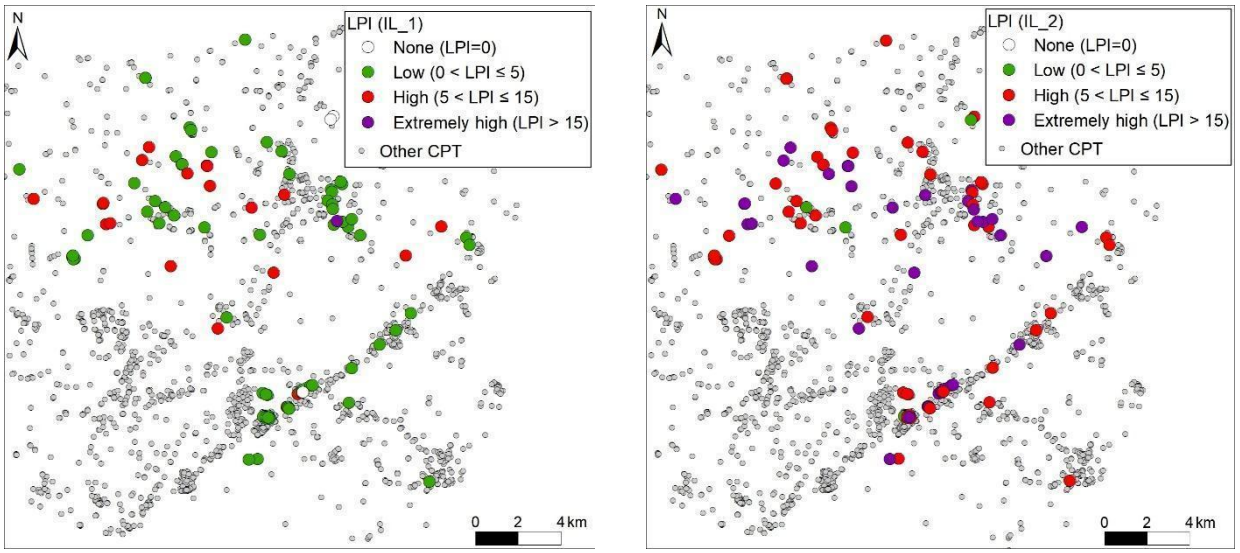

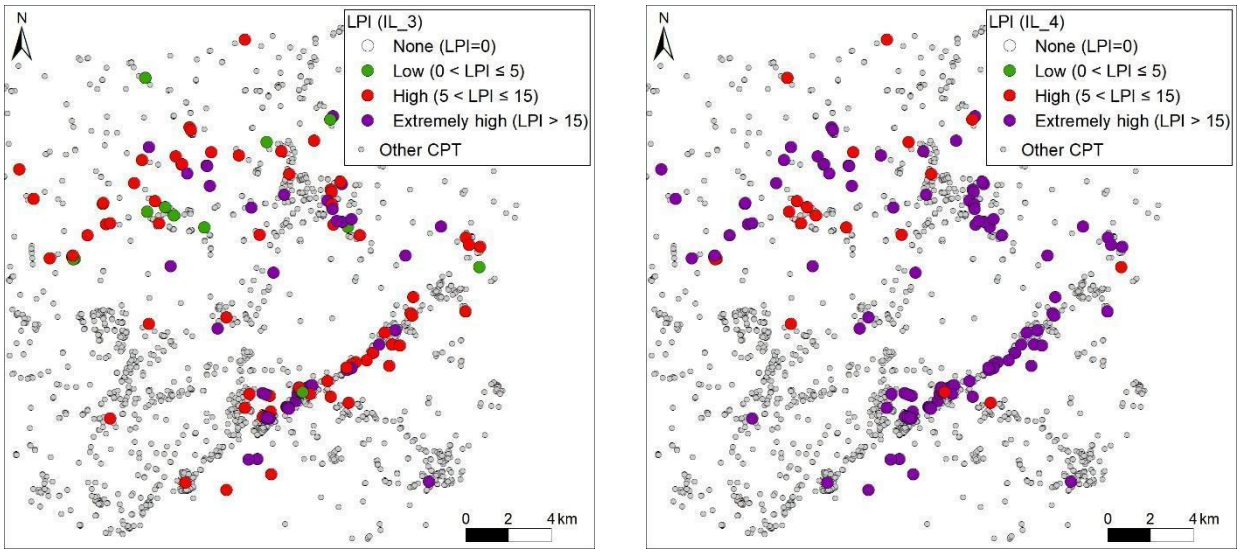

Figure 20. Spatial distribution of the Liquefaction Potential Index (LPI) for each scenario.

In addition to the spatial distribution of the points, a statistical analysis was also conducted on all the processed data to evaluate the variability, even if only partial. Figure 21 shows the statistics related to the LPI values and a boxplot for each scenario. One can observe how the variability of the data changes from Scenario 1 to Scenario 4, with a noticeable increase in Scenario 4. In fact, the standard deviation rises from 3.3 in Scenario 1 to 10.5 in Scenario 4. IL_2 and IL_3 are similar in terms of distribution and variability.

The plots in Figure 22 show the distribution of LPI classes for each scenario. The IL_1 chart shows that most observations fall into the "low" category, with about 70% of the events. Fewer observations are found in the "high" category, while the "very high" category shows almost no occurrences, suggesting that high liquefaction potential is rare in Scenario IL_1.

In the case of IL_2, the distribution shifts toward higher liquefaction index values. Most observations fall into the "high" category, with nearly 40% of the cases, and a significant portion also falls into the "very high" category, with about 30% of the observations. These results are due to the increase in the PGA value (from 0.15 g to 0.25 g).

Finally, for Scenarios IL_3 and IL_4, there is a clear trend toward higher LPI levels, though in distinct ways. IL_3 has most of its observations concentrated in the "high" category, with a significant number also falling under "very high." In contrast, Scenario IL_4 shows an even more extreme concentration in the "very high" category, where the majority of observations are found (about 80% of occurrences).

Statistic	IL_1	IL_2	IL_3	IL_4
N. of observations	131	131	131	131
Minimum	0.0	1.8	1.3	6.1
Maximum	17.0	41.0	38.7	58.1
1st Quartile	0.6	8.8	8.8	17.1
Median	1.2	11.7	12.3	22.5
3rd Quartile	4.3	18.5	18.3	31.7
Mean	2.8	14.0	14.2	24.8
Variance	10.9	56.5	67.1	111.2
Standard deviation	3.3	7.5	8.2	10.5

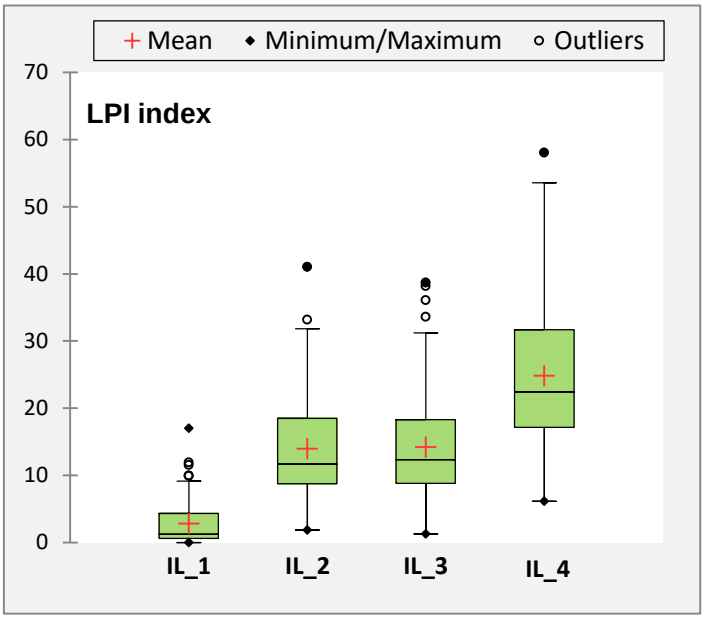

Figure 21. Statistics and boxplot of LPI.

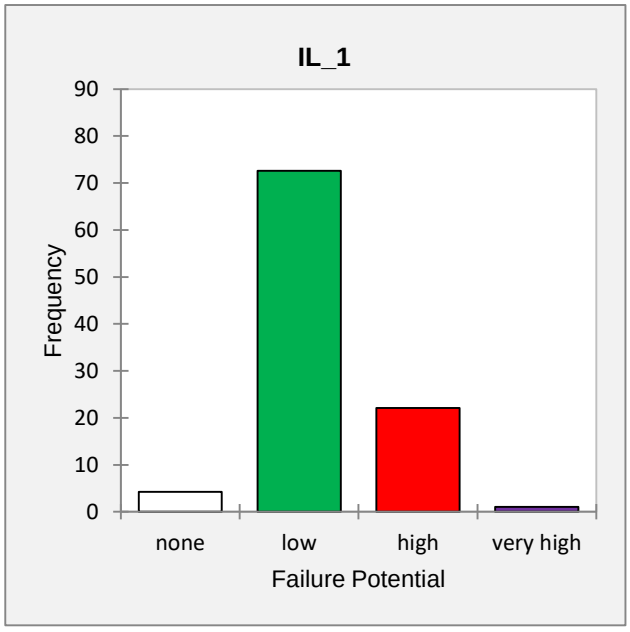

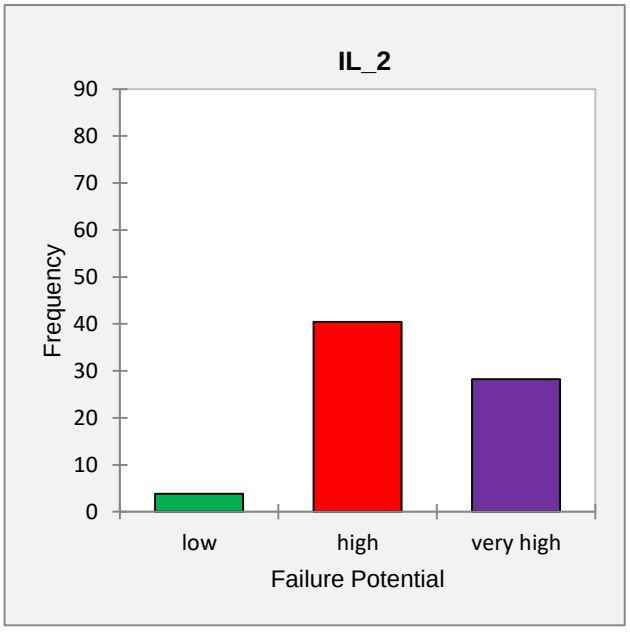

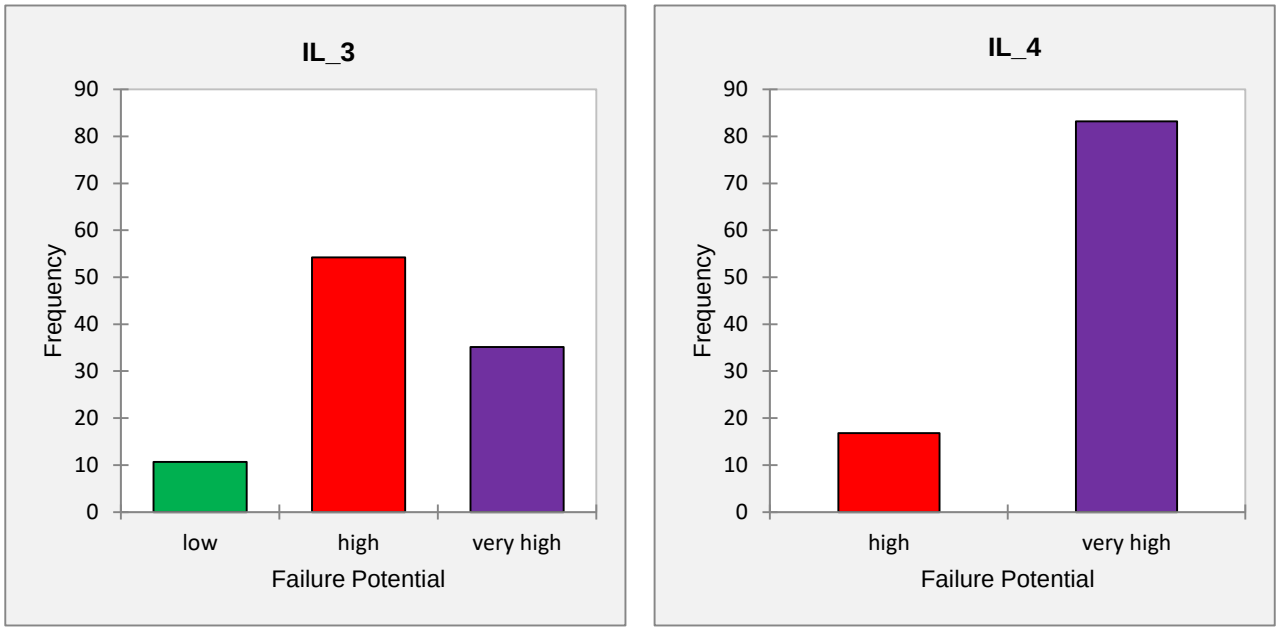

Figure 22. Frequency distribution of LPI classes in each scenario.

3.4.3 *Settlements assessment*

Based on the equations described in the previous section, settlements were evaluated for each reference scenario (Figure 23). In particular, for Scenario 1, the distribution of settlement values shows significant variation in the intensity of the phenomenon. Most points are characterized by very low settlements (< 0.05 m), distributed across various areas, indicating that a large part of the territory does not experience significant deformation. Settlements between 0.05 and 0.10 m are more widely distributed and cover a broader area, while values between 0.10 and 0.20 m are less frequent and concentrated in specific locations. Finally, high settlements represent a small portion of the overall distribution but highlight the most critical zones, with values ranging between 0.20 and 0.40 meters.

In Scenario 2, the distribution of values is similar to that of Scenario 1, with settlement values mainly concentrated in the low and very low categories, and a few localized areas showing more significant settlements.

In Scenario 3, most points fall within the very low and low settlement categories (< 0.1 m); however, compared to the previous maps, there is a slight expansion of areas with moderate and high settlements, although still concentrated in specific regions.

Finally, Scenario 4 shows a relative increase in settlement, particularly for values below 0.1 m. A distribution similar to the previous scenario (Scenario 3) is observed for values above 0.1 m.

The statistics in Figure 24 confirm the progressive increase shown in the maps from Scenario 1 to Scenario 4. Furthermore, in this case, the data also show greater dispersion in Scenarios 3 and 4 compared to Scenarios 1 and 2.

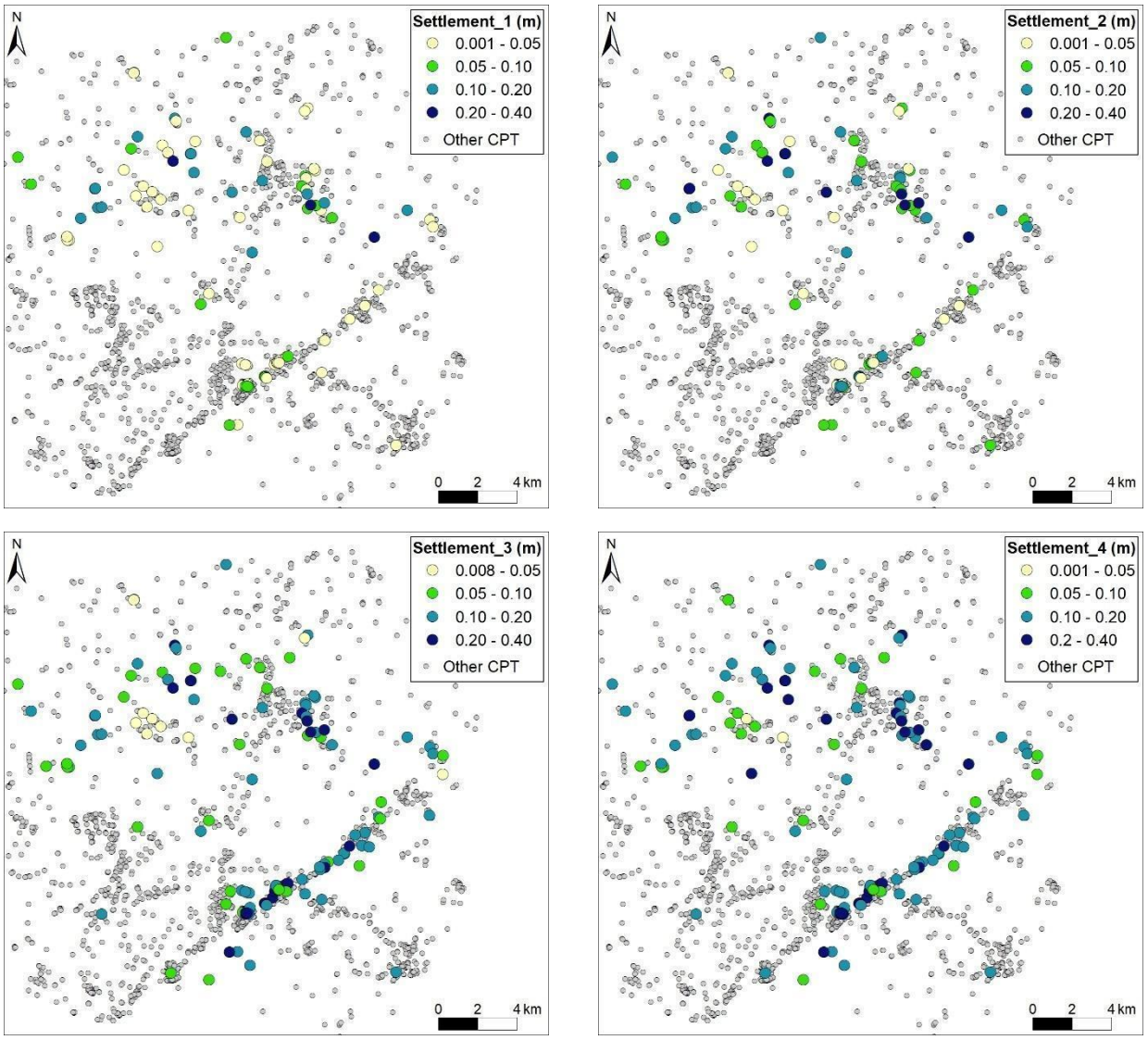

Figure 23. Spatial distribution of the settlements for each scenario.

Statistic	Sett_1	Sett_2	Sett_3	Sett_4
N. of observations	131	131	131	131
Minimum	0.00	0.00	0.01	0.02
Maximum	0.30	0.34	0.37	0.39
1st Quartile	0.02	0.05	0.09	0.11
Median	0.04	0.09	0.12	0.14
3rd Quartile	0.08	0.12	0.18	0.20
Mean	0.06	0.10	0.14	0.16
Variance	0.00	0.01	0.01	0.01
Standard deviation	0.06	0.07	0.07	0.08

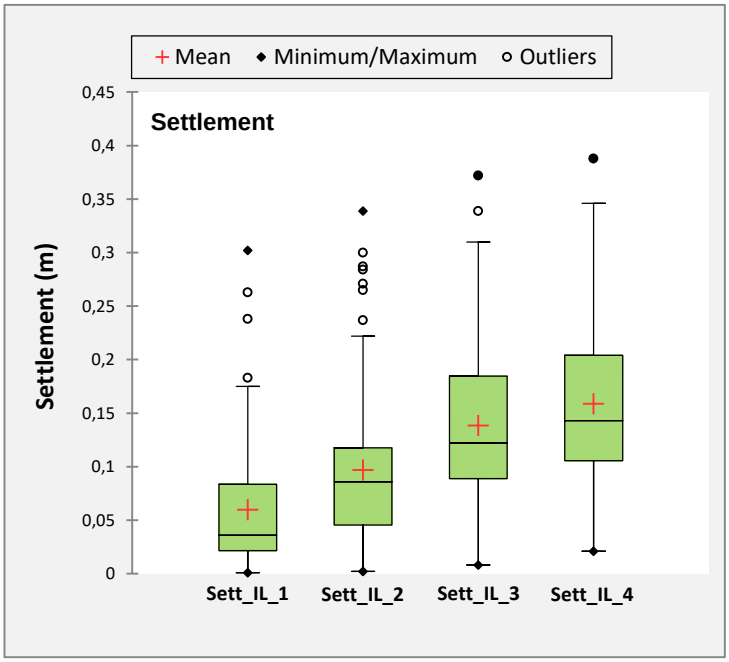

Figure 24. Statistics and boxplot of the settlements.

3.4.4 *Spatial analysis*

In order to develop a simple methodology for spatializing the results within a specific area while avoiding complex interpolation methods, a grid-based map was proposed in which each cell displays averaged values from the available investigations. The grid size can be adjusted based on the study area's extent and the number of available investigations. In this case, a grid with 2x2 km cells was created. Figure 25 shows the number of available and processed CPTs within each grid cell.

Specifically, Figure 25c shows that the density of investigations is quite variable—some cells contain fewer than 15 CPTs (in the northwestern area), while others have more than 15 investigations. As for the processed CPTs, the map shows a concentration of data processing in the central areas, with higher numbers (indicated in pink and purple) and lower values (yellow and orange) in the surrounding cells (Figure 25d).

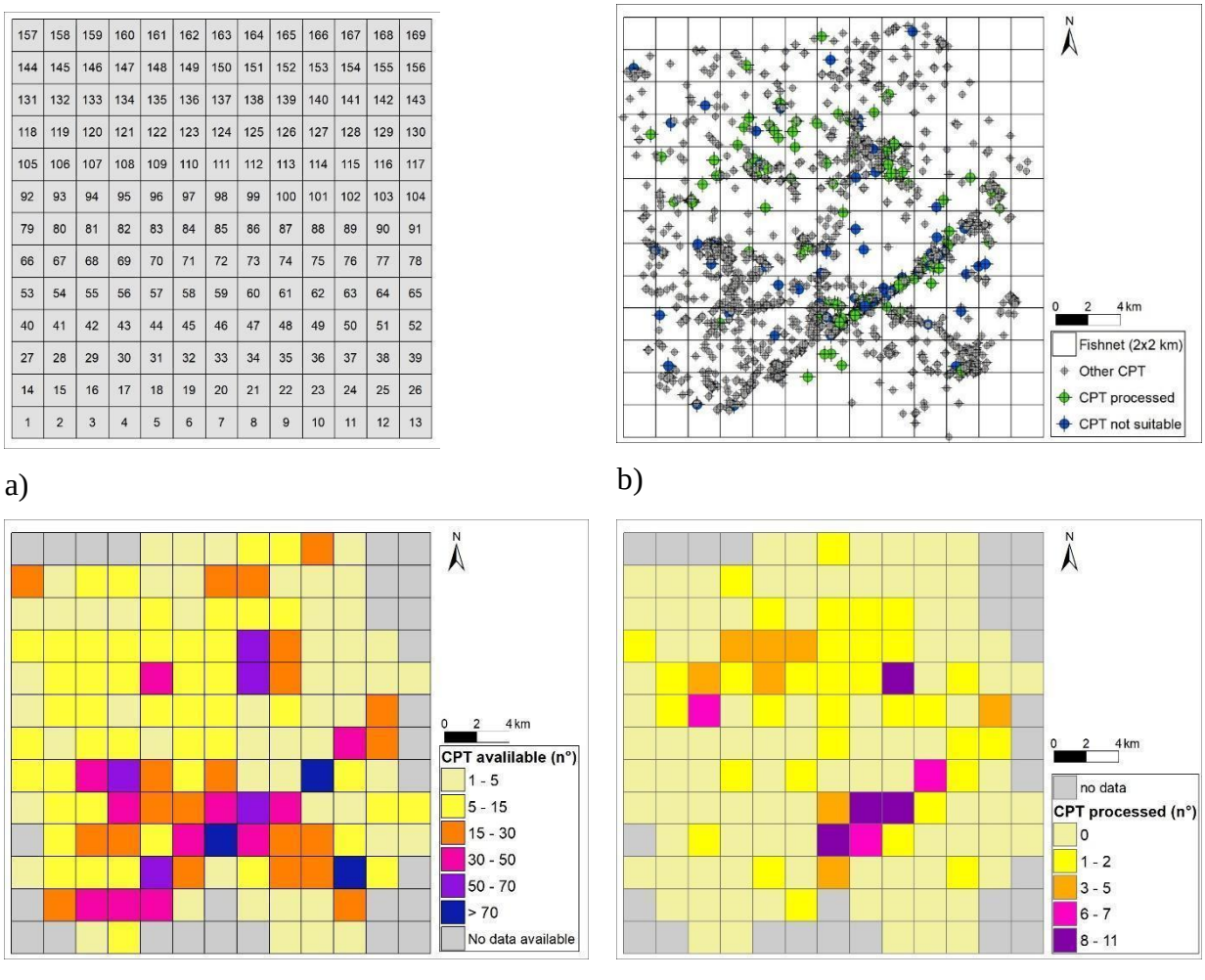

Figure 25. Assigned Cell ID (a); CPT distribution on the grid (b); number of available CPTs in each grid cell (c);

number of processed CPTs in each grid cell (d).

For all the processed data, minimum, maximum, and average values were calculated for each liquefaction scenario, both for the Liquefaction Potential Index (LPI) and for settlement. However, for spatial representation of the data, the average LPI values and the maximum settlement values were selected, as calculated in Table 2. Figure 26 shows the distribution of average LPI values for the four reference scenarios.

Figure 26a displays a scattered distribution of green cells (low LPI values) and red cells (high LPI values) throughout the grid. Most low values are concentrated toward the central and northern zones, while the high values are irregularly distributed. Gray cells indicate a lack of data.

In the map of Figure 26b, there is a significant presence of areas with high and extremely high values for Scenario 2. These areas are particularly concentrated in the central and northern parts of the grid. Light green squares, representing areas with absent or very low values, are more sparsely distributed.

Figure 26c shows a substantial presence of high and extremely high LPI values. Specifically, cells with high LPI (red) are more widely spread, while cells with extremely high LPI (purple) appear in specific central and southern areas. Low values (green) are less frequent but are clustered near the upper and central parts of the map. This distribution highlights the effect of soil saturation on the liquefaction potential index when setting the groundwater depth to field level (0 m).

Finally, Figure 26d shows a clear increase in LPI, with extremely high values more widespread across the area and no low values present. This distribution of elevated values results from the worsening of both preparatory and triggering parameters in Scenario 4, where the groundwater level is at zero and PGA is 0.25 g.

Table 2. Mean value of the LPI and maximum values of the settlements calculated for each cell.

ID cella	TOT data	next data	data processed	IL_1 mean	IL_2 mean	IL_3 mean	IL_4 mean	SETTL_1 max	SETTL_2 max	SETTL_3 max	SETTL_4 max
19	1		1			13.64	18.16			0.082	0.082
31	54	53	1			9.96	16.45			0.097	0.106
33	4	1	3	2.89	16.76	20.46	28.68	0.051	0.061	0.201	0.201
37	84	83	1	0.27	10.51	15.32	27.11	0.011	0.054	0.155	0.171
42	20	19	1			11.14	21.04			0.106	0.114
46	115	105	10	1.31	11.49	17.53	29.11	0.082	0.108	0.249	0.249
47	39	32	7	2.25	18.34	22.75	35.80	0.114	0.124	0.339	0.341
48	30	29	1	0.15	6.24	7.09	11.87	0.028	0.096	0.121	0.122

59	32	27	5	0.82	10.96	14.41	22.77	0.006	0.025	0.133	0.143
60	60	49	11	3	18.11	20.40	31.45	0.053	0.115	0.297	0.298
61	40	31	9	0.23	13.61	13.85	24.85	0.012	0.051	0.212	0.230
62	1		1			10.87	15.17			0.081	0.082
69	52	51	1			5.16	12.11			0.054	0.072
71	14	12	2	3.19	13.32	16.52	24.33	0.055	0.056	0.190	0.190
75	101	94	7	2.04	13.73	14.86	24.76	0.006	0.022	0.247	0.248
76	10	9	1			8.87	18.91			0.095	0.109
85	11	10	1	6.38	18.41	22.19	31.97	0.100	0.105	0.171	0.171
89	37	35	2	0.06	8.72	11.13	19.35	0.015	0.084	0.120	0.178
90	21	20	1			13.71	27.45			0.130	0.151
93	11	10	1			14.47	19.09			0.094	0.094
94	11	5	6	1.72	10.18	6.68	15.56	0.122	0.132	0.173	0.179
96	12	11	1	5.02	18.11	20.55	32.19	0.030	0.036	0.182	0.204
98	13	12	1	1.13	5.69	7.91	14.78	0.018	0.033	0.068	0.076
100	13	12	1	3.55	20.48	9.47	33.36	0.099	0.195	0.165	0.255
101	5	4	1	11.54	27.93	28.01	45.45	0.263	0.287	0.310	0.328
103	27	23	4	1.07	10.44	8.93	18.58	0.049	0.107	0.130	0.158
106	6	5	1	6.67	15.5	11.13	18.81	0.085	0.099	0.110	0.120
107	8	4	4	7.81	20.98	12.82	25.24	0.165	0.222	0.221	0.240
108	15	14	1	1.18	6.97	4.31	14.05	0.023	0.058	0.042	0.072
109	37	33	4	1.14	6.08	4.46	10.31	0.028	0.059	0.045	0.074
110	9	7	2	3.75	11.2	10.77	17.61	0.128	0.145	0.194	0.204
111	11	10	1	9.95	25.27	22.65	36.06	0.183	0.211	0.248	0.260
112	54	53	1	5.64	17.07	17.55	27.26	0.126	0.149	0.187	0.189
113	30	20	10	3.75	18.06	15.87	31.25	0.302	0.339	0.372	0.388
115	4	3	1	5.77	17.71	18.1	28.78	0.131	0.156	0.172	0.183
118	7	6	1	2.59	12.88	6.35	19.6	0.050	0.110	0.064	0.116
121	8	5	3	5.08	15.7	13.22	23.28	0.119	0.130	0.179	0.185
122	7	3	4	3.39	12.06	13.85	22.84	0.238	0.265	0.304	0.323
123	10	6	4	4.33	23.43	18.07	32.63	0.175	0.300	0.233	0.346
124	11	10	1	0.79	7.55	7.64	18.33	0.034	0.070	0.092	0.123
125	53	52	1	1.6	8.83	6.04	14.02	0.041	0.053	0.076	0.093
126	17	15	2	1.37	11.21	15.84	26.62	0.048	0.079	0.169	0.184
135	15	13	2	0.71	11.56	8.83	21.18	0.117	0.271	0.221	0.325
137	6	5	1	0.05	6.27	4.33	11.86	0.109	0.147	0.056	0.091
138	8	7	1			13.8	20.06			0.089	0.089
139	7	5	2	0	4.39	8.86	23.82	0.009	0.059	0.154	0.210
147	10	8	2	0.70	5.74	2.43	10.09	0.022	0.045	0.032	0.050
163	3	2	1	0.76	6.02	9.68	14.34	0.067	0.161	0.145	0.192

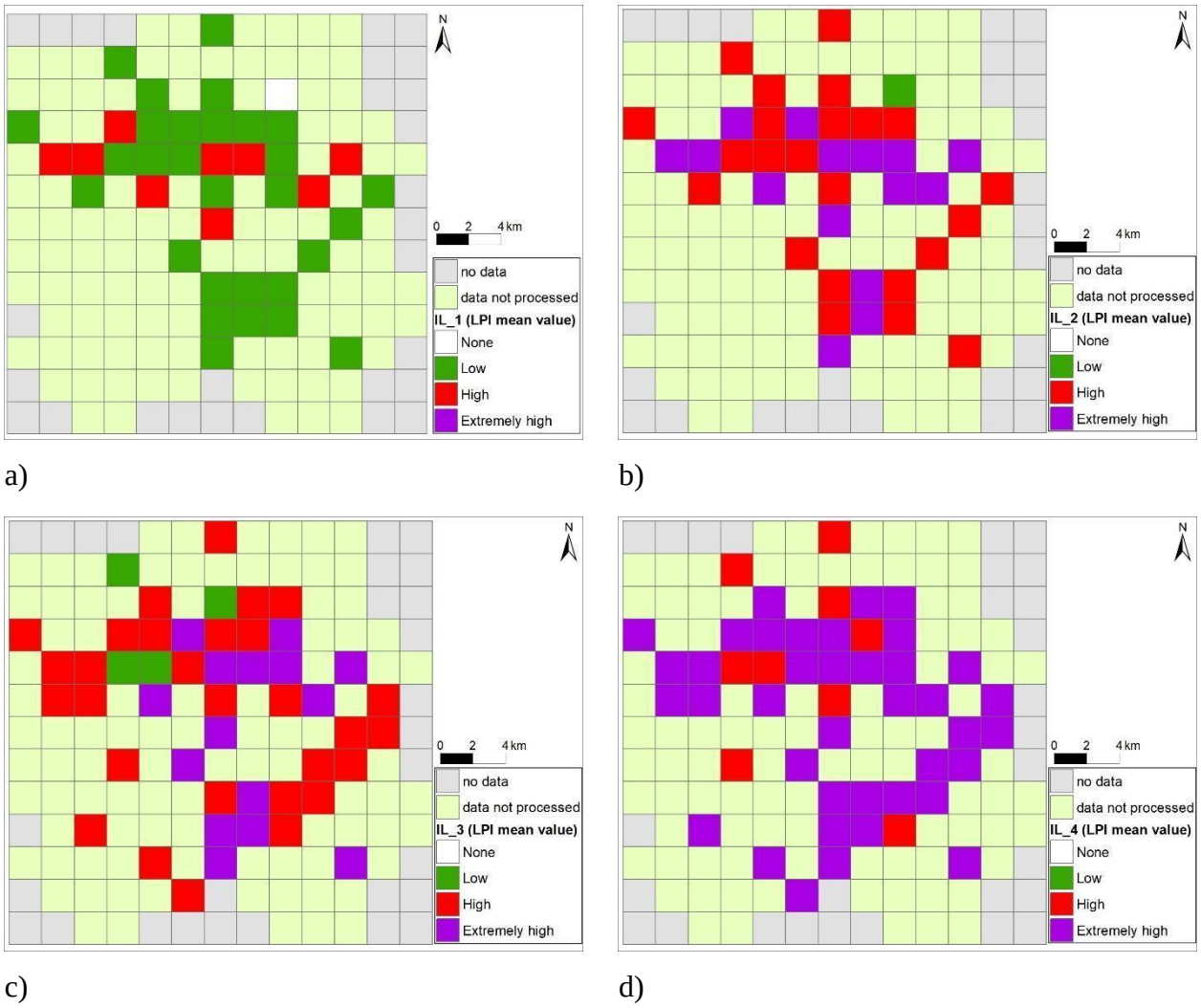

Figure 26 Spatial distributionof the mean value of LPI for a) scenario 1; b) scenario 2; c) scenario 3; d) scenario 4.

Using the maximum settlement values, the spatial distribution was mapped for the four reference scenarios. Figure 27a shows a relatively even pattern of settlements, with a prevalence of low values (in light green and yellow). However, there are some areas in the central strip with values greater than 0.1 m.

In Figure 27b, there are more blue cells compared to the first scenario, with settlement values > 0.1 m concentrated in the same central strip and in some lateral areas. The increased density of cells with higher settlement highlights the worsening conditions compared to Scenario 1.

In Figure 27c, the distribution of settlements < 0.1 m is similar to that of Scenario 2, but with a broader extent, indicating increased severity of settlements in the same areas.

Finally, Figure 27d shows the worst-case scenario, with the highest settlement values (> 0.2 m).

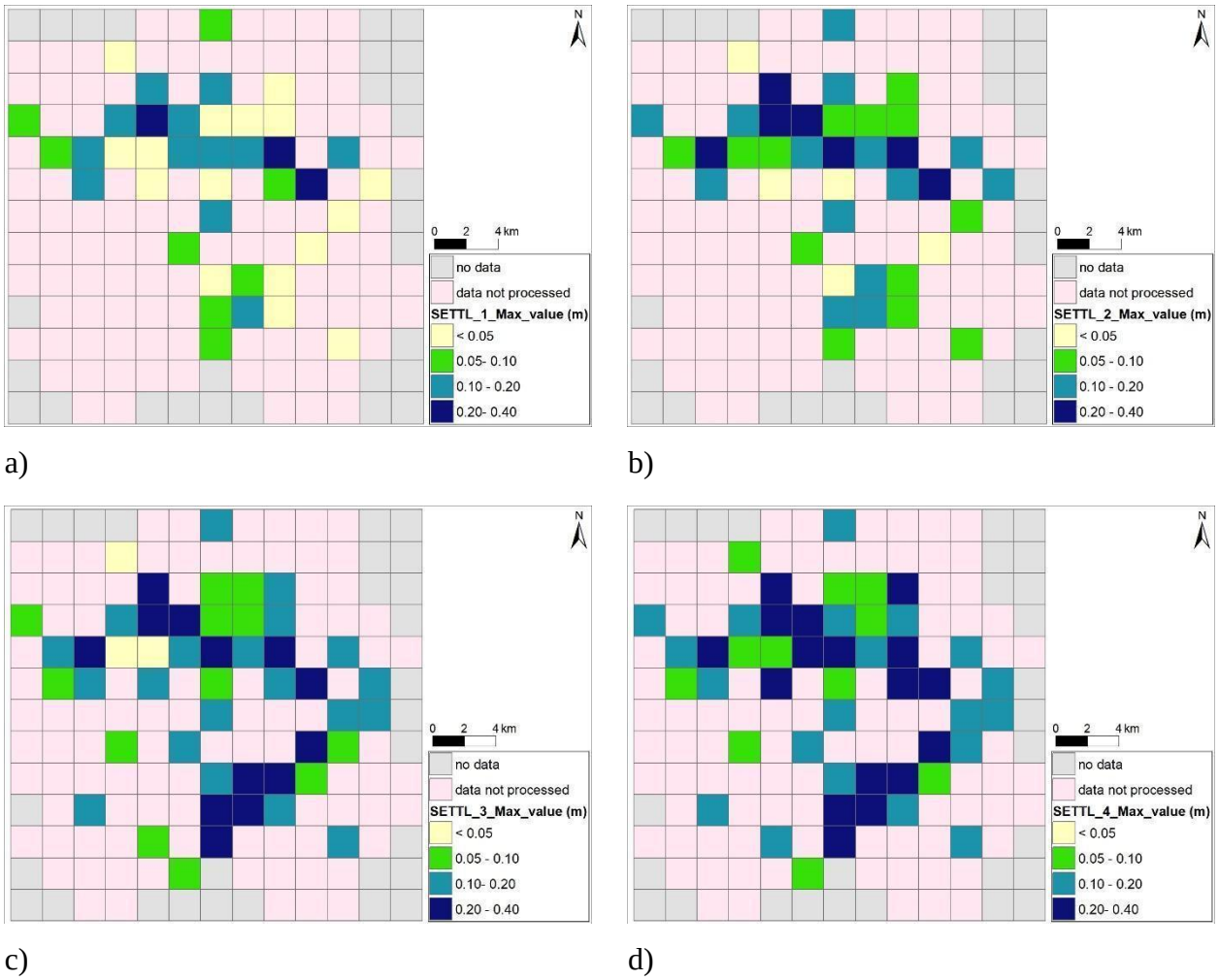

Figure 27. Spatial distribution of the maximum settlement value for a) scenario 1; b) scenario 2; c) scenario 3; d) scenario 4.

3.4.5 *Validation of the results*

The validation phase of the study was conducted based on the historical liquefaction events recorded in the days following the 2012 earthquake. Specifically, by intersecting the points of past evidence with the susceptibility maps of Level 1 and Level 2, both the frequency of these events within each map class and the predictive capacity via the ROC curve were calculated.

As for the Level 1 susceptibility, only the frequency of liquefaction points in each class was assessed, for both the screening map (which considers only lithological groupings) and the map that also incorporates PGA values.

In the first liquefaction susceptibility map (screening level) shown in Figure 14, only the classes “medium” and “high” are present. Historical evidence is mostly distributed in the “high” class (approximately 80%) and to a lesser extent in the “medium” class (around 20%).

In the Level 1 map of Figure 15, which also includes PGA, the present classes are “medium”, “high”, and “very high”. The liquefaction points are mainly distributed in the latter two,

with frequency values of 20% and 80%, respectively.

These results highlight the potential to identify liquefiable areas using a simple-to-apply approach, which can serve as a foundation for further investigations and detailed studies.

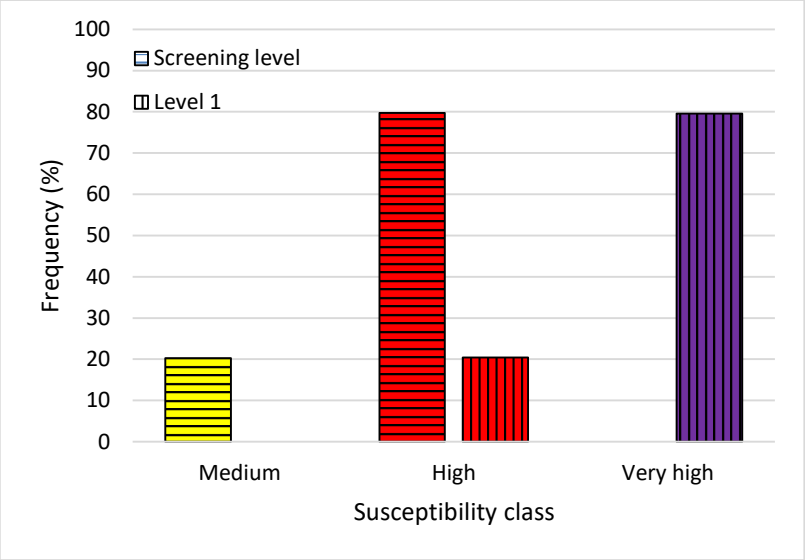

Figure 28. Frequency distribution of historical liquefaction events across different Level 1 susceptibility classes.

As for Level 2 susceptibility, based on the frequencies of events in each LPI class, Scenario 1 in Figure 27a shows that most cases fall into the "low" category, with a low frequency of "high" values and almost no "very high" cases, highlighting a discrepancy between the scenario and historical events. This discrepancy can be explained by the particular nature of the 2012 earthquake, which triggered liquefaction despite not being of very high intensity, but characterized by several close aftershocks. Scenario 2 in Figure 27b shows an increase in frequencies for both the "high" and "very high" categories. This trend is much more evident in the other two scenarios (3 and 4), where the frequency of events in the "very high" category increases from 63% to 96% (Figures 27c and 27d).

The AUC table and ROC curve in Figure 30 confirm this trend, showing that the predictive capacity of the model improves from the first scenario (AUC = 0.5) to the second (AUC = 0.67) and stabilizes in the subsequent scenarios (AUC = 0.69 and 0.68, respectively). This suggests that, for accurate settlement prediction, the most critical scenarios (IL_3 and IL_4) provide better sensitivity.

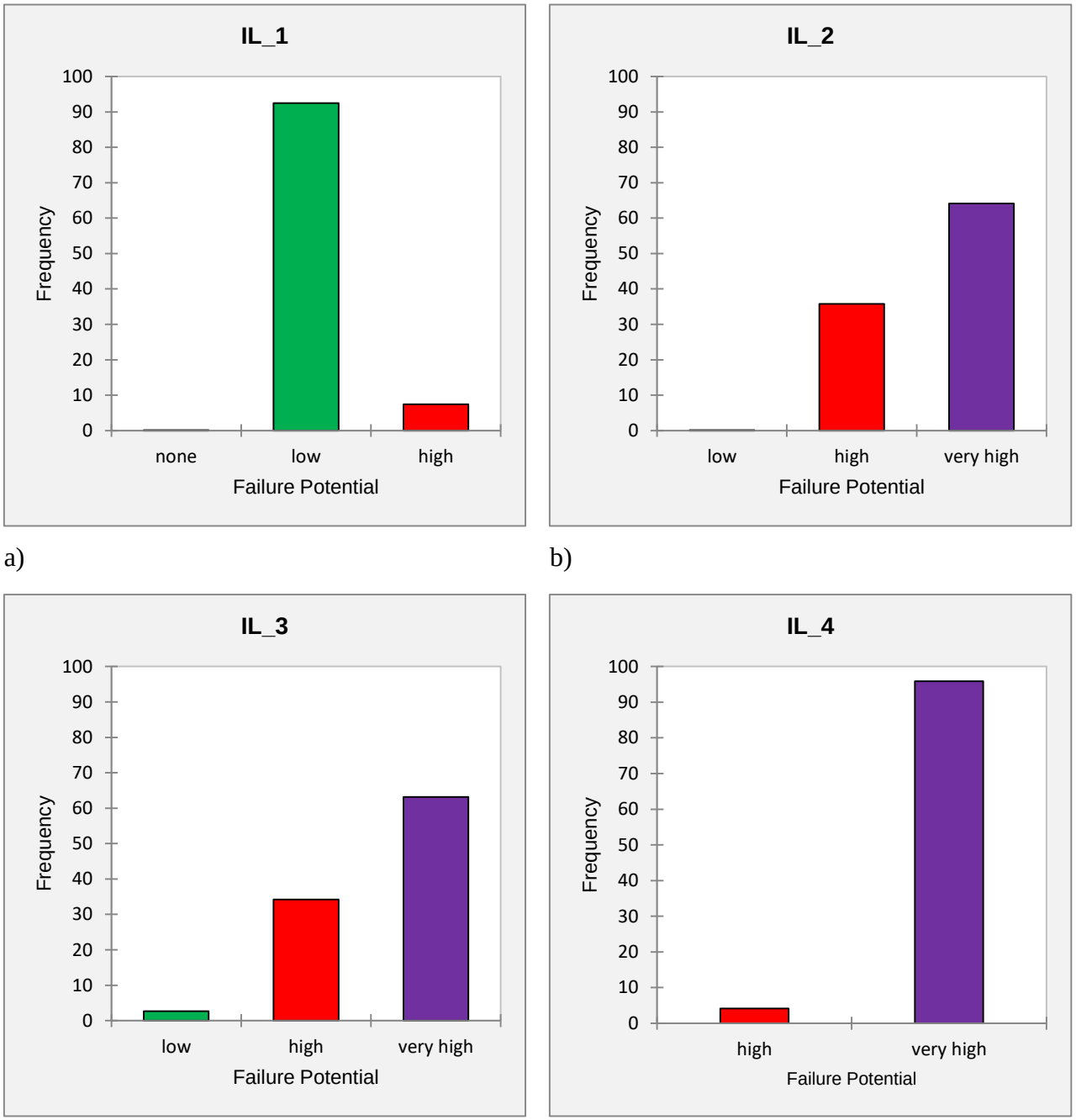

Figure 29. Frequency distribution of the liquefaction occurences in each LPI class for every scenario.

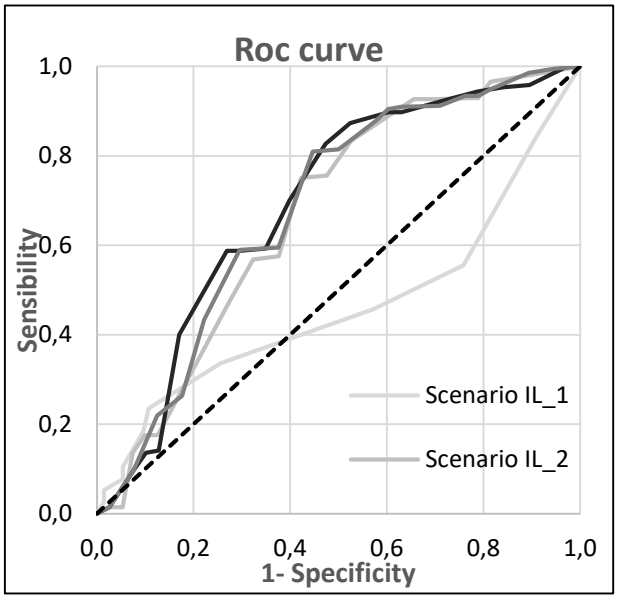

AUC	
Scenario IL_1	0.54
Scenario IL_2	0.67
Scenario IL_3	0.69
Scenario IL_4	0.68

Figure 30. ROC curve and AUC values values related to the LPI index.

As for the settlements, in Scenario 1, the distribution is balanced (Figure 31a), with a high frequency in the 0.05-0.10 m range (about 40%) and a good representation also in the 0.10-0.20 m range (around 30%). The extreme intervals, 0.0-0.05 m and 0.20-0.40 m, show a lower frequency. In Scenario 2 (Figure 31b), there is an increase in frequency for both the 0.10-0.20 m (about 50%) and 0.20-0.40 m (about 22%) ranges, at the expense of the lower classes. In Scenario 3(Figure 31c), the distribution shifts significantly towards higher settlement values. The dominant range is 0.20-0.40 m, which represents about 80% of occurrences, while other classes have much lower frequencies. Scenario 4 (Figure 31d) reflects a similar situation to Scenario 3, where almost all cases (about 90%) fall into the 0.20-0.40 m range.

As for the predictive performance analysis, the progression of the ROC curves and the AUC values shows a gradual improvement in the four scenarios: Settlement_1 (0.71), Settlement_2 (0.72), Settlement_3 (0.74), and Settlement_4 (0.74). This indicates that the model becomes more accurate in predicting critical cases as the data move toward more severe conditions. However, the last two scenarios (Settlement_3 and Settlement_4) show the same AUC value, confirming their similarity (Figure 32).

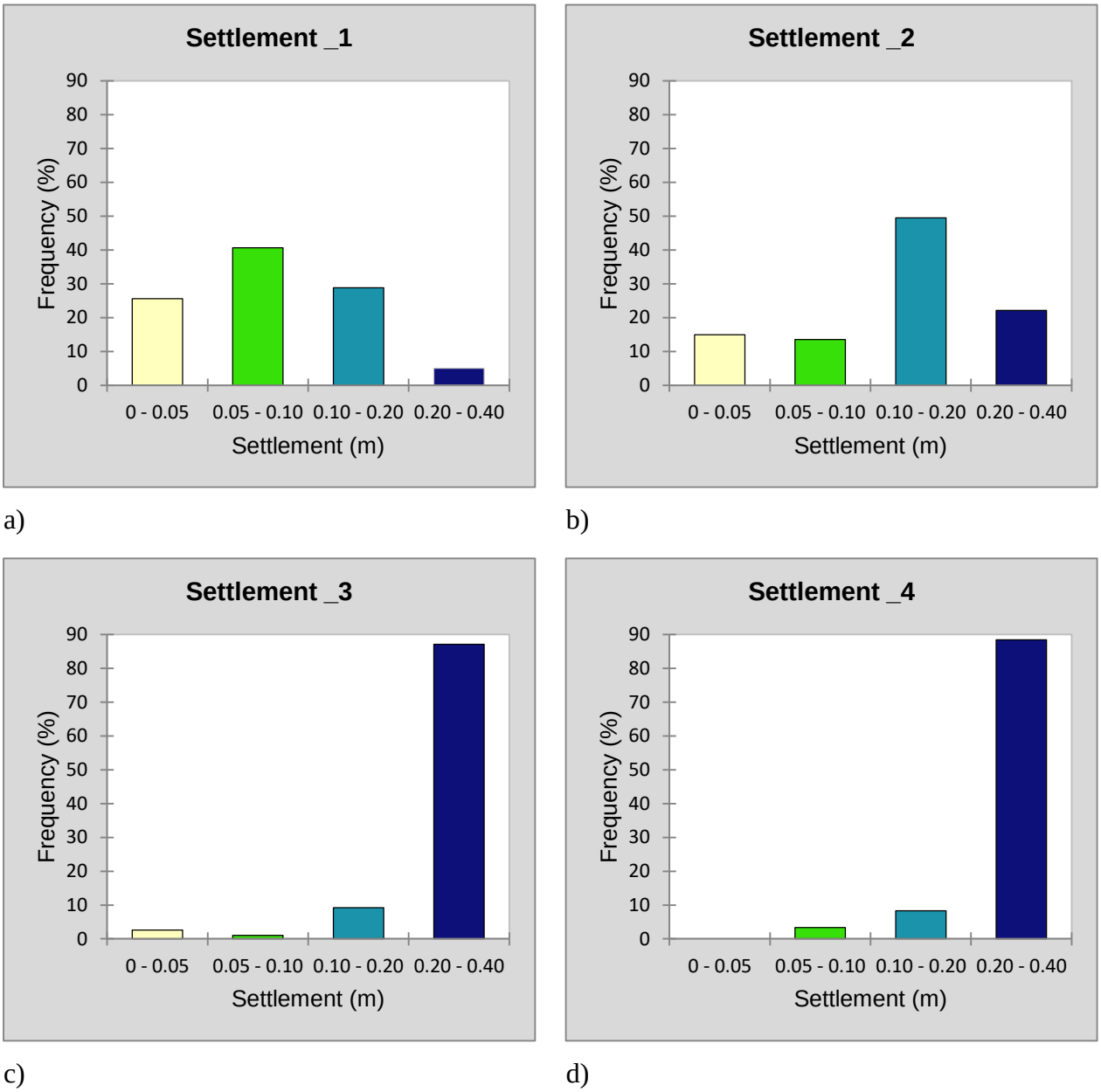

Figure 31. Frequency distribution of the liquefaction occurrences in every range of settlements for the 4 scenarios.

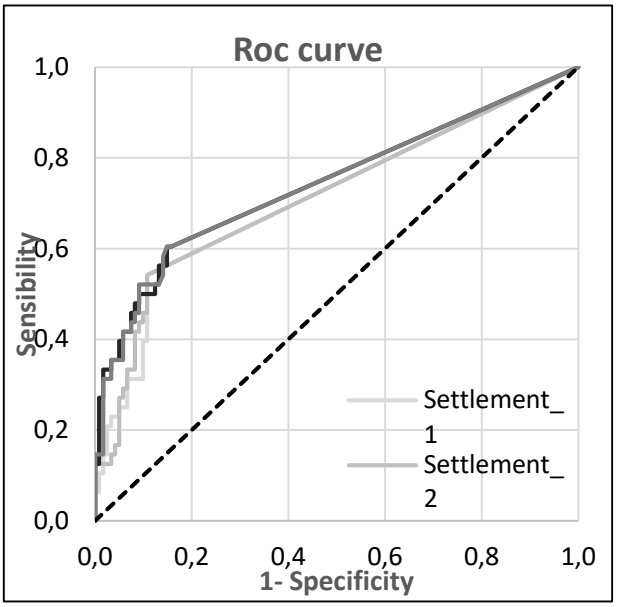

AUC	
Settlement_1	0.71
Settlement_2	0.72
Settlement_3	0.74
Settlement_4	0.74

Figure 32. ROC curve and AUC values for settlements.

3.5 References

Ambraseys, N.N., 1988. Engineering seismology: Part II. Earthquake Engineering & Structural Dynamics, 17, 51-105.

Anderson, D., Franke, K.W., Dashti, S., Badanagki, M., Kayen, R., 2019. The over-prediction of liquefaction in alluvially deposited volcanic sediments, Earthquake Geotechnical Engineering for Protection and Development of Environment and Constructions. CRC Press, pp. 1122-1129.

Anderson, K., Nelson, S., Mayo, A., Tingey, D., 2006. Interbasin flow revisited: The contribution of local recharge to high-discharge springs, Death Valley, CA. Journal of Hydrology, 323, 276-302.

Andrus, R.D., Stokoe, I.I.K.H., 2000. Liquefaction Resistance of Soils from Shear-Wave Velocity. Journal of Geotechnical and Geoenvironmental Engineering, 126, 1015-1025.

Andrus, R.D., Stokoe, K.H., II, 1999. Liquefaction Resistance Based on Shear Wave Velocity.

Boulanger, R.W., 2003. High Overburden Stress Effects in Liquefaction Analyses. Journal of Geotechnical and Geoenvironmental Engineering, 129, 1071-1082.

Boulanger, R.W., Idriss, I.M., 2014. CPT and SPT based liquefaction triggering procedures. Report No. UCD/CGM.-14, 1, 134.

Cetin, K.O. et al., 2000. Field case histories for SPT-based in situ liquefaction potential evaluation. Geotechnical engineering research report No. UCB/GT-2000/09.

Chiaradonna, A. et al., 2018. Numerical simulation of soil liquefaction during the 20 May 2012 M6. 1 Emilia Earthquake in Northern Italy: the case study of Pieve di Cento, pp. 18-21.

Civico, R. et al., 2015. Liquefaction susceptibility assessment in fluvial plains using airborne lidar: the case of the 2012 Emilia earthquake sequence area (Italy). Natural Hazards and Earth System Sciences, 15, 2473-2483.

Cubrinovski, M., Rhodes, A., Ntritsos, N., Van Ballegooy, S., 2019. System response of liquefiable deposits. Soil Dynamics and Earthquake Engineering, 124, 212-229.

Dobry, R., Taboada, V., Liu, L., 1997. Centrifuge modeling of liquefaction effects during earthquakes, International Conference on Earthquake Geotechnical Engineering (1 ; Tokyo 1995-11-14). A.A. Balkema, Rotterdam, pp. 1291-1324.

Flora, A., Bilotta, E., Lirer, S., Mele, L., Madoni, G., 2023. Liquefaction mechanisms and mitigation techniques. Rivista Italiana di Geotecnica, 2/2023, 33-88.

Hardin, B.O., Richart, F.E., 1963. Elastic Wave Velocities in Granular Soils. Journal of the Soil Mechanics and Foundations Division, 89, 33-65.

Hatanaka, M., Uchida, A., Ohara, J., 1997. Liquefaction characteristics of a gravelly fill liquefied during the 1995 Hyogo-Ken Nanbu earthquake. Soils and Foundations, 37, 107-115.

Idriss, I.M., Boulanger, R.W., 2006. Semi-empirical procedures for evaluating liquefaction potential during earthquakes. Soil dynamics and earthquake engineering, 26, 115-130.

Idriss, I.M., Boulanger, R.W., 2008. Soil liquefaction during earthquakes. Earthquake Engineering Research Institute. Oakland, CA.

Ishihara, K., Yoshimine, M., 1992. Evaluation of settlements in sand deposits following liquefaction during earthquakes. Soils and foundations, 32, 173-188.

Iwasaki, T., Arakawa, T., Tokida, K.-I., 1984. Simplified procedures for assessing soil liquefaction during earthquakes. International Journal of Soil Dynamics and Earthquake Engineering, 3, 49-58.

Iwasaki, T. et al., 1982. Microzonation for soil liquefaction potential using simplified methods, pp. 1310-1330.

Kayen, R.E. et al., 1992. Evaluation of SPT-, CPT-, and shear wave-based methods for liquefaction potential assessment using Loma Prieta data, pp. 177-204.

Kokusho, T., 1987. In-situ dynamic soil properties and their evaluations.

Kramer, S.L., Elgamal, A.W.M., 2001. Modeling soil liquefaction hazards for performance-based earthquake engineering, Pacific Earthquake Engineering Research Center, College of Engineering. University of California, Berkeley.

Kramer, S.L., Stewart, J.P., 2024. Geotechnical earthquake engineering. CRC Press.

Lai, C.G., Bozzoni, F., Mangriotis, M.-D., Martinelli, M., 2015. Soil liquefaction during the 20 may 2012 M5. 9 Emilia earthquake, northern Italy: Field reconnaissance and post-event assessment. Earthquake Spectra, 31, 2351-2373.

Lombardi, D., Bhattacharya, S., 2014. Liquefaction of soil in the Emilia-Romagna region after the 2012 Northern Italy earthquake sequence. Natural hazards, 73, 1749-1770.

Minarelli, L. et al., 2022. Liquefied sites of the 2012 Emilia earthquake: a comprehensive database of the geological and geotechnical features (Quaternary alluvial Po plain, Italy). Bulletin of Earthquake Engineering, 20, 3659-3697.

Moss, R.E.S. et al., 2003. Field case histories for CPT-based in situ liquefaction potential evaluation. Geoengineering Research Rep. UCB/GE-2003, 4.

NTC, 2008. Norme tecniche per le costruzioni. Decree of the Minister of the Infrastructures, 14.

NTC, 2018. Norme tecniche per le costruzioni. Decree of the Minister of the Infrastructures, 42.

Priolo, E. et al., 2012. The Ferrara thrust earthquakes of May-June 2012: preliminary site response analysis at the sites of the OGS temporary network. Annals of Geophysics, 55.

Pyke, R.M., 1979. Nonlinear Soil Models for Irregular Cyclic Loadings. Journal of the Geotechnical Engineering Division, 105, 715-726.

Robertson, P.K., Wride, C.E., 1998. Evaluating cyclic liquefaction potential using the cone penetration test. Canadian geotechnical journal, 35, 442-459.

Sciarra, A. et al., 2012. Soil-gas survey of liquefaction and collapsed caves during the Emilia seismic sequence. Annals of Geophysics.

Seed, H.B., Idris, I.M., 1982. Ground motions and soil liquefaction during earthquakes. Earthquake Engineering Institute Berkeley, CA.

Seed, H.B., Idriss, I.M., 1971. Simplified procedure for evaluating soil liquefaction potential. Journal of the Soil Mechanics and Foundations division, 97, 1249-1273.

Seed, H.B., Idriss, I.M., Arango, I., 1983. Evaluation of liquefaction potential using field performance data. Journal of geotechnical engineering, 109, 458-482.

Seed, H.B., Lee, K.L., 1966. Liquefaction of Saturated Sands During Cyclic Loading. Journal of the Soil Mechanics and Foundations Division, 92, 105-134.

Seed, H.B., Peacock, W.H., 1971. Test Procedures for Measuring Soil Liquefaction Characteristics. Journal of the Soil Mechanics and Foundations Division, 97, 1099-1119.

Seed, H.B., Tokimatsu, K., Harder, L.F., Chung, R.M., 1985. Influence of SPT procedures in soil liquefaction resistance evaluations. Journal of geotechnical engineering, 111, 1425-1445.

Shibata, T., Teparaksa, W., 1988. Evaluation of liquefaction potentials of soils using cone penetration tests. Soils and Foundations, 28, 49-60.

Silvestri, F., D'Onofrio, A., 2014. Risposta sismica e stabilità di centri abitati e infrastrutture, La Geotecnica nella difesa del territorio e delle infrastrutture dalle calamità naturali. AGI, pp. 5-60.

Sonmez, H., 2003. Modification of the liquefaction potential index and liquefaction susceptibility mapping for a liquefaction-prone area (Inegol, Turkey). Environmental Geology, 44, 862-871.

Stefani, M., Minarelli, L., Fontana, A., Hajdas, I., 2018. Regional deformation of late Quaternary fluvial sediments in the Apennines foreland basin (Emilia, Italy). International Journal of Earth Sciences, 107, 2433-2447.

Tokimatsu, K., Seed, H.B., 1987. Evaluation of settlements in sands due to earthquake shaking. Journal of geotechnical engineering, 113, 861-878.

Tokimatsu, K., Yamazaki, T., Yoshimi, Y., 1986. Soil Liquefaction Evaluations by Elastic Shear Moduli.

Soils and Foundations, 26, 25-35.

Tomasello, G., Porcino, D.D., 2022. Influence of sloping ground conditions on cyclic liquefaction behavior of sand under simple shear loading. Soil Dynamics and Earthquake Engineering, 163, 107516.

Tonkin, Taylor, 2012. Canterbury Earthquakes 2010 and 2011: Land Report as at 29 February 2012. . Earthquake, Commission.

Toprak, S., Holzer, T.L., 2003. Liquefaction potential index: field assessment. Journal of Geotechnical and Geoenvironmental Engineering, 129, 315-322.

Tsurumaki, S., Nishi, K., Kohmura, Y., Uchida, A., Babasaki, R., 2003. Study on the Simplified Procedure for Evaluating the Undrained Cycric Strength for Gravelly Soils (F572).

Vaid, Y.P., Stedman, J.D., Sivathayalan, S., 2001. Confining stress and static shear effects in cyclic liquefaction. Canadian Geotechnical Journal, 38, 580-591.

Vannucchi, G. et al., 2012. Soil liquefaction phenomena observed in recent seismic events in Emilia-Romagna Region, Italy. Ingegneria sismica, 2016, 20-30.

Youd, T.L., Idriss, I.M., 2001. Liquefaction resistance of soils: summary report from the 1996 NCEER and 1998 NCEER/NSF workshops on evaluation of liquefaction resistance of soils. Journal of geotechnical and geoenvironmental engineering, 127, 297-313.

Youd, T.L., Noble, S.K., 1997. Magnitude scaling factors. National Center for Earthquake Engineering, Research, Buffalo, NY, pp. 149-165.

Youd, T.L., Perkins, D.M., 1978. Mapping liquefaction-induced ground failure potential. Journal of the Geotechnical Engineering Division, 104, 433-446.

Zhang, G., Robertson, P.K., Brachman, R.W., 2002. Estimating liquefaction-induced ground settlements from CPT for level ground. Canadian Geotechnical Journal, 39, 1168-1180.

4 Regional Subsidence

4.1 Introduction

Subsidence has become a global issue, particularly in coastal areas (Herrera-García et al., 2021; Wu et al., 2022). Delta regions, which are representative of coastal areas, are home to over 300 million people (Edmonds et al., 2020) due to their fertile soil, perennial aquatic food sources, and convenient transportation and trade routes (Stanley and Warne, 1997). However, these regions are vulnerable to subsidence caused by various natural and anthropogenic factors. Natural factors include tectonics, soil compaction, and glacial isostatic adjustment, leading to long-term effects. Anthropogenic activities, such as urbanization and exploitation of underground resources, typically produce short-term effects and accelerate land subsidence (Higgins, 2015; Kuenzer et al., 2019; Syvitski et al., 2009). Subsidence in deltas can lead to relative sea level rise, shoreline erosion, and wetland loss, posing serious threats to coastal populations (Törnqvist et al., 2008).Interferometric synthetic aperture radar (InSAR) is an effective tool for high-precision, large-scale monitoring of surface deformation. It generates digital elevation models (DEM) by calculating the phase difference between SAR images taken at different times over the same area. Differential InSAR introduces external DEMs or uses data from multiple tracks to obtain surface deformation information (Gabriel et al., 1989; Massonnet et al., 1993). Multi-temporal InSAR (MT-InSAR) techniques mitigate atmospheric delay phase errors by leveraging atmospheric space low-pass and temporal high-pass properties, estimating deformation information from permanent scatterers. The measurement accuracy can reach centimeter or millimeter levels. The two classical MT-InSAR techniques are permanent scatterers (PS) (Ferretti et al., 2000, 2001) and small baseline subsets (SBAS) (Berardino et al., 2002). PS InSAR identifies PS points, such as buildings and exposed rocks, using a single image as the reference, and is suitable for monitoring linear deformation. SBAS InSAR can be extended to distributed scatterers (DS) points and is suitable for monitoring nonlinear deformation (Chen et al., 2021).

InSAR techniques have been successfully applied to estimate delta subsidence and characterize its spatial distribution in various regions, including the Nile Delta, Mekong Delta, Yellow River Delta, and Po Delta (Becker and Sultan, 2009; Erban et al., 2014; Higgins et al., 2013; Teatini et al., 2011). Unlike subsidence caused by human activities in inland cities, delta subsidence typically involves a rapid initial phase followed by gradual stabilization, primarily due to the natural consolidation of deposits. In the Po Delta, subsidence derived from ERS data follows a typical log-type consolidation process, consistent with the Terzaghi consolidation subsidence curve (Teatini et al., 2011). In other areas, subsidence of soft and nonhomogeneous clay deposits is often modeled using a hyperbolic rule (Park and Hong, 2021; Tan et al., 1991).

In recent years, the availability of SAR data and improvements in computational capabilities have advanced the analysis of subsidence. Initially, subsidence was primarily analyzed directly from InSAR

time series, with further investigation of triggering factors in specific areas or points. However, with the increased data availability from sources like Sentinel-1 and significant computational advancements, the deformation patterns in various areas and situations have become clearer. Consequently, research has increasingly focused on time series modeling to investigate spatiotemporal patterns, using algorithms for classification, clustering, and detection.

Seasonal and trend decomposition using LOESS and variational modal decomposition have been combined to estimate the periodic and trend components of InSAR time series and the thermal expansion characteristics of bridges (Bai et al., 2022). Similarly, InSAR time series are decomposed into trend and seasonality using least squares linear regression and the Fast Fourier Transform (FFT) (Priestley, 1981), followed by unsupervised detection of the time series (Festa et al., 2023). For turning/change points detection, a sequential turning point detection method for InSAR time series has been proposed (Ghaderpour et al., 2024). Additionally, a deep learning approach combining long short-term memory (LSTM) and time-gated LSTM has been developed for change point detection (Lattari et al., 2022). For InSAR time series classification, combining a stacked autoencoder (SAE) with a convolutional neural network (CNN) enables classification into five categories: stable, linear, accelerating, decelerating, and phase unwrapping error (Li et al., 2023).

In current research, seasonality is often analyzed in contexts such as the seasonal deformation of permafrost due to freezing and thawing (Jung et al., 2023) or the seasonal deformation of landslides correlated with precipitation (Hu et al., 2016). However, some seasonal signals not related to actual land surface deformation can mislead interpretation. Abrupt changes are also crucial for hazard assessment, especially in areas like the Po Delta, where significant portions of land are below sea level and protected by embankments. In the spatial domain, delta subsidence often exhibits a seaward distribution due to compressible deposits, potentially obscuring anomalous subsidence and complicating risk identification. Therefore, it is essential to provide a comprehensive spatiotemporal analysis of subsidence in areas such as the Po Delta.

Efforts in using InSAR for monitoring land subsidence have been significant, but systematic analysis of its time series is still in its early stages. With approximately 10 years of cumulative Sentinel-1 data, developing a framework for automatic monitoring of critical elements is particularly important. In this study, we present a spatiotemporal analysis based on InSAR time series, incorporating trend, seasonality, and abrupt change detection in the temporal domain, as well as numerical modeling in the spatial domain.

4.2 Tool chain for subsidence

In the context of subsidence, predisposing factors include topography, geological and geotechnical characteristics, land use/land cover (LULC), distance from tectonics, permeability, sea level and

geothermal activity (see Figure 33).

The subsidence tool chain assigns different levels of significance to each factor, indicated by a star rating: high (3 stars: topography, geology, geotechnical properties), medium (2 stars: LULC, distance from tectonics), low (1 star: permeability, sea level, geothermal activity). To the predisposing factors can be possibly added the preparatory factors which are water pumping, water table fluctuations and urbanisation. Trigger in cases of subsidence is water pumping. The effects of the post-trigger can be represented through process severity class maps that can be qualitative, quantitative (InSAR) and semi-quantitative (susceptibility).

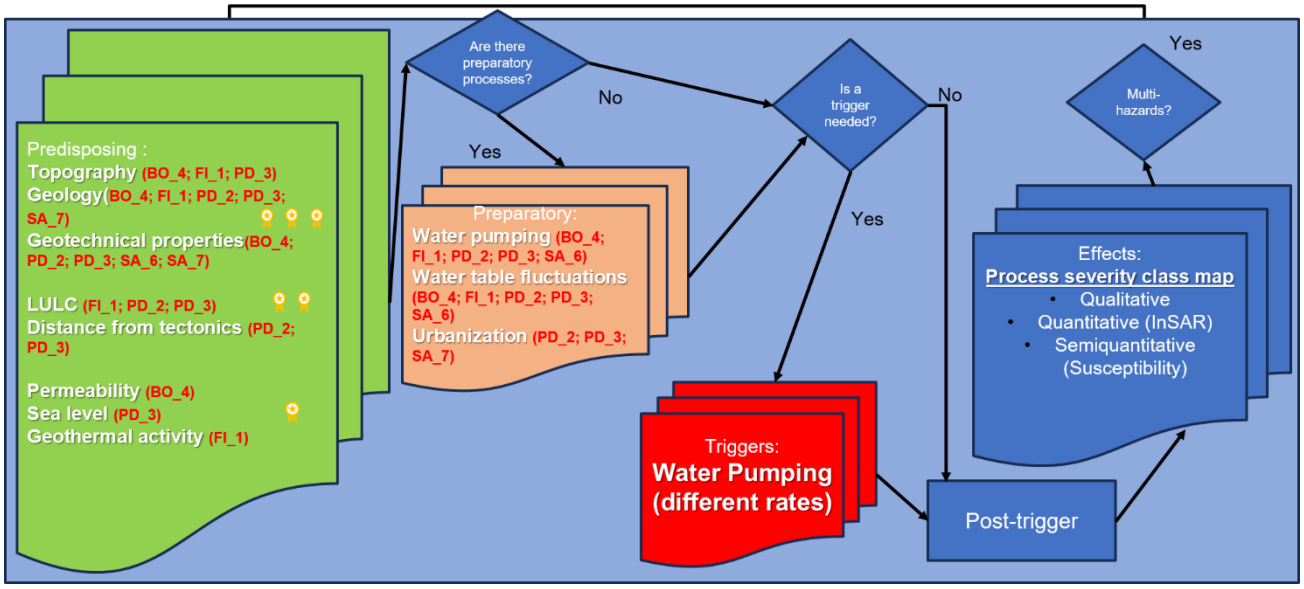

Figure 33. Tool chain developed under the RETURN project for subsidence analysis.

4.3 Methodology and Data

4.3.1 Data sources

The study utilized data from the European Ground Motion Service (EGMS) ortho product derived from Sentinel-1 between 2018 and 2022, capturing vertical and horizontal movements at 6-day intervals. Given that subsidence is the primary concern in the Po Delta area, only vertical movement data were analyzed. The EGMS dataset provides information on mean velocity, seasonal variations, time series displacement, among other parameters. Comparison of these velocities with our previous findings processed using the IPTA method in GAMMA software (Wegnüller et al., 2016), shows strong agreement (Fabris et al., 2022).

Figure 1b displays the vertical velocity sourced from EGMS data, indicating a seaward trend with velocities exceeding -10 mm/year nearer to the coast. Given the relatively short study period for this long-term subsidence process, the velocity trend typically exhibits a linear pattern. In Figure 1c, seasonality exhibits a varied spatial distribution. Most points show minimal seasonality, less than 2 mm, while only a few points record seasonality exceeding 4 mm.

4.3.2 Spatial modelling

To establish the relationship between the age of deposits and vertical velocities, four common functional models—power, exponential, logarithmic, and hyperbolic—were evaluated using the following formulas,

(1) power function: $y = a \cdot x^b + c$

(2) exponential model: $y = a \cdot e^{bx} + c \cdot e^{dx}$

(3) logarithmic model: $y = b \cdot ln\ ln\ (x + a)\ + c$

(4) hyperbolic function: $y = \frac{x}{a \cdot x + b} + c$

The age of deposits across the study area was obtained from geochronological data (Stefani and Vincenzi, 2005) and interpolated using a triangulated irregular network. The age values of deposits at specific points (PS points) were extracted from this network.

Considering the ongoing subsidence in the Po Delta area, which may include anomalies caused by anthropogenic factors (outliers), a robust least squares method is employed using bisquare weights (Huber and Ronchetti, 2011). The bisquare weights method minimizes a weighted sum of squares, where each data point's weight depends on its distance from the fitted line. Points close to the line receive full weight, while points further away receive reduced weight. Points that deviate significantly from the expected value may receive zero weight. This approach aims to fit a curve to the majority of the data using standard least squares while mitigating the influence of outliers.

The coefficient of determination R^2 and root mean square error (RMSE) of the four models are compared to determine the best-performing model. Subsequently, the chosen model is utilized to simulate subsidence based on the age of deposits. Following simulation, the disparity between observed and simulated subsidence is calculated. It is anticipated that there will be instances of anomalous subsidence in this analysis.

4.3.3 Temporal modelling: Modelling trend and seasonality

Given the potential movement characteristics within the delta, a regression model utilized in the EGMS data analysis is employed. This model comprises a third-order polynomial trend combined with a seasonal (sinusoidal) component. By applying this regression model to the InSAR time series data, the movement characteristics can be categorized into three main types: trend-dominant, seasonal-dominant, and irregular patterns. The parameter vector of the fitting model is as follows:

$$G = [t^3\ t^2\ t\ ones(n, 1)\ cos\ cos\ (2\pi \cdot t)\ \square\square\square\ sin\ (2\pi \cdot t)\ ]$$

where n represents the number of images and t is a column vector containing n acquisition dates.

After regression, if the standard deviation (STD) of the residuals is smaller than a specified

threshold σ and the amplitude of seasonality is smaller than another specified threshold σ_s, the data are classified as trend-dominant. If the STD of the residuals is smaller than the specified threshold σ but the amplitude of seasonality exceeds σ_s, the data are classified as seasonal-dominant. Any data that does not meet these criteria are classified as irregular patterns.

Since there are points showing noticeable seasonal variations, further investigation into seasonality includes examining its correlation with land surface temperature (LST). The Pearson correlation coefficient (C) between displacement and temperature time series is computed to assess the influence of temperature changes or other potential factors on displacement, using the following equation,

$$C = \frac{\sum_{i=1}^{n} (t_i - \underline{t})(w_i - \underline{w})}{\sqrt{\sum_{i=1}^{n} (t_i - \underline{t})^2}\sqrt{\sum_{i=1}^{n} (w_i - \underline{w})^2}}$$

where t_i, w_i represent land surface displacement and temperature, respectively, for the ith dates. The correlation coefficient C ranges from -1 to 1. A negative C indicates opposite seasonal patterns between the two parameters, while a positive C suggests similar seasonal patterns.

4.3.4 *Temporal modelling: Change detection*

In comparison to other remote sensing time series data, InSAR time series exhibit greater complexity and flexibility due to their spatiotemporal patterns being less rigidly tied to land use or geography. Given the uncertainty surrounding change points in such data, we adopted a method proposed by Zhao et al. (2019), tailored with our specific pattern definitions. This method, known as Bayesian Estimator of Abrupt Change, Seasonal Change, and Trend (BEAST), is designed for time-series decomposition, allowing for the extraction of nonlinear ecosystem dynamics across various timescales. BEAST employs Bayesian model averaging to assess the utility of individual decomposition models, thereby enhancing the robustness of detecting changepoints, seasonality, and trends in the data. It provides realistic nonlinear trend estimates and credible uncertainty measures, which are challenging to obtain using traditional single-best-model approaches.

In their evaluation, Li et al. (2022) assessed the effectiveness of three widely used methods: Detecting Breakpoints and Estimating Segments in Trend (DBEST) (Jamali et al., 2015), Breaks for Additive Seasonal and Trend (BFAST) (Verbesselt et al., 2010), and BEAST (Zhao et al., 2019). They determined that BEAST demonstrated superior performance in detecting abrupt changes in both trend and seasonality. Furthermore, BEAST was noted for its capability to effectively characterize the dynamics of abrupt changes in the data.

In our study, the seasonal components are modeled using a harmonic format with a seasonality order set to 1, indicating a single type of seasonal pattern. Given that seasonal variations are not relevant to subsidence, we disregard abrupt changes in the seasonal components, setting this parameter to 0. For the trend component, we assume the number of change points to range from 0 to 5. This choice reflects the InSAR time series data's 5-year period, allowing for at most 1 change point per year. The trend order

is set to 3, accommodating gradual curvilinear trends in the data. The algorithm provides probabilities associated with detected change points. We establish a probability threshold of 0.9, meaning that if the probability exceeds 0.9, the time series is considered to have experienced an abrupt change at that specific date. Regarding outliers, the algorithm permits a maximum of 50 outlier-type changepoints within the total dataset spanning 302 dates.

4.4 Application and validation to Po delta

4.4.1 Classification of PS points

According to our methodology, the PS points are categorized using the regression method. Points with low standard deviation (STD) and a small amplitude of seasonality exhibit displacements that align with a linear or curvilinear trend, classified as trend-dominated, as depicted in Figure 34a. Conversely, points with low STD but a large amplitude of seasonality display displacements following a clear seasonal pattern, classified as seasonal-dominated points, as shown in Figure 34b. The third category comprises points characterized by irregular patterns, resembling Figure 34c, lacking distinct trend or seasonal components but exhibiting noise.

In a subsequent analysis, to determine whether the trend tends towards linearity or curvature, a model comprising a first-order polynomial trend plus a seasonal (sinusoidal) component was employed. The standard deviation (STD) of the first-order polynomial model was compared with that of the third-order polynomial model, and their STD histograms are depicted in Figure 34d. It was observed that third-order polynomial models generally exhibit lower STD compared to linear models. This is reasonable because a linear trend can be seen as a special case of a first-order polynomial trend. For most points, the STD values from both models are similar, indicating these points follow a linear trend. However, in some cases, the STD from the third-order polynomial models is significantly lower, suggesting that these points are more likely to follow a curvilinear trend.

To visually distinguish between different classes of points, a threshold of STD for distinguishing regular and irregular points is set to 2. Additionally, a threshold of amplitude of seasonality between trend-dominated and seasonal-dominated points is set to 1. Using these thresholds, the classification of the PS points is illustrated in Figure 34e, with selected enlarged images. This figure clearly identifies points exhibiting linear displacements versus those showing seasonal displacements.

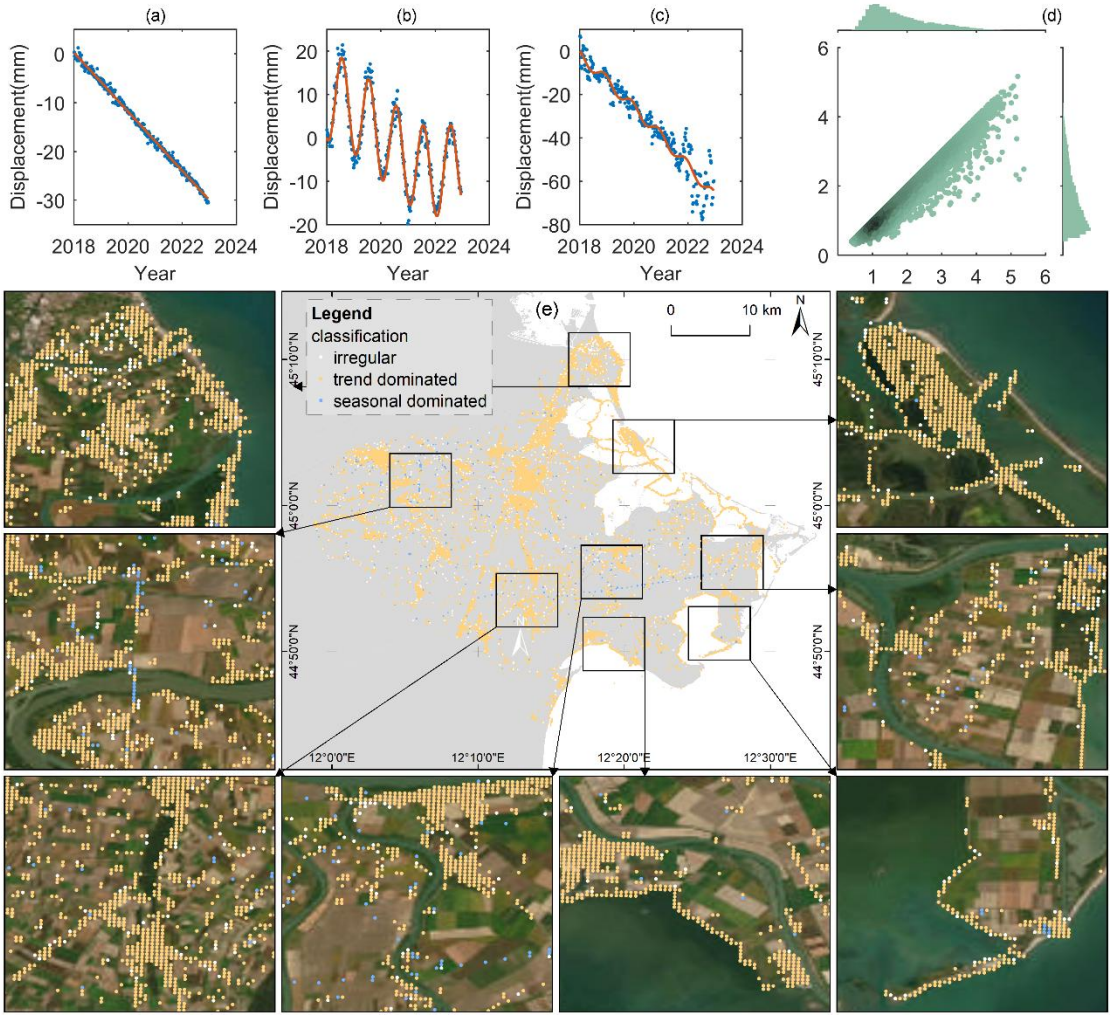

Figure 34 Classification of the points according to their temporal pattern.

4.4.2 Abrupt changes

Typical InSAR time series with and without abrupt changes are depicted in Figure 35a-d. The original time series exhibit clear abrupt changes, detectable using BEAST algorithms. When abrupt changes are evident, the probability of the change point approaches 1. The distribution of points with and without abrupt changes is illustrated in Figure 35e , with the majority showing no abrupt changes. Due to the Monte Carlo algorithm used in the calculations, results may vary. To enhance confidence in the results, calculations can be repeated multiple times.

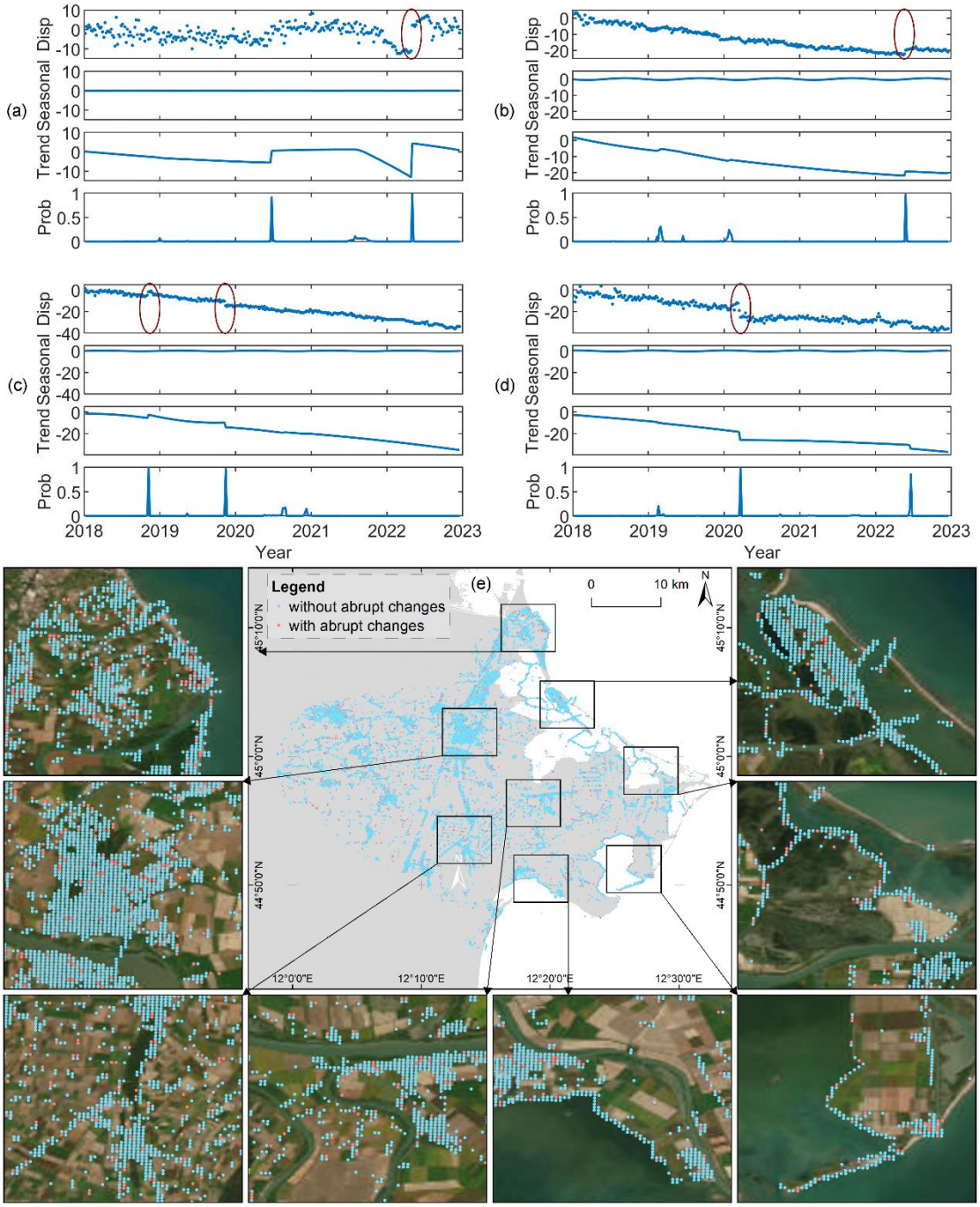

Figure 35. Spatial distribution of PS points without/with abrupt changes, with magnified images.

4.5 Spatial domain

The four models, including linear, polynomial (up to third order), power, exponential, and logarithmic models, were tested using robust estimation. Following the regression process, the fitted parameters along with their 95% confidence intervals are presented below, alongside the corresponding R2 and RMSE values.

(1) power function

$$y = 1.193 \cdot x^{0.1828} - 8.284$$

$R^2 = 0.7188, RMSE = 0.7987$

(2) exponential model:

$$y = -2.122 \cdot e^{-0.004936x} - 4.427 \cdot e^{-0.00009958x}$$

$R^2 = 0.71887$, $RMSE = 0.799$

(3) logarithmic model:

$$y = 0.6924 \cdot ln\ ln\ (x + 10.71)\ - 8.816$$

$R^2 = 0.7238$, $RMSE = 0.7916$

(4) hyperbolic function:

$$y = \frac{x}{0.2984 \cdot x + 82.36} - 6.568$$

$R^2 = 0.7201$, $RMSE = 0.7968$

The R2 and RMSE values of the four models are closely comparable, suggesting similar effectiveness in modeling. Figure 36 displays the four fitted lines against a backdrop of a scatter plot depicting the relationship between sediment ages (over the last 3500 years) and vertical velocities. Each fitted line exhibits a similar trend.

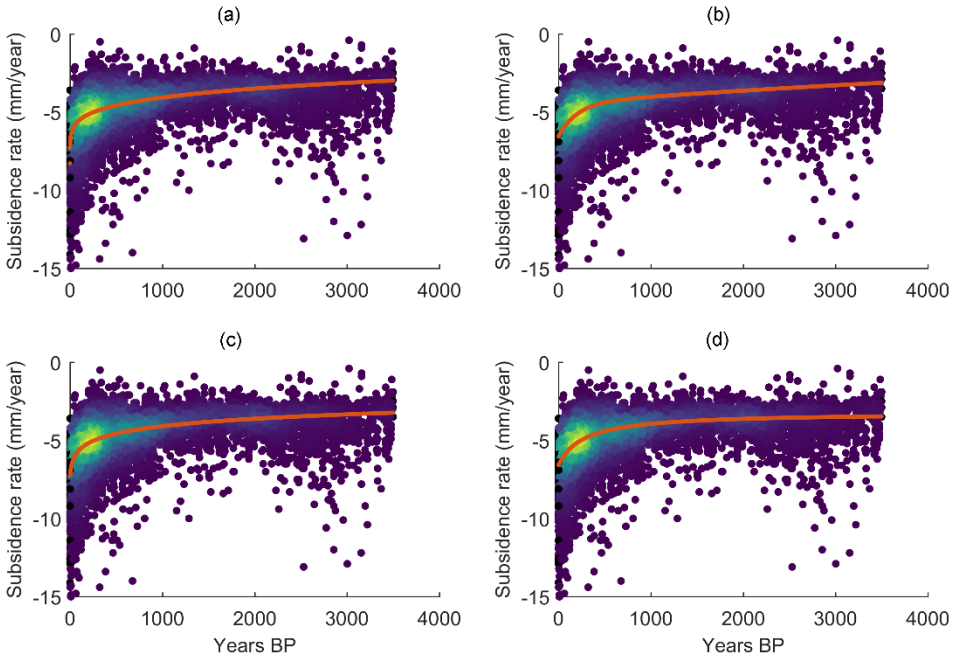

Figure 36. Geochronology data and the vertical velocity across all PS points within the area formed over the last 3500 years, modeled robustly using the logarithmic function.

Since there was little difference observed between the four models, and considering the logarithmic shape proposed by Teatini et al. (2011), the logarithmic model was selected for modeling natural subsidence in this study. Using the fitted parameters, the modeled subsidence distribution is depicted in Figure 37b. The observed subsidence distribution is shown in Figure 37a using the same colormap. The modeled subsidence distribution closely resembles the observed subsidence distribution. Figure 37 illustrates the difference between observed and modeled subsidence. For most points, the differences range from -2 to 2 mm/year, indicating good agreement between observed and modeled values. However, certain points show larger differences, as highlighted in Figure 37d-g: levees, a power plant, a breakwater, and a transmission tower exhibit significant differences. In Figure 37d-f, the differences are negative, indicating observed subsidence is greater than modeled. Conversely, in Figure 37g, the differences for the power tower line are positive, suggesting observed subsidence is less than modeled. Several factors could contribute to these discrepancies. Firstly, the lithology, shows predominant deposits of ancient coastal sands, delta fronts, and distributary channels. Secondly, construction of the tower likely required deeper foundations, potentially affecting the compressible deposits differently compared to surrounding areas.

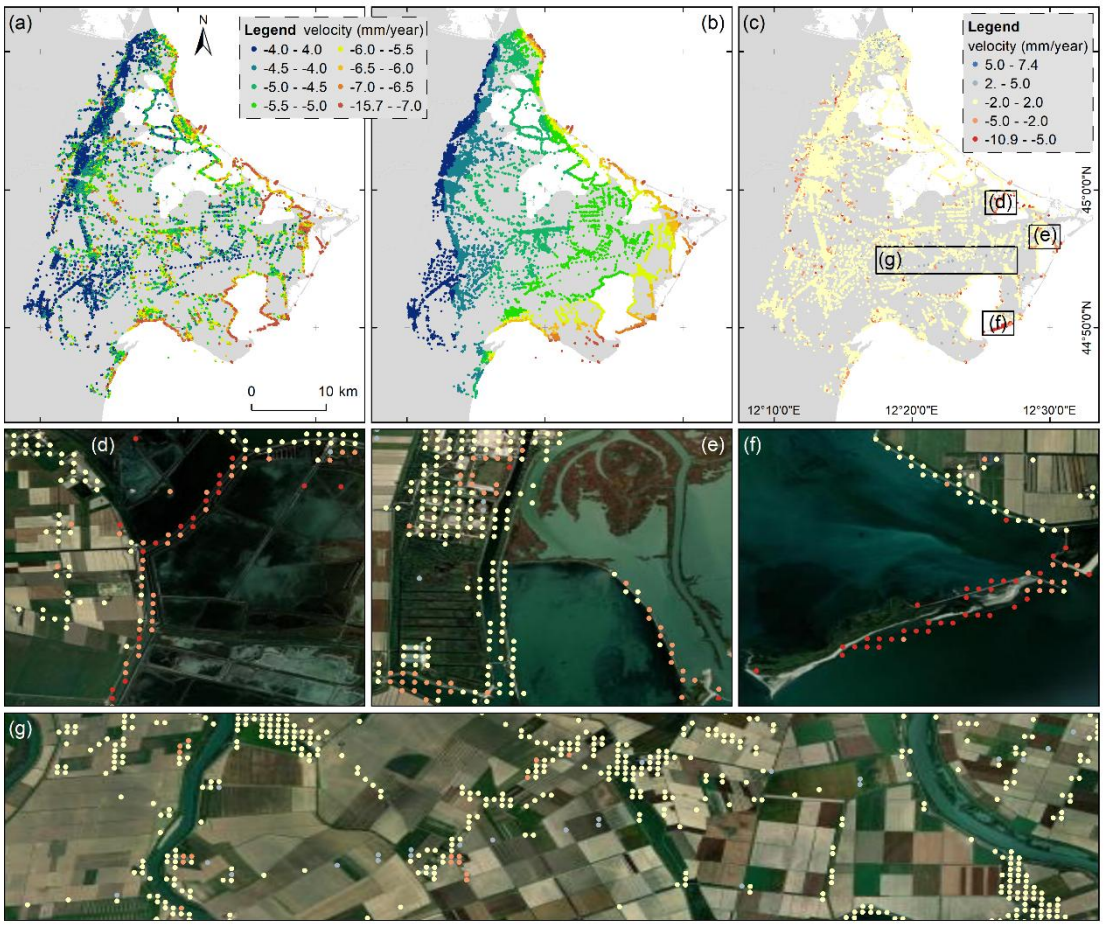

Figure 37. Vertical velocity comparison between observed and modeled data. (a) Observed vertical velocity. (b) Modeled vertical velocity derived using the logarithmic relationship with geochronology. (c) Difference between observed and modeled vertical velocities. (d-f) Magnified views of selected areas.

4.6 References

Bai, Z., Wang, Y., Fang, S., Liu, X., Gao, M., & Zhang, Z. 2022. Detecting seasonal and trend components in PS-InSAR displacement time series. Geocarto International, 37, 16212-16231. https://doi.org/10.1080/10106049.2022.2106316

Becker, R.H., & Sultan, M. 2009. Land subsidence in the Nile Delta: inferences from radar interferometry. The Holocene, 19, 949-954. https://doi.org/10.1177/0959683609336558

Berardino, P., Fornaro, G., Lanari, R., & Sansosti, E. 2002. A new algorithm for surface deformation monitoring based on small baseline differential SAR interferograms. IEEE Transactions on Geoscience and Remote Sensing, 40, 2375-2383. https://doi.org/10.1109/TGRS.2002.803792

Carbognin, L., Teatini, P., Tosi, L., Strozzi, T., & Tomasin, A. 2011. Present relative sea level rise in the northern Adriatic coastal area, 1147-1162.

Cenni, N., Fiaschi, S., & Fabris, M. 2021. Monitoring of Land Subsidence in the Po River Delta (Northern Italy) Using Geodetic Networks. Remote Sensing, 13, 1488. https://doi.org/10.3390/rs13081488

Chen, X., Peng, J., Song, Z., Zheng, Y., & Zhang, B. 2022. Monitoring Persistent Coal Fire Using Landsat Time Series Data from 1986 to 2020. IEEE Transactions on Geoscience and Remote Sensing, 60, 1-60. https://doi.org/10.1109/TGRS.2022.3142350

Chen, X., Tessari, G., Fabris, M., Achilli, V., & Floris, M. 2021. Comparison between PS and SBAS InSAR techniques in monitoring shallow landslides. Understanding and Reducing Landslide Disaster Risk (pp. 155-161)

Cleveland, R.B., Cleveland, W.S., McRae, J.E., & Terpenning, I. 1990. STL: A seasonal-trend decomposition. J. Off. Stat, 6, 3-73.

Edmonds, D.A., Caldwell, R.L., Brondizio, E.S., & Siani, S.M. 2020. Coastal flooding will disproportionately impact people on river deltas. Nature communications, 11, 1-8. https://doi.org/10.1038/s41467-020-18531-4

Erban, L.E., Gorelick, S.M., & Zebker, H.A. 2014. Groundwater extraction, land subsidence, and sea-level rise in the Mekong Delta, Vietnam. Environmental research letters, 9, 084010. https://doi.org/10.1088/1748-9326/9/8/084010

Fabris, M., Battaglia, M., Chen, X., Menin, A., Monego, M., & Floris, M. 2022. An Integrated InSAR and GNSS Approach to Monitor Land Subsidence in the Po River Delta (Italy). Remote Sensing, 14, 5578. https://doi.org/10.3390/rs14215578

Ferretti, A., Prati, C., & Rocca, F. 2000. Nonlinear subsidence rate estimation using permanent scatterers in differential SAR interferometry. IEEE Transactions on Geoscience and Remote Sensing, 38, 2202-2212. https://doi.org/10.1109/36.868878

Ferretti, A., Prati, C., & Rocca, F. 2001. Permanent scatterers in SAR interferometry. IEEE Transactions

on Geoscience and Remote Sensing, 39, 8-20. https://doi.org/10.1109/36.898661

Festa, D., Novellino, A., Hussain, E., Bateson, L., Casagli, N., Confuorto, P., Del Soldato, M., & Raspini, F. 2023. Unsupervised detection of InSAR time series patterns based on PCA and K-means clustering. International Journal of Applied Earth Observation and Geoinformation, 118, 103276. https://doi.org/10.1016/j.jag.2023.103276

Fiaschi, S., Fabris, M., Floris, M., & Achilli, V. 2018. Estimation of land subsidence in deltaic areas through differential SAR interferometry: the Po River Delta case study (Northeast Italy). International Journal of Remote Sensing, 39, 8724-8745. https://doi.org/10.1080/01431161.2018.1490977

Gabriel, A.K., Goldstein, R.M., & Zebker, H.A. 1989. Mapping small elevation changes over large areas: Differential radar interferometry. Journal of Geophysical Research: Solid Earth, 94, 9183-9191. https://doi.org/10.1029/JB094iB07p09183

Gambolati, G., Putti, M., Teatini, P., Camporese, M., Ferraris, S., Stori, G.G., Nicoletti, V., Silvestri, S., Rizzetto, F., & Tosi, L. 2005. Peat land oxidation enhances subsidence in the Venice watershed. Transactions American Geophysical Union, 86, 217-220. https://doi.org/10.1029/2005EO230001

Ghaderpour, E., Antonielli, B., Bozzano, F., Mugnozza, G.S., & Mazzanti, P. 2024. A fast and robust method for detecting trend turning points in InSAR displacement time series. Computers & Geosciences, 185, 105546. https://doi.org/10.1016/j.cageo.2024.105546

Giosan, L., Syvitski, J., Constantinescu, S., & Day, J. 2014. Climate change: Protect the world's deltas. Nature News, 516, 31. https://doi.org/10.1038/516031a

Herrera-García, G., Ezquerro, P., Tomás, R., Béjar-Pizarro, M., López-Vinielles, J., Rossi, M., Mateos, R.M., & al., e. 2021. Mapping the global threat of land subsidence. science, 371, 34-36. https://doi.org/10.1126/science.abb8549

Higgins, S., Overeem, I., Tanaka, A., & Syvitski, J.P. 2013. Land subsidence at aquaculture facilities in the Yellow River delta, China. Geophysical Research Letters, 40, 3898-3902. https://doi.org/10.1002/grl.50758

Higgins, S.A. 2015. Review: Advances in delta-subsidence research using satellite methods. Hydrogeology Journal, 24, 587-600. https://doi.org/10.1007/s10040-015-1330-6

Hu, X., Wang, T., Pierson, T.C., Lu, Z., Kim, J., & Cecere, T.H. 2016. Detecting seasonal landslide movement within the Cascade landslide complex (Washington) using time-series SAR imagery. Remote Sensing of Environment, 187, 49-61. https://doi.org/10.1016/j.rse.2016.10.006

Huber, P.J., & Ronchetti, E.M. 2011. Robust statistics. John Wiley & Sons.

Jamali, S., Jönsson, P., Eklundh, L., Ardö, J., & Seaquist, J. 2015. Detecting changes in vegetation trends using time series segmentation. Remote Sensing of Environment, 156, 182-195. https://doi.org/10.1016/j.rse.2014.09.010

Jung, Y.T., Park, S.-E., & Kim, H.-C. 2023. Observation of spatial and temporal patterns of seasonal

ground deformation in central Yakutia using time series InSAR data in the freezing season. Remote Sensing of Environment, 293, 113615. https://doi.org/10.1016/j.rse.2023.113615

Kuenzer, C., Heimhuber, V., Huth, J., & Dech, S. 2019. Remote sensing for the quantification of land surface dynamics in large river delta regions - A review. Remote Sensing, 11, 1985. https://doi.org/10.3390/rs11171985

Lattari, F., Rucci, A., & Matteucci, M. 2022. A deep learning approach for change points detection in InSAR time series. IEEE Transactions on Geoscience and Remote Sensing, 60, 1-16. https://doi.org/10.1109/TGRS.2022.3155969

Li, J., Li, Z.-L., Wu, H., & You, N. 2022. Trend, seasonality, and abrupt change detection method for land surface temperature time-series analysis: Evaluation and improvement. Remote Sensing of Environment, 280, 113222. https://doi.org/10.1016/j.rse.2022.113222

Li, M., Wu, H., Yang, M., Huang, C., & Tang, B.-H. 2023. Trend Classification of InSAR Displacement Time Series Using SAE–CNN. Remote Sensing, 16, 54. https://doi.org/10.3390/rs16010054

Maselli, V., & Trincardi, F. 2013. Man made deltas. Scientific reports, 3, 1-7. https://doi.org/10.1038/srep01926

Massonnet, D., Rossi, M., Carmona, C., Adragna, F., Peltzer, G., Feigl, K., & Rabaute, T. 1993. The displacement field of the Landers earthquake mapped by radar interferometry. Nature, 364, 138-142. https://doi.org/10.1038/364138a0

Park, S.W., & Hong, S.H. 2021. Nonlinear modeling of subsidence from a decade of InSAR time series. Geophysical Research Letters, 48, e2020GL090970. https://doi.org/10.1029/2020GL090970

Peng, F., & Qihao, W. 2015. Temporal Dynamics of Land Surface Temperature From Landsat TIR Time Series Images. IEEE Geoscience and Remote Sensing Letters, 12, 2175-2179. https://doi.org/10.1109/lgrs.2015.2455019

Priestley, M.B. 1981. Spectral analysis and time series. Academic press London. https://doi.org/9780125649223

Salvioni, G. 1957. I movimenti del suolo nell'Italia centro-settentrionale, 16, 325-366.

Sestini, G. 1996. Land subsidence and sea-level rise: the case of the Po Delta region, Italy. Sea-level rise and coastal subsidence (pp. 235-248): Springer. https://doi.org/10.1007/978-94-015-8719-8_13

Simeoni, U., & Corbau, C. 2009. A review of the Delta Po evolution (Italy) related to climatic changes and human impacts. Geomorphology, 107, 64-71. https://doi.org/10.1016/j.geomorph.2008.11.004

Stanley, D.J., & Warne, A.G. 1997. Holocene Sea-Level Change and Early Human Utilization of Deltas. GSAToday, 7, 1-7.

Stefani, M., & Vincenzi, S. 2005. The interplay of eustasy, climate and human activity in the late Quaternary depositional evolution and sedimentary architecture of the Po Delta system. Marine Geology, 222, 19-48. https://doi.org/10.1016/j.margeo.2005.06.029

Syvitski, J., Kettner, A., Overeem, I., Hutton, E., Hannon, M., Brakenridge, G., Day, J., Vörösmarty, C., Saito, Y., Giosan, L., & Nicholls, R. 2009. Sinking deltas due to human activities. Nature Geoscience, 2, 681-686. https://doi.org/10.1038/ngeo629

Tan, T.-S., Inoue, T., & Lee, S.-L. 1991. Hyperbolic method for consolidation analysis. Journal of Geotechnical Engineering, 117, 1723-1737. https://doi.org/10.1061/(ASCE)0733-9410(1991)117:11(1723)

Teatini, P., Gambolati, G., & Tosi, L. 1995. A new three-dimensional nonlinear model of the subsidence at Venice. Land subsidence. Proc. international symposium, the Hague, 1995, 353-361. https://doi.org/10.1016/0148-9062(96)83375-4

Teatini, P., Tosi, L., & Strozzi, T. 2011. Quantitative evidence that compaction of Holocene sediments drives the present land subsidence of the Po Delta, Italy. Journal of Geophysical Research, 116, B08407. https://doi.org/10.1029/2010jb008122

Törnqvist, T.E., Wallace, D.J., Storms, J.E., Wallinga, J., Van Dam, R.L., Blaauw, M., Derksen, M.S., Klerks, C.J., Meijneken, C., & Snijders, E.M. 2008. Mississippi Delta subsidence primarily caused by compaction of Holocene strata. Nature Geoscience, 1, 173-176. https://doi.org/10.1038/ngeo129

Tosi, L., Da Lio, C., Strozzi, T., & Teatini, P. 2016. Combining L-and X-band SAR interferometry to assess ground displacements in heterogeneous coastal environments: the Po River Delta and Venice Lagoon, Italy. Remote Sensing, 8, 308. https://doi.org/10.3390/rs8040308

Tosi, L., Teatini, P., & Strozzi, T. 2013. Natural versus anthropogenic subsidence of Venice. Scientific reports, 3, 1-9. https://doi.org/10.1038/srep02710

Verbesselt, J., Hyndman, R., Newnham, G., & Culvenor, D. 2010. Detecting trend and seasonal changes in satellite image time series. Remote Sensing of Environment, 114, 106-115. https://doi.org/10.1016/j.rse.2009.08.014

Vitagliano, E., Riccardi, U., Piegari, E., Boy, J.-P., & Di Maio, R. 2020. Multi-component and multi-source approach for studying land subsidence in deltas. Remote Sensing, 12, 1465. https://doi.org/10.3390/rs12091465

Vitagliano, E., Vitale, E., Russo, G., Piccinini, L., Fabris, M., Calcaterra, D., & Di Maio, R. 2022. Analysis of the Periodic Component of Vertical Land Motion in the Po Delta (Northern Italy) by GNSS and Hydrological Data. Remote Sensing, 14, 1126. https://doi.org/10.3390/rs14051126

Wegnüller, U., Werner, C., Strozzi, T., Wiesmann, A., Frey, O., & Santoro, M. 2016. Sentinel-1 Support in the GAMMA Software. Procedia Computer Science, 100, 1305-1312. https://doi.org/10.1016/j.procs.2016.09.246

Wu, P.C., Wei, M., & D'Hondt, S. 2022. Subsidence in coastal cities throughout the world observed by InSAR. Geophysical Research Letters, 49, e2022GL098477. https://doi.org/10.1029/2022GL098477

Zhao, K., Wulder, M.A., Hu, T., Bright, R., Wu, Q., Qin, H., Li, Y., Toman, E., Mallick, B., Zhang, X., & Brown, M. 2019. Detecting change-point, trend, and seasonality in satellite time series data to track abrupt changes and nonlinear dynamics: A Bayesian ensemble algorithm. Remote Sensing of Environment, 232, 111181. https://doi.org/10.1016/j.rse.2019.04.034

5 Anthropogenic Sinkholes

Sinkholes are characterized by an enclosed depression, regardless of the presence of an internal drainage (Waltham and Fookes, 2003), with a predominantly subcircular shape in plan view and a varying three-dimensional shape (cylindrical, conical, etc.). (Gutiérrez, 2016). The process that generates sinkholes can usually be described in the following steps (Waltham et al., 2005): firstly, surface or meteoric water enters an enclosed depression, and it infiltrates underground. This first step can also be accompanied by possible local ground erosion due to water that washes away the surface material. Subsequently, the infiltrated water can cause the dissolution of soluble rock underground, typically karst-related materials or evaporitic rocks. This dissolution can form underground cavities that can eventually collapse and form a sinkhole.

The described process can also impact man made underground cavities, and, in this case, sinkholes triggered due to the heavy anthropization are called “anthropogenic sinkholes” (Guarino and Nisio, 2012; Parise, 2015). Man made cavities are extremely widespread all over the world, and even in Italian cities like Rome (Fasani et al., 2013), Catania (Bonaccorso et al. 2005), Naples (Varriale et al., 2022) (Figure 38), and Palermo (Todaro, 2020).

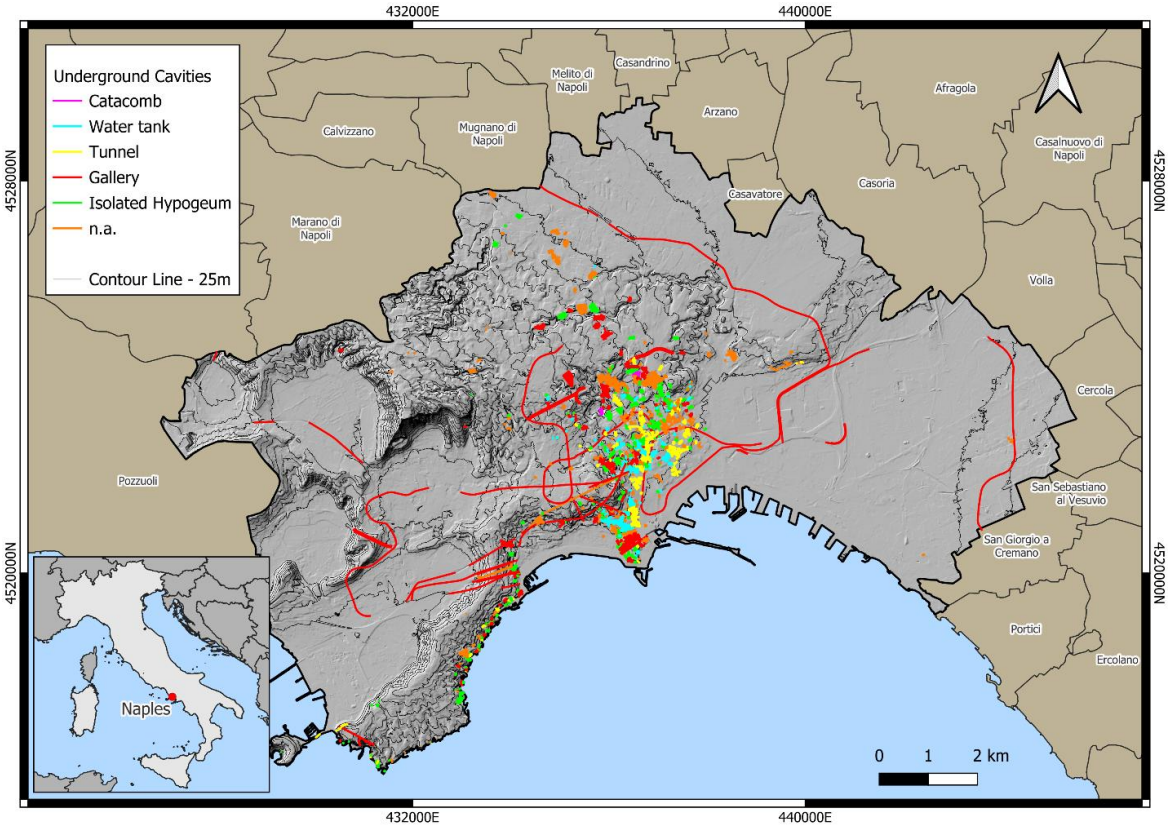

Figure 38. Example of a dense underground cavity network in an Italian city (Naples). In the inlet, the location of the city of Naples in the Italian peninsula.

These voids can be either directly or indirectly related to human activities. Mining building stones

is one of the primary examples of manmade cavities directly excavated by humans that can be affected by anthropogenic sinkholes (Singh and Dhar, 1997). In January 1996, during the construction of an underground tunnel aimed at road network expansion, a sinkhole triggered and damaged a gas pipeline; the subsequent explosion caused by the sinkhole killed 11 people and heavily damaged a residential building (Puntillo, 2001). Sinkholes caused by leaking faulty or damaged pipes can be the cause of unexpected underground cavities (Dastpak et al., 2023) and be a danger to human life: in September 1969, in Via Aniello Falcone, a teacher died after an underground cavity caused by a damaged water collector collapsed (Puntillo, 2001).

The methodology proposed in this deliverable as a tool for the anthropogenic sinkhole susceptibility analysis is aimed at the objectives of WP4 and, in particular, Task 2.4.3. It is based on a statistical approach, in particular to the construction of an ensemble model, using three different machine learning algorithms: Gradient Boosting Machine (hereafter GBM) (Friedman, 2001); Random Forest (RF) (Breiman, 2001); and Maximum Entropy (MaxEnt) (Phillips and Dudìk, 2008). Subsequently, the Temporal Occurrence is evaluated using the Poisson distribution (Poisson, 1837; Haight, 1967) for 4, user-defined, time intervals. Lastly, twelve hazard scenarios (three Spatial Occurrence maps × four Temporal Occurrence probabilities) (Figure 39) are obtained. The tool requires, before starting the processing, to compile the CONFIG.txt file. The user can define different settings by modifying the file (the specific settings will be shown later) with the first one being the choice between:

- Sinkhole Susceptibility Assessment;

- Sinkhole Hazard Scenario Evaluation.

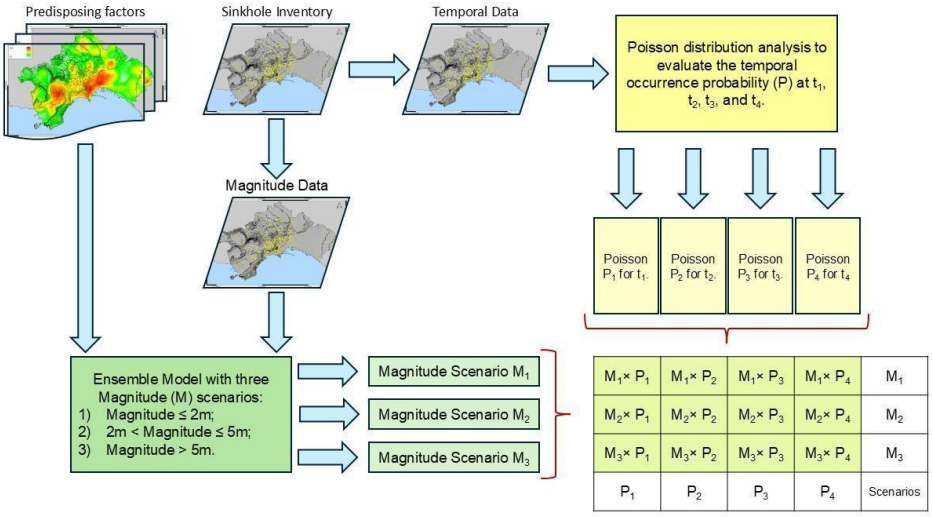

Figure 39. Example of Hazard Scenarios evaluation using the produced tool.

Figure 39

5.1 Tool chain for subsidence

In the context of subsidence, predisposing factors include geological and geotechnical

characteristics, structural elements, past events, distance from infrastructures, man-made caves, LULC and topograph (see Figure 40), with different levels of significance: high (3 stars: topography, geology, geotechnical properties), medium (2 stars: LULC, distance from tectonics), low (1 star: permeability, sea level, geothermal activity). To the predisposing factors can be possibly added the preparatory factors which are heavy rainfall events and water table fluctuations. Trigger in cases of sinkholes is the occurrence of important rainfall events. The effects of the post-trigger can be represented through process severity class maps that can be qualitative, quantitative (InSAR) and semi-quantitative (susceptibility).

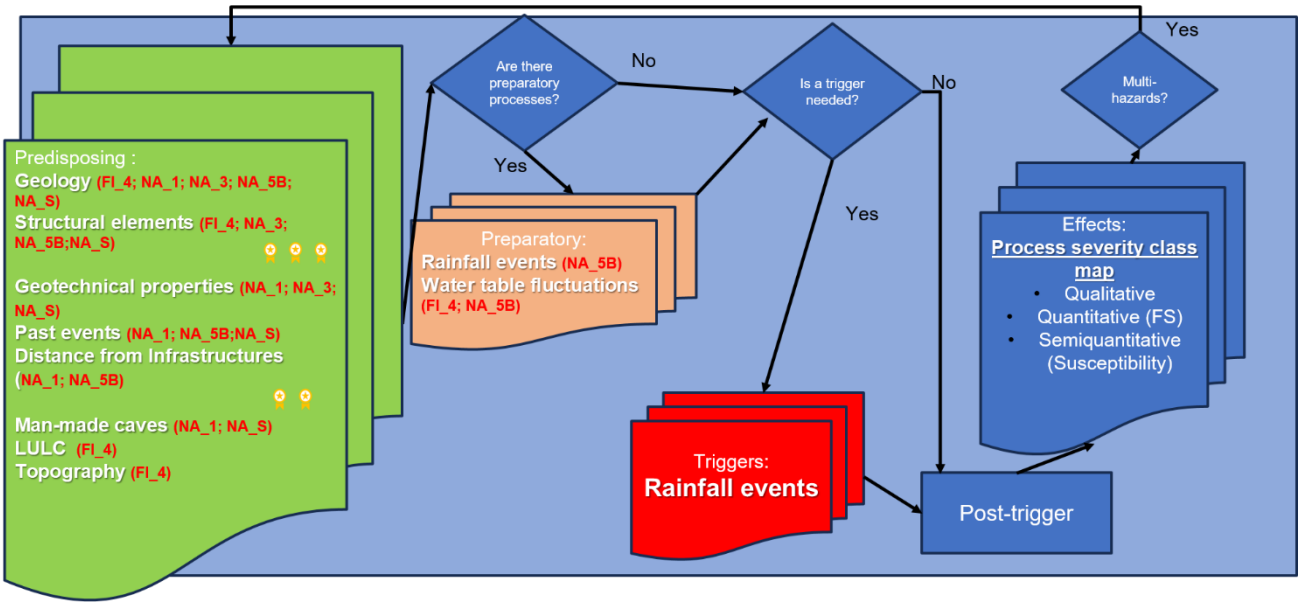

Figure 40. Tool chain developed under the RETURN project for sinkholes analysis.

5.2 Anthropogenic Sinkhole Inventory: Data gathering for statistical analysis

The Anthropogenic Sinkhole inventory (Figure 41) is an essential tool for sinkhole susceptibility assessment (Tufano et al., 2022). As the proposed approach is based on statistical methods like machine learning algorithms, an anthropogenic sinkhole inventory containing updated and complete information is a vital tool. In particular, this approach uses the exact dates data to perform Poisson distribution and sinkhole diameter to evaluate the magnitude of the event. The reason the diameter has been chosen as the magnitude index instead of the depth is mostly related to both data availability (the diameter is a characteristic measurable from the surface level) and the impact on the urban fabric, as sinkholes of different sizes can lead to different degrees of road or building interdiction.

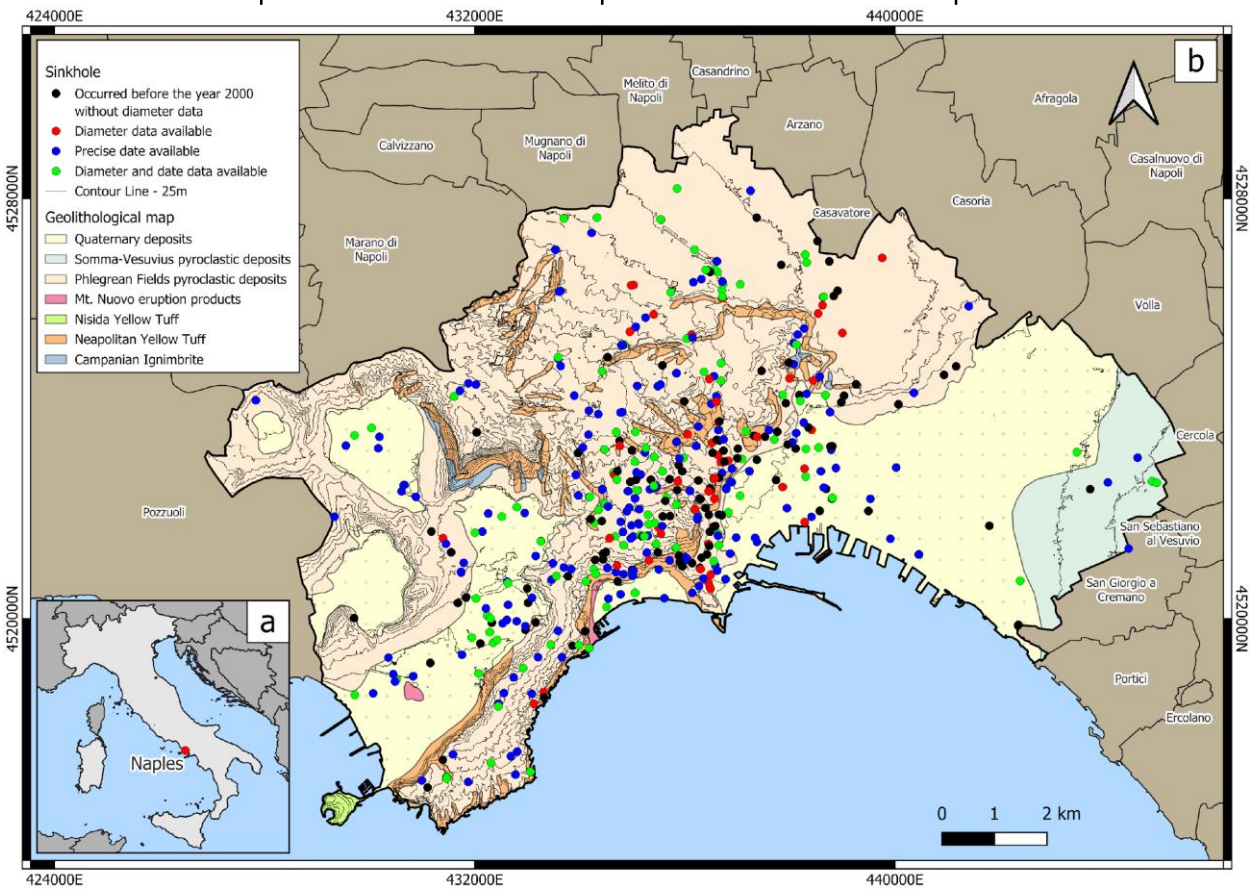

Figure 41. Anthropogenic Sinkhole Inventory of the city of Naples. This South Italian city and the city of Palermo have been largely used as test areas for the proposed approach.

The proposed approach, which uses the sinkhole inventory as the presence data for the statistical analysis, requires different .csv files depending on the type of analysis required by the user. As mentioned before, the tool can execute two different methods, the first one (a) for a simple susceptibility analysis and the second one (b) for the Sinkhole Hazard scenarios.

The inventory/presence data required for the first method needs to be formatted as a .csv file containing the following three columns:

- First column containing ID or species data (will not be used during the process phase);

- Longitude – the coordinate system is irrelevant; it only needs to be the same one as the predisposing factor raster files;

- Latitude – just like the Longitude column, the EPSG needs to be the same one as the longitude and the predisposing factors raster ones.

Regarding the second approach, the required inventory file increases to two .csv, as the temporal and spatial analysis are performed separately.

The .csv file containing the data for the susceptibility analysis also contains the sinkhole diameters

and is made up of four columns (Figure 42):

- ID or species data column;

- Longitude;

- Latitude;

- Diameter – containing the data related to the maximum diameter of the sinkhole.

	A	B
1	species,lon,lat,D (m)	
2	Sinkhole,434265.16,4520946.05,2.50	
3	Sinkhole,436689.25,4524535.26,1.00	
4	Sinkhole,435837.49,4521359.22,1.80	
5	Sinkhole,434674.94,4521567.93,0.50	
6	Sinkhole,438304.14,4522707.23,0.50	
7	Sinkhole,437094.79,4523039.76,10.00	
8	Sinkhole,435046.46,4522990.98,3.00	
9	Sinkhole,437055.33,4522342.05,11.00	
10	Sinkhole,435419.92,4523079.38,1.50	

Figure 42. Example of Hazard Scenarios evaluation using the produced tool.

As for the second .csv file, the one related to the temporal analysis (Figure 43), it is also made up of four columns:

- ID or species data column;

- Longitude;

- Latitude;

- Date – with format data YYYY-MM-DD.

	A	B
1	species,lon,lat,Date	
2	Sinkhole,433926.69,4522740.22,2009-06-21	
3	Sinkhole,435243.68,4523170.89,2009-06-21	
4	Sinkhole,436583.37,4521012.88,2009-11-03	
5	Sinkhole,434265.16,4520946.05,2009-12-02	
6	Sinkhole,436689.25,4524535.26,2009-12-18	
7	Sinkhole,435837.49,4521359.22,2013-10-08	
8	Sinkhole,436793.55,4522498.07,2013-11-30	
9	Sinkhole,434674.94,4521567.93,2013-03-08	
10	Sinkhole,438304.14,4522707.23,2013-11-25	

Figure 43. Example of a .csv file containing the precise dates of occurrence.

As shown previously in Figure 41, not all the entries of the sinkhole inventory contain complete information about the event. There could be a sinkhole with complete geometrical information but no precise date of occurrence, or there could be an event well known from a temporal point of view but

without additional information. For this reason, to avoid any possible confusion and make the data formatting phase easier, it was decided to utilize two different .csv inventory files in the second type of approach.

5.3 Anthropogenic Sinkhole spatial Occurrence Analysis

The tool for the Anthropogenic Sinkhole Spatial Occurrence analysis has been written in R (R Core Team, 2024) using the R Studio software (Posit Team, 2025). Other packages used are:

- biomod2 (Thuiller et al., 2023);
- caret (Kuhn, 2008);
- classInt (Bivand, 2025);
- dismo (Hijmans et al., 2024);
- doparallel (Corporation and Weston, 2022);
- dplyr (Wickham et al., 2023);
- earth (Milborrow et al., 2024);
- gam (Hastie, 2024);
- ggplot2 (Wickham, 2016);
- ggtext (Wilke and Wiernik, 2022);
- glmnet (Tay et al., 2023);
- leaflet (Cheng et al., 2024);
- maxnet (Phillips, 2021);
- mda (Hastie and Tibshirani, 2024);
- modEvA (Barbosa et al., 2013);
- parallel (R Core Team, 2024);
- raster (Hijmans, 2025a);
- randomForest (Liaw and Wiener, 2002);
- RcppEigen (Bates and Eddelbuettel, 2013);
- sf (Pebesma, 2018; Pebesma and Bivand, 2023);
- spatstat (Baddeley et al., 2015);
- terra (Hijmans, 2025b);

- tidyterra (Hernangómez, 2023);
- usdm (Naimi et al., 2014);
- writexl (Ooms, 2024);
- xgboost (Chen et al., 2024).

Of these packages: biomod2; caret, dismo, doparallel, dplyr, earth, gam, glmnet, maxnet, mda, parallel, randomForest, RcppEigen, sf, spatstat, usdm, and xgboost were used for analysis; classInt to divide the susceptibility maps into classes using the Natural Breaks method (Jenks, 1967); ggplot2, ggtext, leaflet, tidyterra were used for diagram and map building; raster and terra were used to perform analysis on the raster data; writexl was employed to manage .xlsx files; finally, the modEvA package was used for the final performance evaluation.

The script requires the intervention of the user to set up the analysis. Before starting the analysis, opening the CONFIG.txt is required (Figure 44).

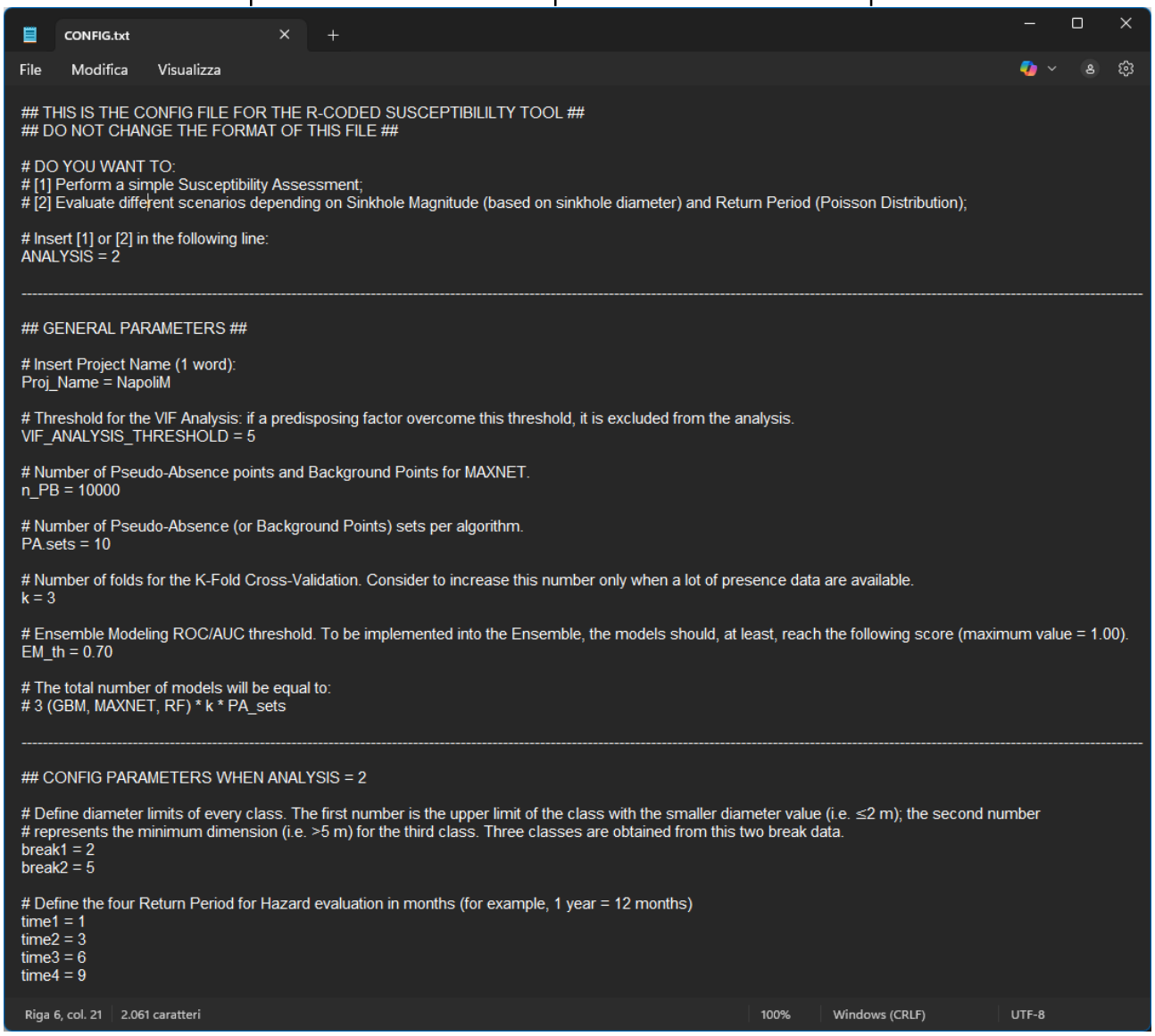

Figure 44. The CONFIG.txt file.

In the first section, at the “ANALYSIS” entries, the user can decide which type of analysis to perform, using either 1 for a sinkhole susceptibility analysis or 2 for the sinkhole hazard scenarios.

In the following section, the user can select the name of the project in “Proj_Name”, while the threshold is used for the Variance Inflation Factor (hereafter VIF). This is a useful tool used to find out if there are collinearity problems, as statistical methods tend to not be able to distinguish when two predictor variables are closely related to each other, leading to collinearity problems. James et al. (2021) define collinearity as "*...the situation in which two or more predictor variables are closely related to one another*". These two parameters tend to have a similar impacts on the model, making it difficult to evaluate the impact of a single predisposing factor. The VIF formula is calculated as (modified from James et al., 2021):

$$VIF_j = \frac{1}{1 - R^2_{\frac{x_j}{x_{-j}}}}$$

In this formula, $R^2_{xj/x-j}$ is the R^2 value of the regression between the predisposing factor j against other factors. It is, in other words, a coefficient that defines how well a model describes the outcome. The higher the value of R^2, the higher the VIF value, and more related are the two predisposing factors to each other. On the other hand, low VIF values are linked to small R^2 values. The minimum value the VIF can assume is 1, which means total absence of collinearity. Generally speaking, James et al. (2021) suggest being careful with parameters whose VIF value exceeds 5. The standard value of VIF proposed in the CONFIG.txt file is 5. Beware, any predisposing factor with a VIF higher than the user-selected threshold will be excluded from the analysis. The following entries are related to:

- n_PB, which is the number of pseudo-absence points for the MaxEnt analysis;
- PA_sets the number of sets of different pseudo-absence points (for GBM and RF) or background points (for MaxEnt) used to elaborate multiple single models;
- k which is the number of folds for the k-Fold Crossvalidation, used on the presence data, allowing the iteration of the modelization process and obtaining a performance score for every single model;
- EM_th is the minimum performance score needed for a model to be used during the ensemble modeling phase and to contribute to the final ensemble model.

The last section of the CONFIG.txt file is related to the Sinkhole Hazard scenario analysis. The two entries “break1” and “break2” represent, respectively, the upper limit of the class with the smaller diameter value, and the second number represents the minimum dimension of the third class. Once the CONFIG.txt file has been successfully modified by the user, the main script can be executed.

5.3.1 *Predisposing factors*

Regarding the predisposing factor, the tool requires them to be provided in .asc format, and they also must have the same extension and resolution. If there are any differences between the .asc raster files, the process will stop. As it is, the tool could also be used to evaluate other geohazard susceptibility, like landslides. There is not a restriction on which type of predisposing factors can be provided. In the specific case of the city of Naples, which has been used to showcase the results later, the predisposing factors used are the following:

- AS_Net_Den, which represents the density of elements related to the main aqueduct and sewer networks;

- AS_Net_Dis, which is the distance to the main aqueduct and sewer networks;

- Cav_Den, the density of underground cavities;

- Cav_Dis, distance to the underground cavity network;

- Geology;

- Hydr_Net_Den, the density of elements that are part of the hydrographic network;

- Hydr_Net_Dis, distance to the hydrographic network;

- Cover_Thick, the thickness of the cover layer;

- Land_Use;

- Road_Den, density of the road network;

- Road_Dis distance to the roads;

- Slope_Angle.

As specified before, other predisposing factors can be freely added, assuming they are useful to the ongoing analysis. As for the first of the different products of the tool, the VIF analysis is shown in the "Other_Results" folder and named as "01_VIF_Analysis.tiff" (Figure 45).

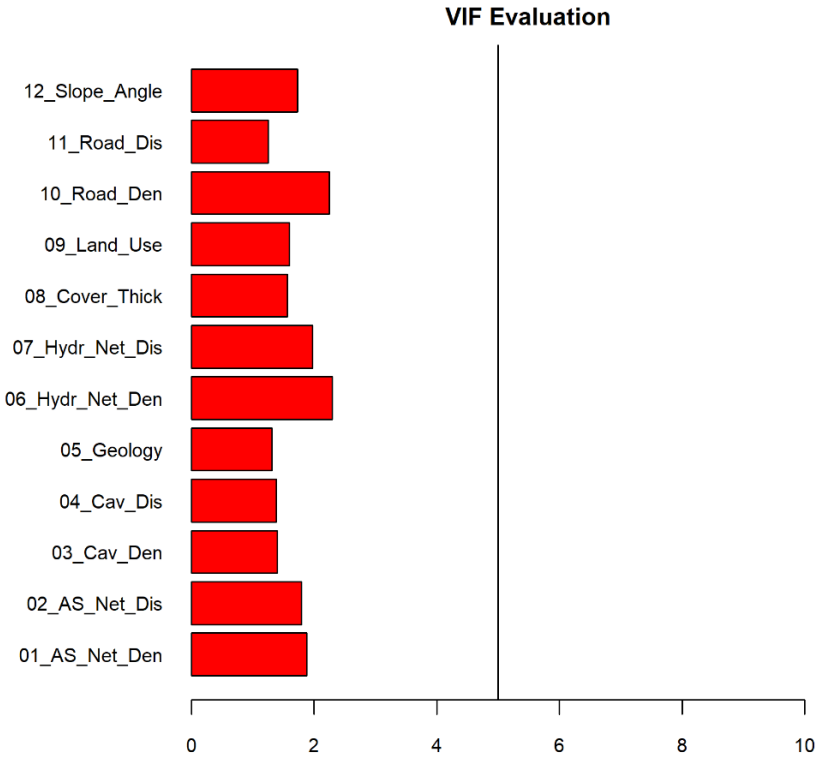

Figure 45. Example of one of the products of the tool, the VIF analysis, in this case, no collinearity problems are found, and all the predisposing factors will be used.

5.3.2 *Ensemble Modeling*

The following steps of the proposed approach are slightly different based on the selected method. In both cases, the presence data provided are divided into two sets: the training data (70%) and the test data (30%). The training data is used to train the singular machine learning models, while the remaining 30% is used at the end of the analysis to test the ensemble model obtained to avoid positive bias in the final performance evaluation. The singular models are evaluated using the k-fold Crossvalidation method.

The training data is divided into k numbers of sets. Of these sets, k-1 are used to train the model, and 1 is used to validate the singular model. By iterating the process and changing the validate set, multiple models can be obtained varying the input data. This validation score of the base models is used to check if the models overcome the user-defined threshold and if it will be used to evaluate the ensemble model (Figure 46).

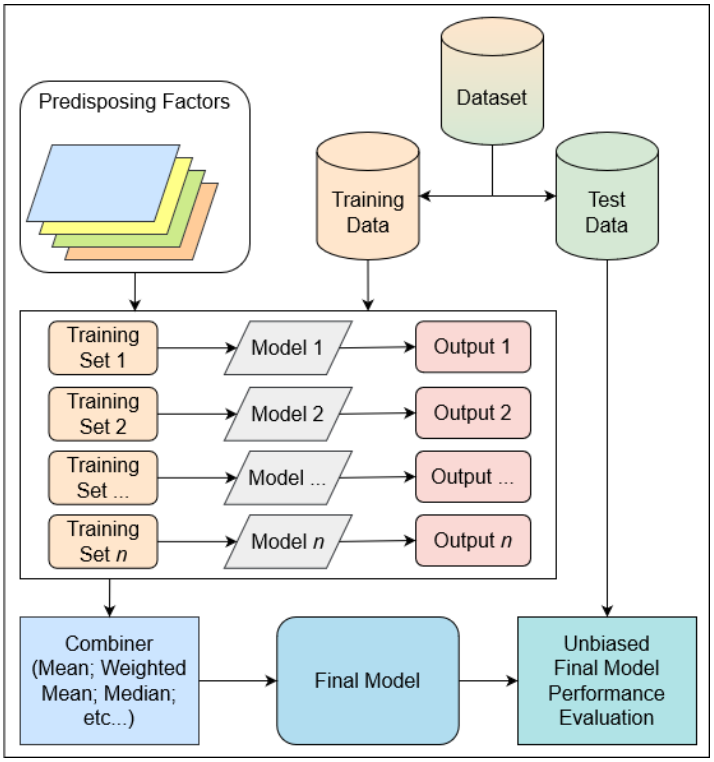

Figure 46. Flowchart of a generic Ensemble Model.

The tool uses three machine learning models to evaluate the singular models: Random Forest (RF), Gradient Boosting Machine (GBM), and Maximum Entropy (MaxEnt). Due to compatibility reasons with different machines, the MaxEnt version used is not the one provided with the "dismo" package, but a different version specifically built for R, and, from hereafter, it will be referred to as MAXNET and not MAXENT.

Random Forest is a machine learning algorithm that produces, for every model, a multitude of decision trees. Every tree is made of nodes, from where different branches develop. For every node, only a subset of predisposing factors is evaluated. At the following node, a new subset of factors is randomly chosen and evaluated. In this way, the algorithm produces trees that can be extremely different from one another, which is intended as if every tree used the same amount and kind of predisposing factors, then one extremely important factor would always be the main discerning one. During the modeling phase, a portion of the data, the out-of-bag (OOB) data, is excluded from the training. This data is then used to evaluate the tree's performance and to determine the importance of the predictors. In the final step, the values of one predictor are permuted each time a tree is processed. By comparing the tree's predictive accuracy before and after the permutation, we can assess the impact of the predictor's randomization.

As for the Gradient Boosting Machine (GBM), it is similar to the Random Forest, as it also creates a multitude of trees, but the iteration of different models is also used to increase the overall performance of the final model. The modeling phase starts with the attribution of an average weight for the predisposing factors. The training data is also used to verify the performance of the initial model. Afterward, a new weight evaluation is performed until it reaches acceptable results, or it reaches the maximum number of iterations allowed. In particular, the new weight evaluation is executed by creating a new decision tree that focuses on minimizing the error evaluated with the previous tree. The main difference with the RF algorithm is related to the usage of the decision trees. In RF, the trees are models in themselves, while the GBM uses every tree as a weak learner to improve the previous one. Both RF and GBM could be considered, on their own, ensemble models (James et al., 2021).

Maximum Entropy (and also MAXNET) was first developed and used as a species distribution tool. It relies on the assumption that the best model that describes the spatial distribution of a species (in this tool, sinkholes) is obtained by maximizing the entropy, which is the degree of resolution of the system. It is also used to measure how important a predisposing factor or other parameter is within a model. During the analysis, the algorithm evaluates the predisposing factors in correspondence with both the presence points (the sinkholes) and the background points, finding the areas that are more likely to contain predisposing factor data compatible with those found in correspondence with the presence data. The model obtained corresponds to the model without initial hypotheses, which can lead to phenomena occurrence with any combination of predictive variables since it has the maximum uncertainty on occurrence probability (Phillips and Dudik, 2008). Regarding predisposing factors importance, the algorithm utilizes the data permutation approach: it replaces the values of a predisposing factor randomly, and if the new values lead to a strong reduction of the model performance, then the analyzed parameter is significant to the model. If the permutation does not influence the final performance, then the analyzed predisposing factor is not important for modeling purposes. Any loss of performance is measured, and the difference between the performance before and after the permutation allows the evaluation of the predisposing factor importance for the model.

After the singular models are produced and validated using the k-fold Crossvalidation approach, the ensemble model production starts. An ensemble model is a combination of multiple models obtained using both different algorithms and different input data. In the case of the presented tool, three different algorithms and a user-defined number of different sets of pseudo-absences are provided. The total number of models produced with this tool is equal to:

$$Total\ number\ of\ models = 3\ (number\ of\ algorithms)\ \times n°\ of\ Pseudo\ Absence\ sets\ \times k\ (k-fold\ crossvalidation)$$

Considering 10 sets of pseudo-absences and a 3-fold Crossvalidation, the total number of models obtained is 90. As the last step for the spatial occurrence assessment, the models that overcome the user-

defined ROC threshold are combined into the final ensemble model using, as the combiner, a weighted mean. The weight of the models is based on their validation score. The final performance evaluation is performed using the ROC/AUC, Sensitivity, Specificity and standardized True Skill Statistic (sTSS) scores (Fauwcett, 2006). In order to evaluate the ROC/AUC and the sTSS performance score, the Sensitivity and Specificity need to be evaluated first using the true positive (areas influenced by sinkholes and detected as a criticality), true negative (areas not affected by sinkholes and not recognized as a criticality), false positive (areas not influenced by sinkholes recognized as a criticality), and false negative (areas impacted by sinkholes but not recognized as a criticality) values. Sensitivity is calculated as:

$$Sensitivity = \frac{true\ positive}{true\ positive + false\ negative}$$

While Specificity is calculated as:

$$Specificity = \frac{true\ negative}{true\ negative + false\ positive}$$

The ROC/AUC score is based on the Receiver Operating Characteristics (ROC) curve and, subsequently, the relative Area Under the Curve (AUC). The ROC curve is built plotting the Sensitivity on the y-axis and the false positive rate (1-Specificity) on the x-axis. By evaluating the area under the ROC curve, the ROC/AUC score is obtained.

The sTSS is the standardized value of the TSS, calculated as:

$$TSS = Sensitivity - \frac{false\ positive}{false\ positive + true\ negative}$$

5.3.3 *Results*

At the end of the first part of the analysis, different products are already available. The first product has already been shown: the VIF analysis (Figure 45). If no predisposing factors show collinearity problems, a single bar plot is produced. On the other hand, if there are collinearity issues, a second bar plot is produced to show the results of the second VIF scores after taking out the predisposing factors that show collinearity. The second product is used to show the Presence and Pseudo Absence points within the analyzed area (Figure 47).

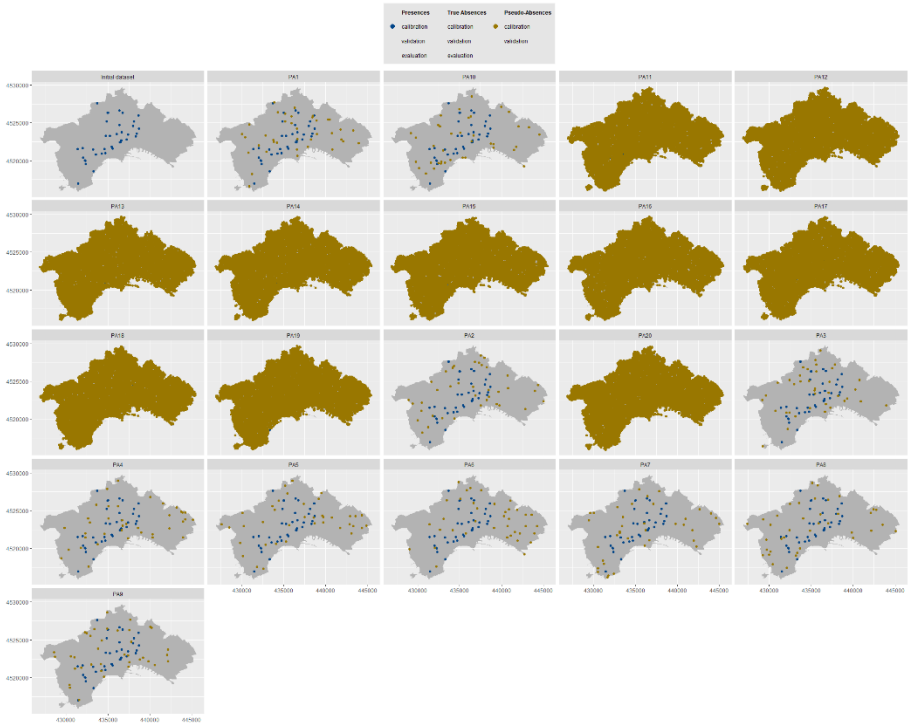

Figure 47. Example of Presence and Pseudo Absence points.

The following products are related to plotting the singular models (Figure 48) and the ensemble model obtained (Figure 49). The first one is named "03_ProjectionData.tiff," while the second one is named "04_SP_FORECAST.tiff." If the method selected is the Sinkhole Hazard scenario evaluation, all these files have a prefix "SET1_," "SET2_," or "SET3_."

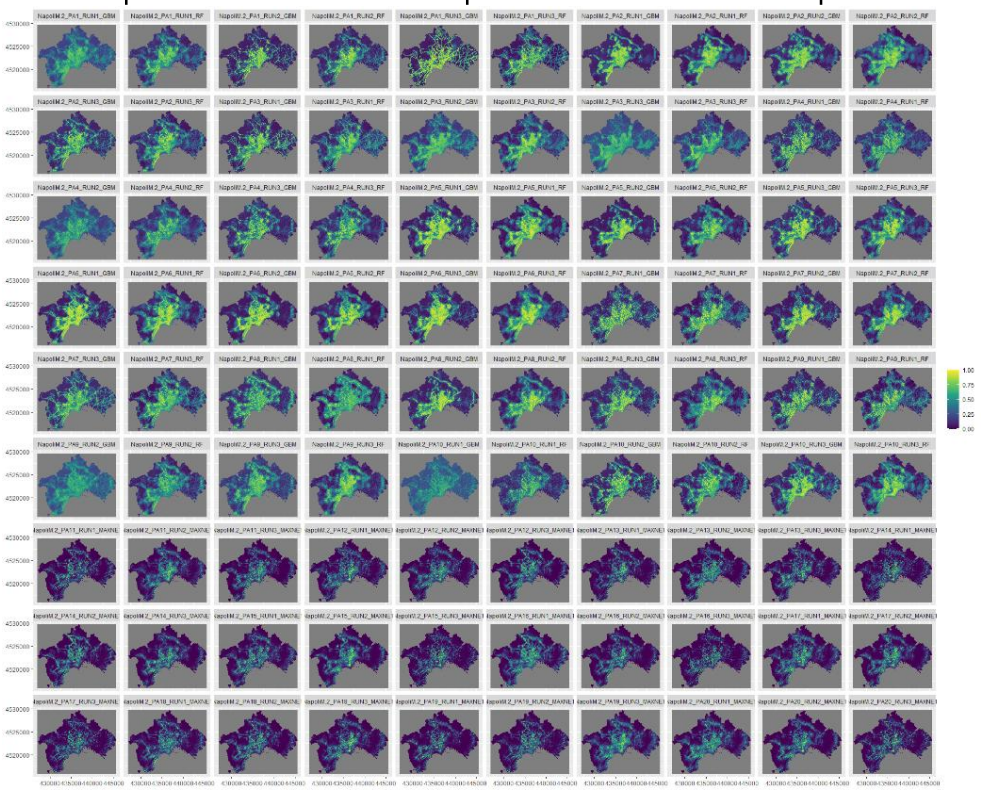

Figure 48. Example of the 03_ProjectionData.tiff product.

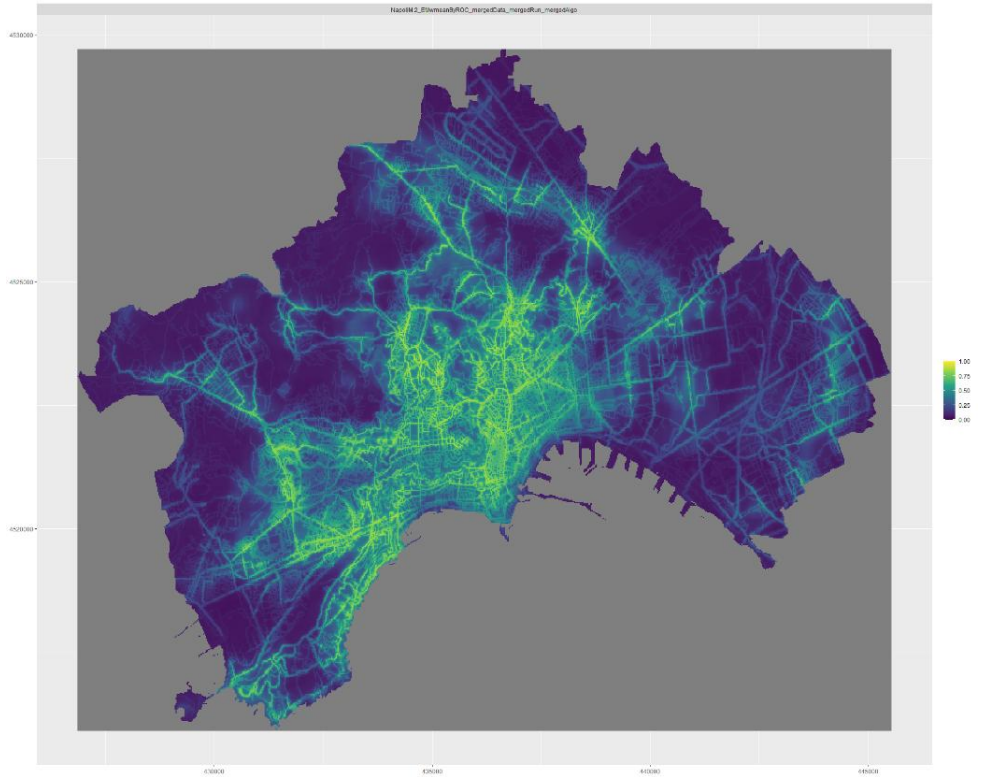

Figure 49. Example of the 04_SP_FORECAST.tiff file.

Additional products that the tool provides are the response curves (Figure 50), which show the relationship between sinkhole and the specific predisposing factor and are named

"05_ResponseCurves.tiff," and the predisposing factors importance boxplot based on the algorithm (Figure 51) ("06_VarImp_Alg.tiff").

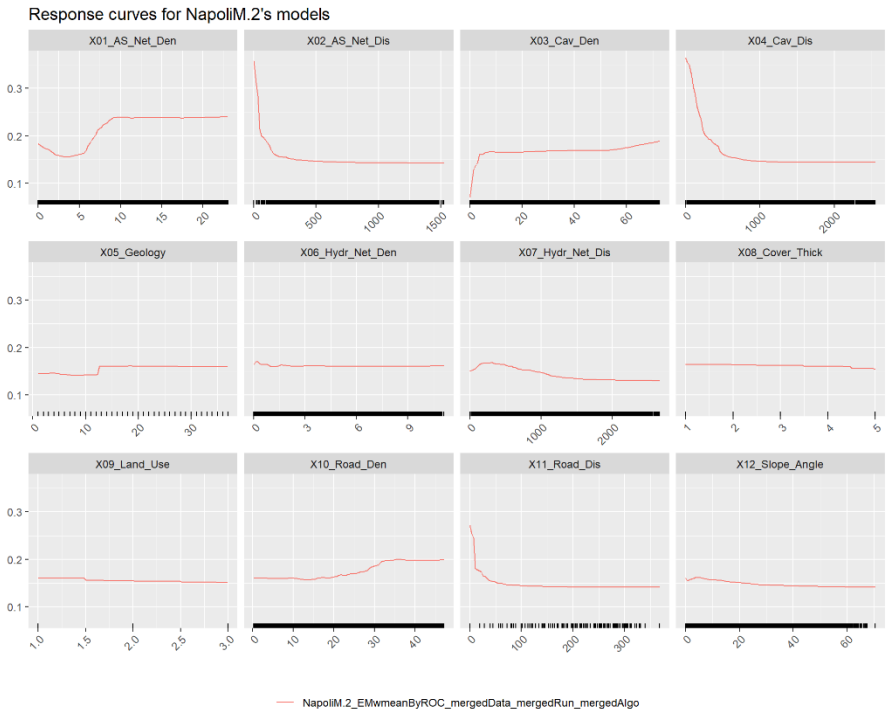

Figure 50. Example of response curves obtained from the proposed tool.

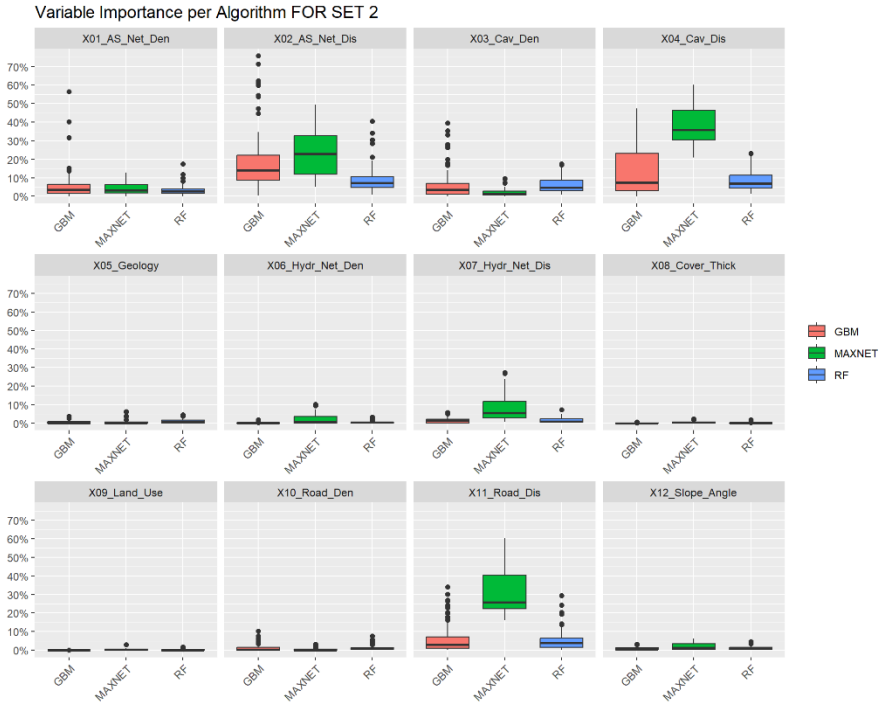

Figure 51. Example of predisposing factor importance boxplot.

The remaining results are related to the final ensemble model obtained. In particular, the models' performance score boxplot gathered based on the algorithm (Figure 52) ("07_Models_Alg.tiff"), a different plot of the final ensemble model (Figure 53) ("08_Susceptibility.tiff"), the ROC/AUC performance score of the ensemble model (Figure 54) ("09_ROCAUC_Score.tiff"), a plot containing the

Sensitivity, Specificity and sTSS (Figure 55).

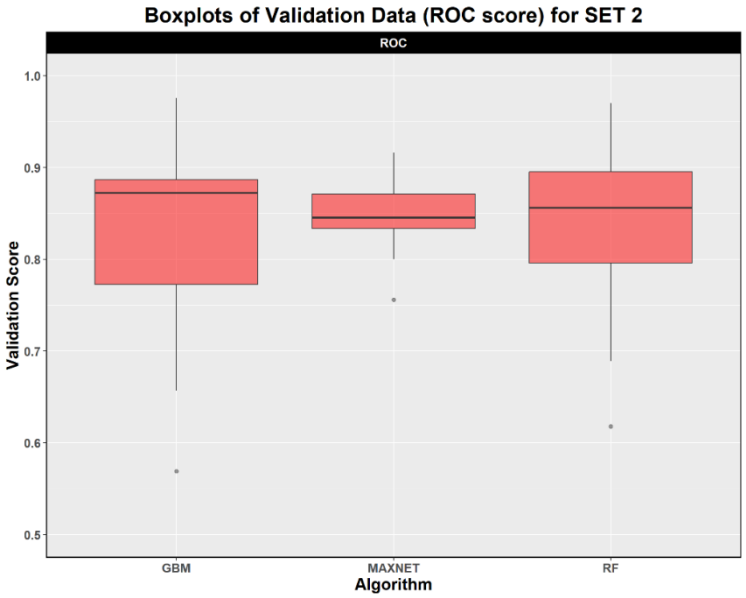

Figure 52. Example of models' performance score boxplot.

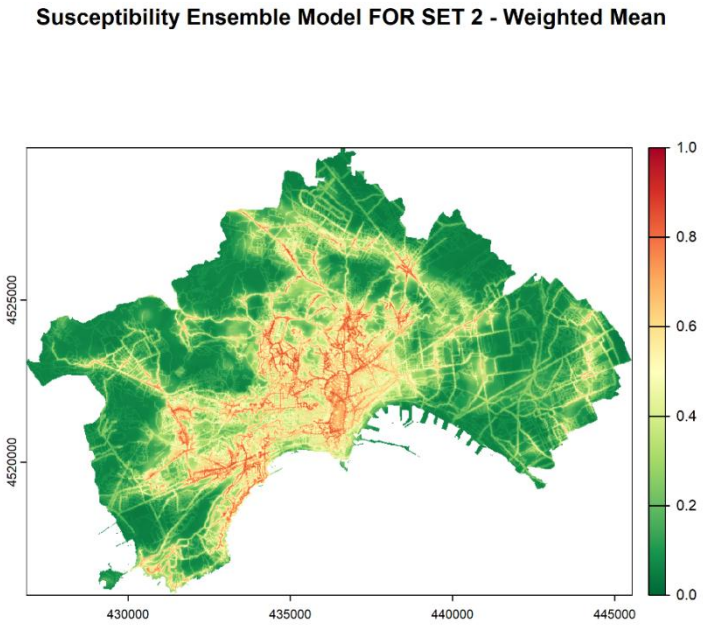

Figure 53. Ensemble model – anthropogenic sinkhole evaluation.

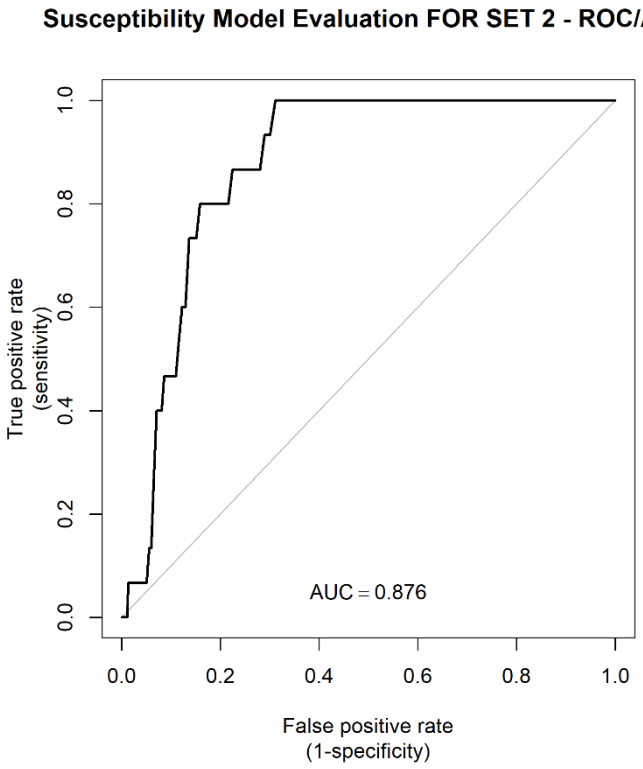

Figure 54. ROC/AUC performance score of the ensemble model.

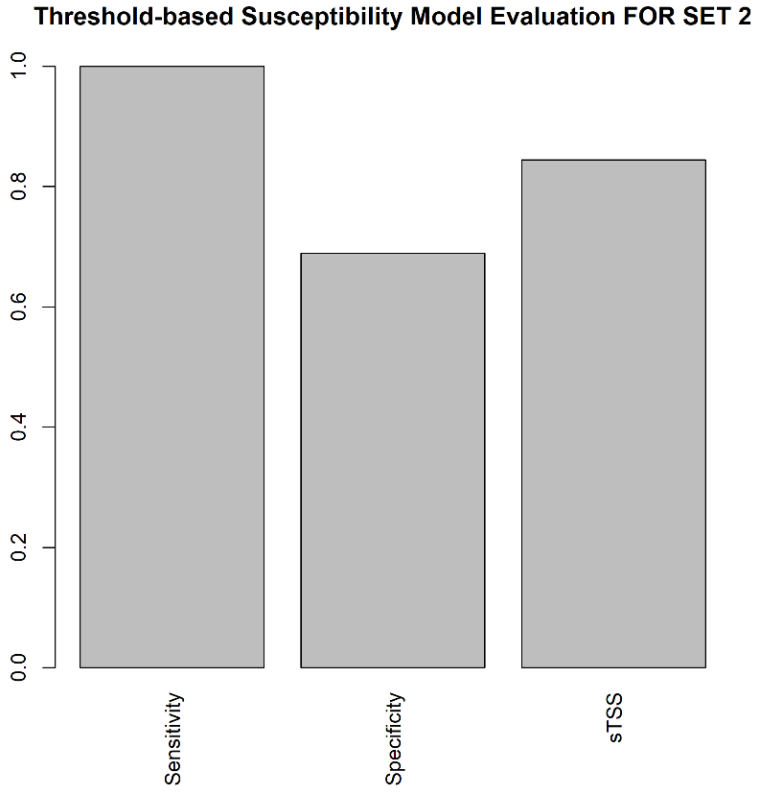

Figure 55. Example of the threshold-based evaluation scores.

Finally, the last plot of this section of the tool provided is the class extension bar plot (in percentage) (Figure 56). The sinkhole susceptibility map is provided as a .tiff file within the Other_Results folder,

named "EM_WM_Susceptibililty.tiff." This raster is divided into five classes using the Natural Breaks method (Jenks, 1967) ("EM_WM_SusceptibililtyReclass.tiff"). The data for the class extension bar plot is obtained from the reclassified spatial occurrence raster file, divided from Very Low to Very High susceptibility class.

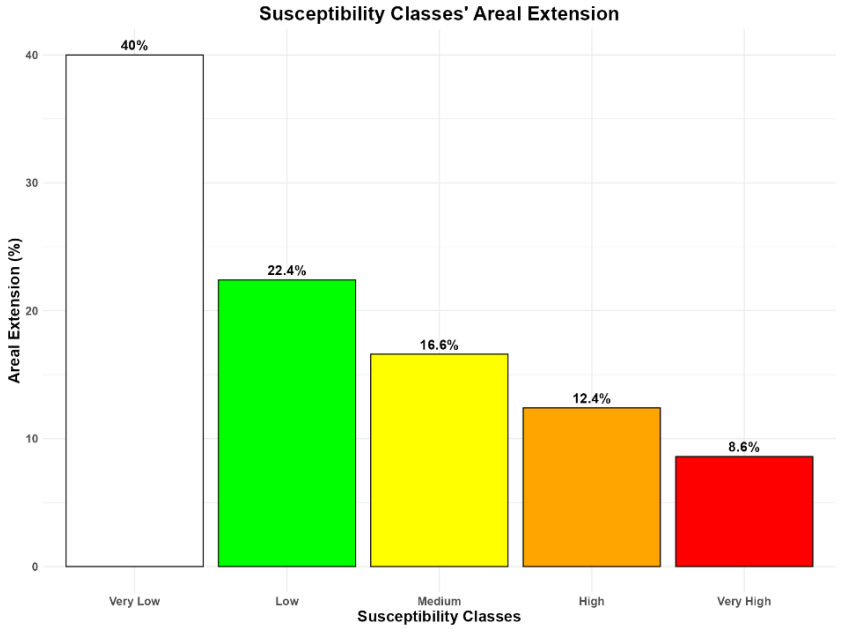

Figure 56. Example of the classes' areal extension bar plot.

Lastly, five .xlsx files are also provided as products:

- Models_VarImp.xlsx – containing all the predisposing factor importance evaluated for all the models;
- ModelsEvaluation.xlsx – contains the validation scores of all the models obtained;
- Performance_Evaluations.xlsx – with the Sensitivity, Specificity, ROC/AUC, and sTSS scores of the final ensemble model;
- Summary_Mean_ModelsPerformance.xlsx – containing the mean ROC and sTSS scores obtained with the different algorithms;
- Summary_Mean_Variable_Importance.xlsx – with the mean variable importance of all the predisposing factors considering all the runs obtained with all the algorithms.

As already specified, when the sinkhole hazard scenario evaluation analysis is selected, three copies of all the products described are provided, differentiated by the numbered set:

- Set 1 for the smaller sinkholes;
- Set 2 for the medium-sized sinkholes;

- Set 3 for the bigger sized sinkholes.

5.4 Anthropogenic Sinkhole Temporal Occurrence Analysis

This section of the tool is executed only if the user has selected the Sinkhole Hazard scenarios evaluation method during the CONFIG.txt file compiling. This analysis uses the second .csv inventory file provided by the user.

As stated before, the distribution analysis used to evaluate the temporal occurrence is the Poisson distribution. It is a probability distribution that evaluates the probability of occurrence of a new and independent event within a time interval. The Poisson distribution assumes that the events are independent in relation to each other and that they occur at a constant average rate. In the showcased example, the sinkholes that occurred during the last 25 years were used as they were the ones with the most constant average rate. The probability P of a new sinkhole initiation within a t time interval can be described by the following formula:

$$P = 1 - exp\left(-\frac{t}{\mu}\right)$$

Where μ represents the mean time between sinkhole events obtained from the inventory in the last 25 years. The product of this analysis is the diagram shown in Figure 57. The red numbers represent the user-defined t that will be used in the following scenario evaluation process.

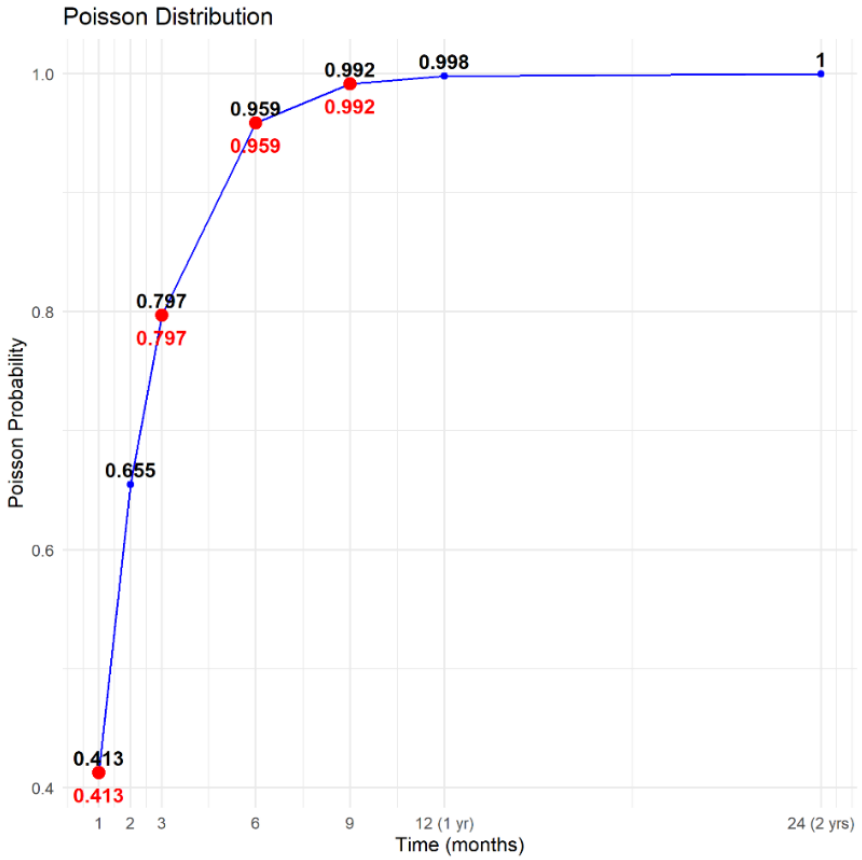

Figure 57. Poisson distribution, the data used for this example are part of the Sinkhole Inventory of the city of Naples.

5.5 Anthropogenic Sinkhole Hazard: scenarios evaluation

As the last step for the Anthropogenic Sinkhole Hazard scenarios evaluation process, the three anthropogenic sinkhole susceptibility map (one for every class of sinkhole diameter) is combined with the temporal probability occurrence obtained using the Poisson distribution (Figure 57) to obtain twelve different scenarios (Figure 58), four for every sinkhole diameter class. The products provided by the tool, in this final step, are twelve .tiff raster files with their values varying from 0 (lowest sinkhole hazard) to 1 (maximum sinkhole hazard). In the showcased example (Figure 59), the four products obtained for the second set of the sinkhole inventory (diameter > 2 m and ≤ 5 m) have been loaded into a GIS environment and assigned the same colour scale to highlight the difference over the four user-defined time intervals.

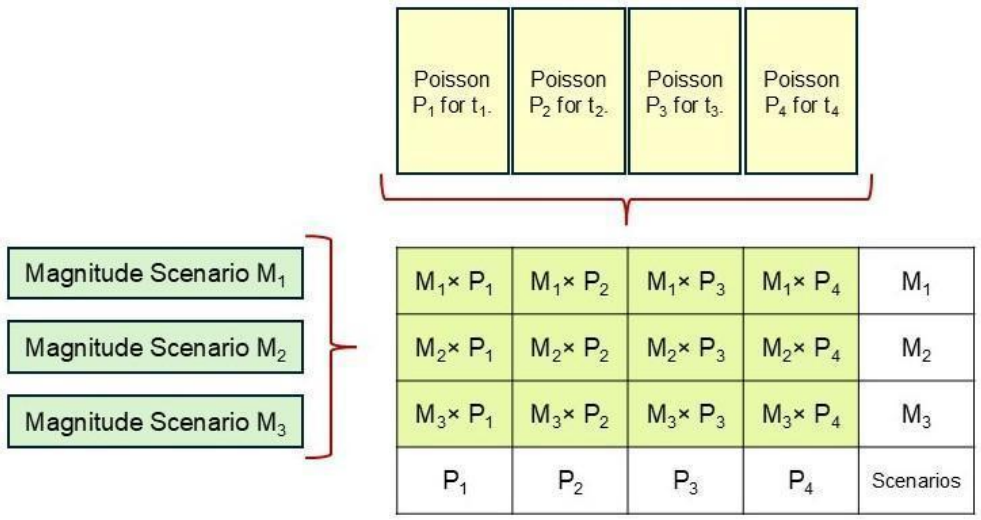

Figure 58. Sinkhole Hazard scenarios evaluation matrix.

.

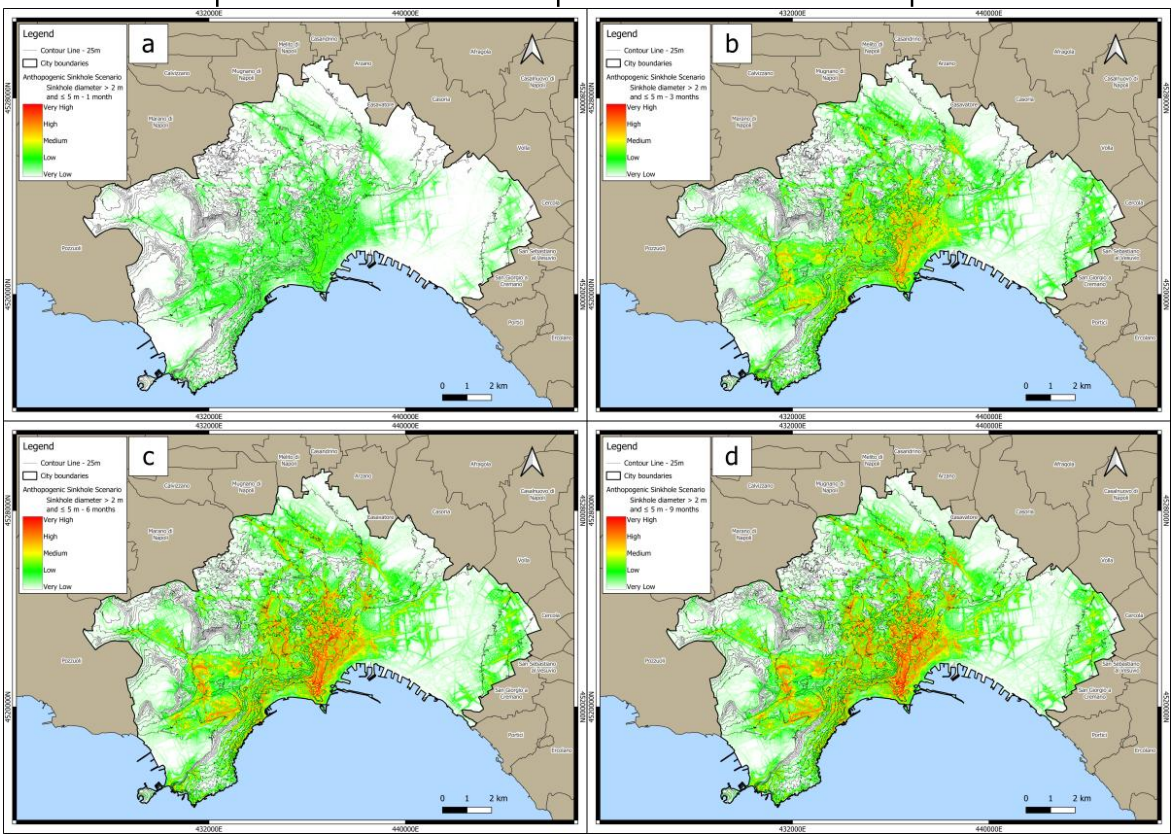

Figure 59. Sinkhole Hazard scenario evolution for sinkholes with a diameter > 2 m and ≤ 5 m within a) 1 month; b) 3 months; c) 6 months; d) 9 months.

5.6 References

Baddeley, A., Rubak, E., and Turner, R. (2015). Spatial Point Patterns: Methodology and Applications with R. Chapman and Hall/CRC Press, London. ISBN 9781482210200, <https://www.routledge.com/Spatial-Point-Patterns-Methodology-and-Applications-with-R/Baddeley-Rubak-Turner/p/book/9781482210200/>.

Barbosa, A.M., Real, R., Munoz, A.R. and Brown, J.A. (2013). New measures for assessing model equilibrium and prediction mismatch in species distribution models. Diversity and Distributions, 19(10), 1333-1338. DOI: 10.1111/ddi.12100. URL: https://onlinelibrary.wiley.com/doi/full/10.1111/ddi.12100.

Bates, D., Eddelbuettel, D. (2013). "Fast and Elegant Numerical Linear Algebra Using the RcppEigen Package." Journal of Statistical Software, *52*(5), 1-24. doi:10.18637/jss.v052.i05 <https://doi.org/10.18637/jss.v052.i05>.

Bivand, R. (2025). classInt: Choose Univariate Class Intervals. R package version 0.4-11, <https://CRAN.R-project.org/package=classInt>.

Bonaccorso, R., Grasso, S., Lo Giudice, E., and Maugeri, M. (2005). Cavities and hypogeal structures of the historical part of the City of Catania. Advances in Earthquake Engineering, 14(2005), 197-223.

Breiman, L. (2001). Random Forests. Kluwer Academic Publishers. Machine Learning, 45(1), 5–

32. https://doi.org/10.1023/A:1010933404324.

Chen, T., He, T., Benesty, M., Khotilovich, V., Tang, Y., Cho, H., Chen, K., Mitchell, R., Cano, I., Zhou, T., Li, M., Xie, J., Lin, M., Geng, Y., Li, Y., and Yuan, J. (2024). xgboost: Extreme Gradient Boosting. R package version 1.7.8.1, <https://CRAN.R-project.org/package=xgboost>.

Cheng, J., Schloerke, B., Karambelkar, B., and Xie, Y. (2024). leaflet: Create Interactive Web Maps with the JavaScript 'Leaflet' Library. R package version 2.2.2, <https://CRAN.R-project.org/package=leaflet>.

Corporation, M., and Weston, S. (2022). doParallel: Foreach Parallel Adaptor for the 'parallel' Package. R package version 1.0.17, <https://CRAN.R-project.org/package=doParallel>.

Dastpak, P., Sousa, R. L., and Dias, D. (2023). Soil erosion due to defective pipes: a hidden hazard beneath our feet. Sustainability, 15(11), 8931.

Fasani, G. B., Bozzano, F., Cardarelli, E., and Cercato, M. (2013). Underground cavity investigation within the city of Rome (Italy): A multi-disciplinary approach combining geological and geophysical data. Engineering Geology, 152(1), 109-121.

Fawcett, T. (2006). An introduction to ROC analysis. Pattern recognition letters, 27(8), 861-874.

Friedman, J. H. (2001). Greedy function approximation: A gradient boosting machine. Institute of Mathematical Statistics. The Annals of Statistics., 29(5), 1189–1232. https://doi.org/10.1214/aos/1013203451

Guarino, P. M., and Nisio, S. (2012). Anthropogenic sinkholes in the territory of the city of Naples (Southern Italy). Physics and Chemistry of the Earth, Parts A/B/C, 49, 92-102.

Gutiérrez, F. (2016). Sinkhole hazards. In Oxford research encyclopedia of natural hazard science.

Guzzetti, F., Reichenbach, P., Cardinali, M., Galli, M., and Ardizzone, F. (2005). Probabilistic landslide hazard assessment at the basin scale. Geomorphology, 72(1-4), 272-299.

Haight, F. A. (1967). Handbook of the Poisson Distribution. Wiley. ISBN: 9780471339328.

Hastie, T. (2024). gam: Generalized Additive Models. R package version 1.22-5, <https://CRAN.R-project.org/package=gam>.

Hastie, T., and Tibshirani, R. (2024). mda: Mixture and Flexible Discriminant Analysis. R package version 0.5-5, <https://CRAN.R-project.org/package=mda>.

Hernangómez, D. (2023). “Using the tidyverse with terra objects: the tidyterra package.” Journal of Open Source Software, *8*(91), 5751. ISSN 2475-9066, doi:10.21105/joss.05751 <https://doi.org/10.21105/joss.05751>.

Hijmans, R., Phillips, S., Leathwick, J., and Elith, J. (2024). dismo: Species Distribution Modeling.

R package version 1.3-16, <https://CRAN.R-project.org/package=dismo>.

Hijmans, R. (2025a). raster: Geographic Data Analysis and Modeling. R package version 3.6-31, <https://CRAN.R-project.org/package=raster>.

Hijmans, R. (2025b). terra: Spatial Data Analysis. R package version 1.8-21, <https://CRAN.R-project.org/package=terra>.

James, G., Witten, D., Hastie, T., and Tibshirani, R. (2021). An Introduction to Statistical Learning: With Applications in R (Second Edition). Springer US. https://doi.org/10.1007/978-1-0716-1418-1

Jenks, G. F. (1967). The data model concept in statistical mapping. International yearbook of cartography, 7, 186-190.

Kuhn, M. (2008). Building Predictive Models in R Using the caret Package. Journal of Statistical Software, 28(5), 1–26. https://doi.org/10.18637/jss.v028.i05.

Liaw, A., and Wiener, M. (2002). "Classification and Regression by randomForest." R News, *2*(3), 18-22. <https://CRAN.R-project.org/doc/Rnews/>.

Milborrow, S., Hastie, T., and Tibshirani, R. (2024). earth: Multivariate Adaptive Regression Splines. R package version 5.3.4, <https://CRAN.R-project.org/package=earth>.

Naimi, B., Hamm, Na., Groen, T.A., Skidmore, A.K., and Toxopeus, A.G. (2014). "Where is positional uncertainty a problem for species distribution modelling." _Ecography_, *37*, 191-203. doi:10.1111/j.1600-0587.2013.00205.x <https://doi.org/10.1111/j.1600-0587.2013.00205.x>.

Ooms, J. (2024). writexl: Export Data Frames to Excel 'xlsx' Format. R package version 1.5.1, <https://CRAN.R-project.org/package=writexl>.

Parise, M. (2015). A procedure for evaluating the susceptibility to natural and anthropogenic sinkholes. Georisk: Assessment and Management of Risk for Engineered Systems and Geohazards, 9(4), 272-285.

Pebesma, E., 2018. Simple Features for R: Standardized Support for Spatial Vector Data. The R Journal 10 (1), 439-446, https://doi.org/10.32614/RJ-2018-009.

Pebesma, E., and Bivand, R. (2023). Spatial Data Science: With Applications in R. Chapman and Hall/CRC. https://doi.org/10.1201/9780429459016.

Phillips, S. J., and Dudík, M. (2008). Modeling of species distributions with Maxent: new extensions and a comprehensive evaluation. Ecography, 31(2), 161-175.

Phillips, S. (2021). maxnet: Fitting 'Maxent' Species Distribution Models with 'glmnet'. R package version 0.1.4, <https://CRAN.R-project.org/package=maxnet>.

Poisson, S. D. (1837). Recherches sur la probabilité des jugements en matière criminelle et en matière civile: précédées des règles générales du calcul des probabilités. Bachelier. (in French).

Posit team (2025). RStudio: Integrated Development Environment for R. Posit Software, PBC, Boston, MA. URL http://www.posit.co/.

Puntillo, E. (2001). Le catastrofi innaturali. Tullio Pironti. (in Italian)

R Core Team (2024). R: A Language and Environment for Statistical Computing. R Foundation for Statistical Computing, Vienna, Austria. <https://www.R-project.org/>.

Singh, K. B., and Dhar, B. B. (1997). Sinkhole subsidence due to mining. Geotechnical & Geological Engineering, 15, 327-341.

Tay, J.K., Narasimhan, B., and Hastie, T. (2023). "Elastic Net Regularization Paths for All Generalized Linear Models.". Journal of Statistical Software, *106*(1), 1-31. doi:10.18637/jss.v106.i01 <https://doi.org/10.18637/jss.v106.i01>.

Thuiller, W, Georges, D., Gueguen, M, Engler, R., Breiner, F., Lafourcade, B., and Patin, R. (2023). biomod2: Ensemble Platform for Species Distribution Modeling. R package version 4.2-4, <https://CRAN.R-project.org/package=biomod2>.

Todaro, P. (2020). La pratica dei sistemi d'acqua sotterranei "ingruttati" nella Piana di Palermo e analisi della terminologia di riferimento. OPERA IPOGEA, 1-2/2020, 35–44. (in Italian)

Varriale, R., Parise, M., Genovese, L., Leo, M., and Valese, S. (2022). Underground Built Heritage in Naples: From Knowledge to Monitoring and Enhancement. In Handbook of Cultural Heritage Analysis (pp. 2001-2035). Cham: Springer International Publishing.

Waltham, A. C., and Fookes, P. G. (2003). Engineering classification of karst ground conditions. Quarterly Journal of Engineering Geology and Hydrogeology, 36(2), 101-118.

Waltham, T., Bell, F. G., Culshaw, M. G., Knez, M., and Slabe, T. (2005). Sinkholes and subsidence: karst and cavernous rocks in engineering and construction (Vol. 382). Berlin: Springer.

Wickham, H. (2016). ggplot2: Elegant Graphics for Data Analysis. Springer-Verlag New York. <https://ggplot2.tidyverse.org>.

Wickham, H., François, R., Henry, L., Müller, K., and Vaughan, D. (2023). dplyr: A Grammar of Data Manipulation. R package version 1.1.4, <https://CRAN.R-project.org/package=dplyr>.

Wilke, C., and Wiernik, B. (2022). ggtext: Improved Text Rendering Support for 'ggplot2'. R package version 0.1.2, <https://CRAN.R-project.org/package=ggtext>.

6 The RETURNLAND Virtual Test Bed

The RETURN Virtual Test Bed (VTB), defined as RETURNLAND, was designed to recreate a unified spatial context reflecting the environmental conditions throughout the country, serving as a general framework within which the ground instabilities addressed by VS2 are studied and modelled. One of the key objectives of the project is undoubtedly the development of a Virtual Test Bed (VTB), conceived as a realistic territory (i.e., encompassing geo- and hydro-morphological features typical of widely occurring contexts across the landscape), though not necessarily corresponding to an overall real location. The VTB serves as a testing environment for evaluating the performance and versatility of toolchains validated through the demonstrator cases described in the reports of the Tasks belonging to WP4.

From a broader perspective, which considers the HUB as a whole and not only Spoke VS2, the VTB acts as an "experimental digital platform" designed to test the functionality of the complete workflow. This workflow begins with the generation of instability scenarios over relatively large areas and the definition of parameters useful for estimating impact energy, and proceeds toward the evaluation of expected losses (damage) to specific structures, infrastructures, or environmental assets. In other words, the VTB is intended to demonstrate the applicability of the entire chain of processes triggered by endogenous and/or exogenous forcing within a necessarily broad territorial context — RETURNLAND, a realistic virtual site of large extent that includes all the environments which have been the subject of specific toolchain development — and to assess the resulting expected damage within anthropic contexts, which are also virtual yet realistic, located in the RETURNVILLEs established in specific areas of RETURNLAND. In line with the aforementioned goals, the chosen approach consists in constructing both RETURNLAND and RETURNVILLE through a "mosaicking" of real territorial segments, appropriately "stitched together" to form a coherent territorial whole. This choice aims to:

i) ensure the adherence of each VTB segment to real-world characteristics, and

ii) link each segment to its specific datasets, thus enabling truly realistic analyses.

Lastly — though no less importantly — as a matter of good scientific practice, the selected real territorial segments are not those where the toolchains have already been validated, thereby avoiding a tautological feedback loop in the assessment of toolchain operability. It is reported in Fig. 60. It leverages a combination of high-resolution digital elevation models (DEMs), both terrestrial (Figure 61) and marine, derived from Learning Examples (LEs) that provide comprehensive geological data.

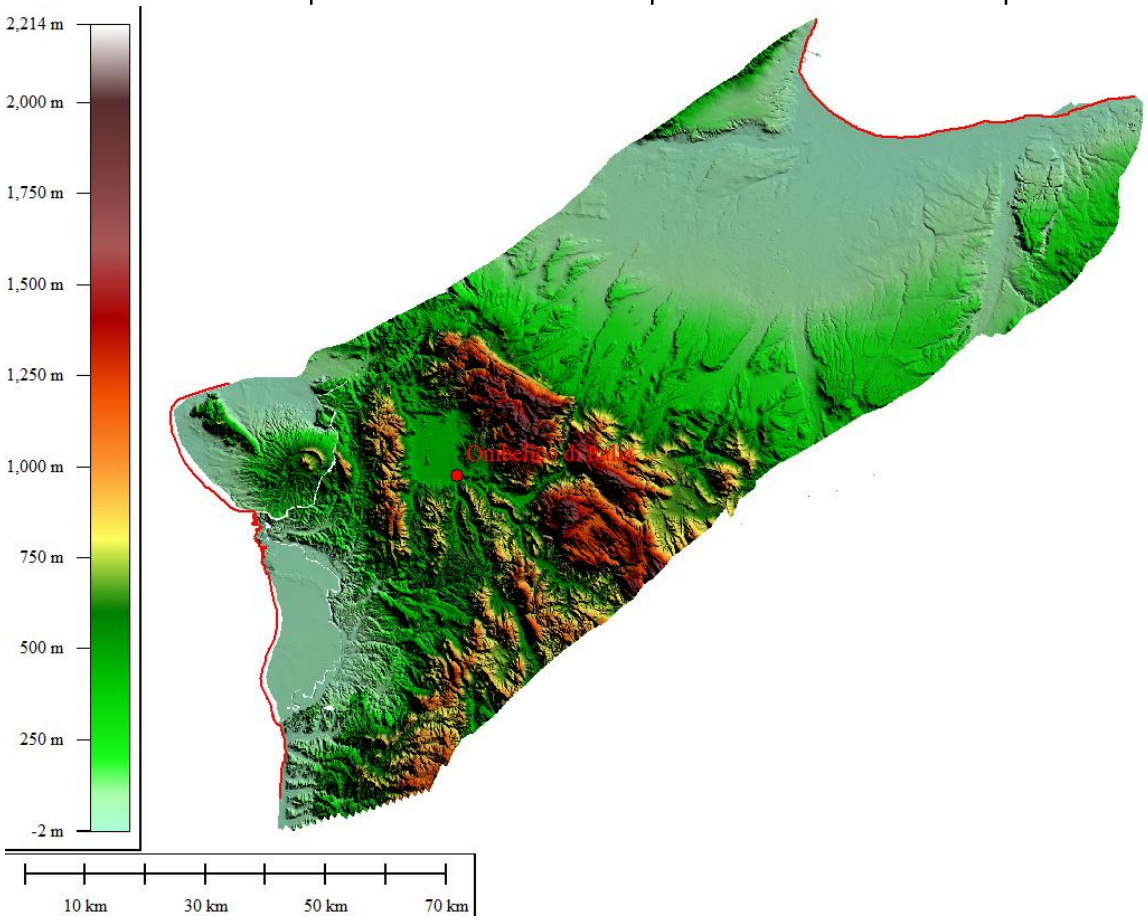

Figure 60. RETURNLAND terrestrial part, before the final merge step.

In the context of plain areas, the VTB includes representative sites in the Emilia-Romagna region (Figure 61a), the Apulia region (Figure 61b), and the Basilicata region (Figure 61c), selected to highlight key ground instabilities processes. Specifically, the site in Emilia-Romagna focuses on liquefaction phenomena and subsidence, while the Tavoliere delle Puglie, in Apulia region, addresses issues related to subsidence and anthropogenic sinkholes. The Metaponto area, in Basilicata region, is of particular significance, as it hosts an important archaeological park, highlighting the need to assess hazard impacts not only on the environment but also on cultural heritage (VS4). The generation of this synthetic DEM involved several important steps. First, the reference systems of the individual DEMs were transformed to a common coordinate system (EPSG:32633 – WGS 84 / UTM zone 33N). Then, the DEMs were aligned using rigid transformations (translations and rotations), considering their elevation values and minimizing discrepancies between them. Once aligned, the DEMs were resampled to the same spatial resolution and merged to form the final VTB. The entire workflow was carried out using various GIS software tools, including Global Mapper, ArcGIS, and QGIS. This VTB is essential for simulating, testing, and analysing real-world processes related to terrestrial and submarine processes. The insights derived from these VTB scenarios are expected to significantly enhance our understanding of both terrestrial and submarine processes.

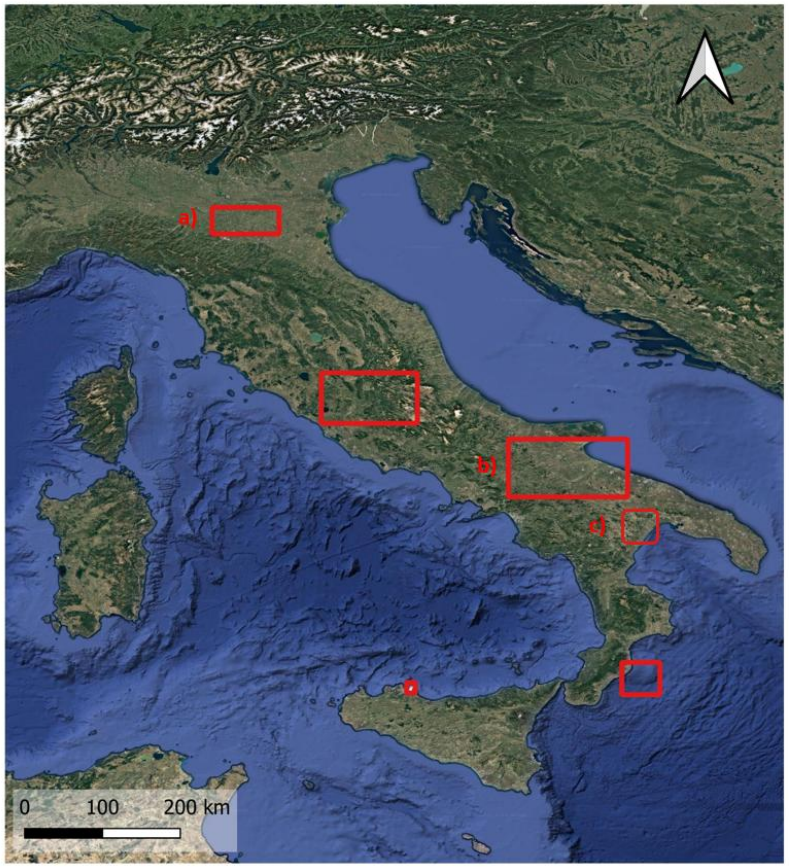

Figure 61. Image representing the study areas from which DTMs were extracted. In particular, the boxes indicated by letters a), b) and c) indicate plain areas.

7 Conclusions

This deliverable (DV 2.4.6) has presented the implementation and validation of thematic mapping methodologies for ground instabilities in large plains, focusing on soil liquefaction, regional subsidence, and anthropogenic sinkholes. These methodologies, designed within the RETURN project framework, aim to support the development of robust, transferable tools for multi-hazard risk assessment under changing climatic and environmental conditions. The deliverable outlines a multi-level, tool-chain-based approach that integrates spatial and temporal data to assess hazard severity and produce risk zoning for the selected geohazards. Each process was treated through a structured methodology, from the identification of relevant input parameters (related to predisposing, preparatory, and triggering factors) to the generation of output indicators and hazard scenarios. In the following Table, a structured overview of the methodologies applied to assess three ground instability processes—soil liquefaction, regional subsidence, and anthropogenic sinkholes is reported. For each process, the corresponding assessment method, required input datasets, and resulting output parameters are summarized.

Process	**Method**	**Input Data**	**Output**
Soil Liquefaction	Multi-level tool chain approach (Level 0–2): - Qualitative screening (Level 0 - 1) - Semi-empirical stress-based analysis (Level 2)	- Geological and geomorphological maps - Groundwater table depth - Peak Ground Acceleration (PGA) - CPT geotechnical investigations - Soil classification - Historical liquefaction records	- Susceptibility maps (Level 0 & 1) - Liquefaction Potential Index (LPI) - Factor of Safety (FS) profiles - Settlement maps
Regional Subsidence	Satellite-based monitoring and temporal modeling: - PSI (Persistent Scatterer Interferometry) - Trend and change detection algorithms	- InSAR satellite data (e.g., Sentinel-1) - Geological setting - Land use and infrastructure layers - Groundwater extraction data - Geochronological calibration points	- Vertical displacement trends - Classification of deformation (e.g., abrupt, seasonal) - Modeled velocity fields - Spatial maps of subsidence-prone zones
Anthropogenic Sinkhole	Ensemble susceptibility modeling and probabilistic forecasting: - Machine learning (RF, GBM, MaxEnt) - Poisson temporal analysis	- Sinkhole inventory (location, time, size) - Geological and urban infrastructure data - DEM, soil type, land use layers - User-defined scenario classes (diameter, time)	- Susceptibility maps (ensemble outputs) - Variable importance plots - Magnitude-based hazard scenarios (3 classes) - Temporal probabilities (4 return periods) - Combined 12-scenario hazard matrix